Document Number**:** H2020-ICT-52/RISE-6G/D3.1

Project Name:

Reconfigurable **I**ntelligent **S**ustainable **E**nvironments for **6G** Wireless Networks

RISE-6G

Deliverable D3.1

Preliminary RIS model and measurement campaigns

Date of delivery:	03/05/2022	Version:	Final
Start date of Project:	01/01/2021	Duration:	36 months

Deliverable D3.1
Preliminary RIS model and measurement campaigns

Project Number:	101017011
Project Name:	**R**econfigurable **I**ntelligent **S**ustainable **E**nvironments for **6G** Wireless Networks

Document Number:	H2020-ICT-52/RISE-6G/D3.1
Document Title:	Preliminary RIS model and measurement campaigns
Editor(s):	R. D'Errico (CEA)
Authors:	CEA: R. D'Errico, A. Clemente, G. Makhoul, A. Mudonhi, S.Garbieh, M. Bouslama
	UNOT : G. Gardoni, S. Terranova, G.Tanner
	GNW ; Jean Baptiste Gros,
	CNRS: M di Renzo
	CNIT : L. Bastianelli, F. Moglie, V. Mariani
	TIM: D. Micheli
	AAU : O. Franek
	NKUA : G. Alexandropoulos, I. Vinieratou
	ORA : P. Ratajczak
Dissemination Level:	PU
Contractual Date of Delivery:	30/10/2021
Security:	Public
Status:	Final
Version:	2.0
File Name:	RISE-6G_WP3_D3.1_Final.docx

Contents

	Document:	H2020-ICT-52/RISE-6G/D3.1		
	Date:	03/05/2022	Security:	Public
	Status:	Final	Version:	2.0

List of Figures

	Document:	H2020-ICT-52/RISE-6G/D3.1		
	Date:	03/05/2022	Security:	Public
	Status:	Final	Version:	2.0

List of Tables

List of Acronyms

5G-NR	5th Generation - New Radio
BS	Base Station
CAPEX	CAPital EXpenditure
DL	Downlink
DL-DoD	Downlink Direction of Departure
DL-TDoA	Downlink Time Difference of Arrival
DoA	Direction of Arrival
DoD	Direction of Departure
EM	Electromagnetic
GDoP	Geometric Dilution of Precision
KPI	Key-Performance Indicator
LB-AoI	Localization Boosted - Area of Influence
LE-AoI	Localization Enabled - Area of Influence
LoS	Line-of-Sight
MIMO	Multiple Inputs Multiple Outputs
NVAA	Non-Value-Added Activities
OPEX	OPerating EXpenditure
RF	Radio Frequency
R-RIS	Reflective RIS
RT-RIS	Reflective-transmission RIS
RIS	Reconfigurable Intelligent Surface
RSSI	Received Signal Strength Indicator
RTT	Round Trip Time
RT-ToF	Round Trip – Time of Flight
Rx	Receiver
SISO	Single Input Single Output
SLAM	Simultaneous Localization and Mapping
TDoA	Time Difference of Arrival
ToA	Time of Arrival
Tx	Transmitter
UAV	Unmanned Aerial Vehicle
UE	User
UTDoA	Uplink Time Difference of Arrival

UL	Uplink
UL-DoA	Uplink Direction of Arrival
UL-TDoA	Uplink Time Difference of Arrival

1   Introduction

The general objective of RISE-6G WP3 is to model, design, and characterize the RIS components as a part of the overall system for enhanced connectivity, localisation and sensing, as well as sustainability. The RIS prototypes developed in this WP will be also integrated in the final project demonstrations and PoCs.

Here we tackle the main issues related to the electromagnetic modelling of the unit cell and the overall RIS, its impact on the radio "reconfigurable" channels and the main technology challenges related to the design and prototyping in a large frequency range from sub 6 GHz up to D-band.

The general objective of this deliverable is to:

- **Provide an electromagnetic RIS model and a system level abstraction** (Section 2);

- **Characterize and model the RIS-empowered reconfigurable radio channel** (Section 3).

- **Design, prototype and characterize the RISs and control logic for the PoC** (Section 4).

1.1   Definitions

Reconfigurable intelligent surfaces (RISs) are surfaces composed of a discrete set of antenna elements following the generalised Snell's law, and can be seen as **reflective or transmissive electromagnetic surfaces** as a function of the selected operation mode. Specifically, **a reflective surface (R-RIS)** operates as an electromagnetic mirror, where an incident electromagnetic wave is reflected towards the desired direction, typically anomalous in the sense that this direction is non-specular, with specific radiation and polarisation characteristics. On the other hand, a **transmissive RIS (T-RIS)** operates as a lens or a frequency selective surface, where the incident field is manipulated (by filtering, polarisation, beam splitting, etc.) and/or phase shifted, and re-radiated so as to control the refraction of plane impinging waves. Although RISs have great potential to implement advanced electromagnetic wave manipulations, only simple functionalities, such as electronic beam-steering and multi-beam scattering, have been demonstrated in the literature. Recently, some investigators have touched upon the possibility of deflecting the beam to achieve **simultaneous reflective-transmission RIS (RT-RIS)** [WDB18].

(a) R-RIS   (b) T-RIS   (c) Reflectarray   (d) Transmitarray
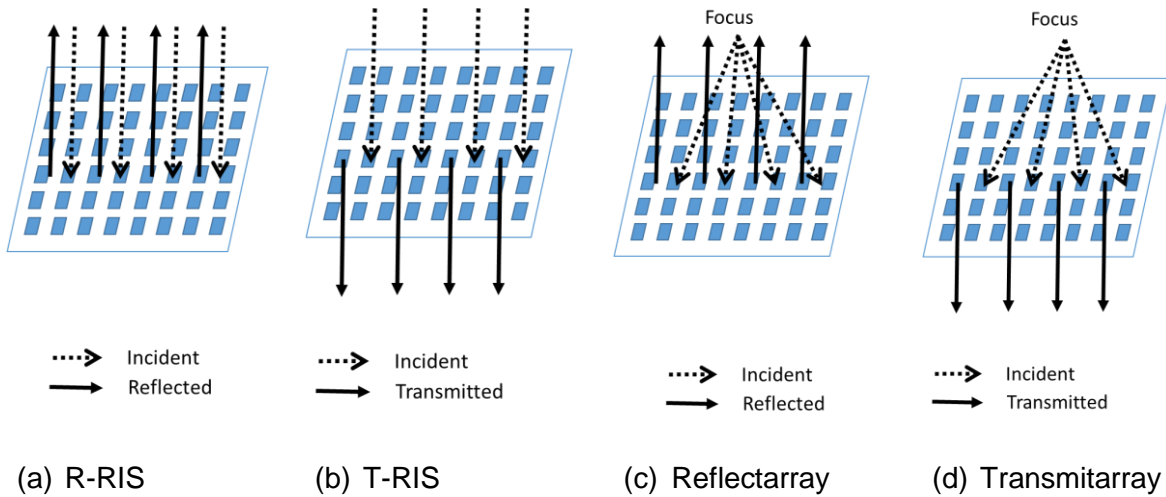
Figure 1-1 – RIS taxonomy

Several different antenna technologies (e.g., [GTB16], [SN17]) can be considered as RIS hardware technologies, including **reflectarrays** [HPC14], **transmitarrays** (e.g., [DCD20], [DCS20], [RVC19]), as well as smart, programmable or software-defined metasurfaces (e.g., [BMM20], [YCY16], [TBM14], [ZZZ10], and [DGL20]).

When the elements have both size and spacing **lower than 1/10th** of the communication operation wavelength, RISs are also **defined as metasurfaces** [GTB16]. Metasurfaces are artificial materials able to manipulate electromagnetic waves, in a way that cannot be performed in homogeneous materials. Simple functionalities enabled by metasurfaces include anomalous reflections or transmissions. Achieving **perfect** anomalous reflection and refraction is possible if metasurfaces are bianisotropic with weak spatial dispersion [AAT16]. Spatially dispersive metasurfaces are realized as artificial sheets, which are typically composed of metallic patches or dielectric engravings in planar or multi-layer configurations within subwavelength thickness. The interaction with electric and/or magnetic fields, is typically provided by resonant effects controlled by the geometry of the unit cells and their distribution, enabling antenna performance enhancement (beamshaping), flat lens, artificial magnetic conductors, cloaking, absorbers and scattering reduction. In particular, the introduction of programmable metasurfaces could realize intelligent environments---giving birth to the novel concept of Environment as a Service (ENVaaS)---where such metamaterials act as smart reflectors to enhance coverage and open new technical and business opportunities for beyond-5G (and 6G) networks.

Compared to classical phased arrays, which require phase-shifters and power amplifiers, RISs are generally passive radiative architectures integrating switches, RF-MEMS, p-i-n diodes, varactors, and/or liquid crystals, to control electronically the local surface phase-shift and/or impedance characteristics. So according to the technology of the unit cell (UC) we can distinguish **between active RIS**, where the reflected signal is amplified by an active element in UC, and **passive RIS,** where the UC is realized with low loss reactive components that are used to implement a prescribed phase shift, either continuous or quantized, resulting in low-energy device.

(a)   (b)
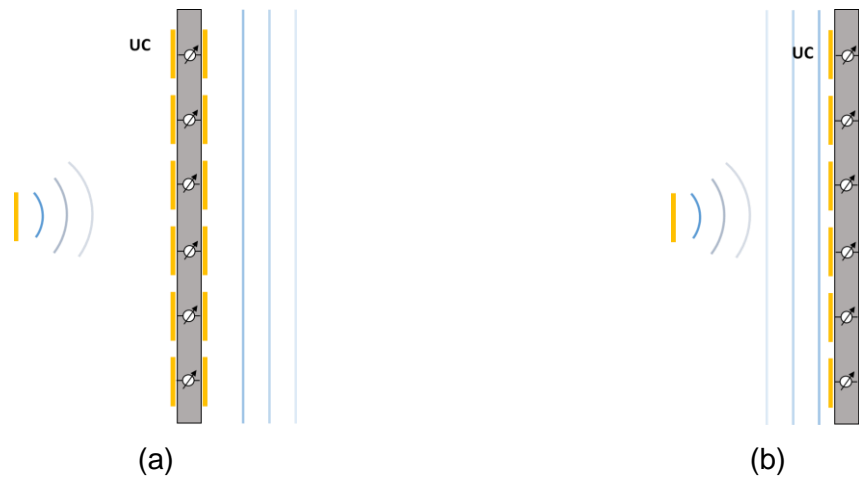
Figure 1-2 – Typical RIS passive architecture: T-RIS/Transmitarray (a), R-RIS/Reflectarray (b)

Finally, as for relays we can also distinguish different operating modes: **Regenerative RIS** that decode, regenerate and retransmit a copy of the original signal; **Non-Regenerative RIS** that act as analog repeaters by retransmitting the signal they receive (in some cases amplified through beamfoming techniques or active elements). A receiving RIS (RX-RIS) enables measurement collection at its site, through a single or few Receive (RX) Radio-Frequency (RF) chains attached to all or a subset of the its unit elements [AV20]. A hybrid surface (H-RIS) combines two of the above-mentioned modes, being able to reflect the impinging signal and simultaneously sense/measure a part of it [ASA21], [ZSA21].

In this context, RISE-6G investigate RIS over a wide span: suggested prototypes are mainly with UCs separation of half-wavelength. However, different studies include metasurfaces, e.g., dipole-based metasurfaces that considered to address the theoretical performance evaluation of RIS assisted wireless systems when the RIS is based on metasurface structures, i.e., including mutual coupling between subwavelength UCs. Prototypes of T-RIS, R-RIS and simultaneous RT-RIS are addressed theoretically and experimentally. From the technology point of view mainly passive RIS based on p-i-n diodes, RF-MEMS and varactors are addressed below 40 GHz. Above these frequencies, active UCs are considered too.

2   Basic RIS modeling

2.1   RIS full-wave electromagnetic simulations

The RIS prototypes developed in RISE-6G (and described in detail in Sec. 4 have been modelled and simulated in commercial electromagnetic software made available by the project Participants. This includes the platforms Dassault Microwave Studio and Ansys HFSS, both capable of calculating scattering and impedance parameters of R-RIS, T-RIS, Reflectarray and Transmittarray structure. The simulations have been performed using two methods, which enable the analysis necessary for the characterization of the RIS: i) single cell with periodic boundary conditions, implementing an infinitely extended planar structure, relevant for the prediction of the scattered field and far field radiation pattern of large RIS structures with thousands of unit cells; ii) finite structure with a limited number (tens to hundreds) of unit cells, relevant for the prediction of port based scattering and impedance matrices.

Full-wave simulations are important to capture the electromagnetic response of RIS unit cells operating at different reflecting states and frequency bands. As explained in Sec. 2.2, the global RIS response, necessary to develop EM based communication end-to-end (E2E) models, is built upon RIS unit cell models either performing homogenization among (quasi-)periodic arrangement of cells or describing mutual interactions among unit cells. It has been shown in the literature that full-wave simulations with method i) are predicted accurately by homogenization models [VCC18]. Although recent effort [PTH20] has confirmed the importance of method ii), further scientific research has been undertaken to develop and validate a simplified EM approach that ease the design of RISs and motivates the adoption of heuristic MIMO communication models [DDT21]. More specifically, the role of full-wave simulations in method i) is detailed in Sec. 2.3, while the role of full-wave simulations in model ii) is detailed in Sec. 2.4. The application and validation of the models in Sec. 2.3 and Sec. 2.4 are addressed in Sec. 2.5, where dedicated full-wave modelling activity has been carried out for the characterization of some RIS prototypes listed in section 4. Finally, the inclusion of fading from multipath propagation in indoors environments is developed into method ii) both via statistical and geometrical approaches in Sec. 3.

Before focusing on how the two methods are guided, applied, and validated by full-wave simulations, we introduce the rationale behind developing equivalent model in the context of communication-oriented design of RIS and array structures.

2.2 Equivalent RIS models

The EM response of the RIS types described in Figure 1-1 can be reproduced by an equivalent mathematical model that describes the collective transmission and reflection properties of arrays of reconfigurable unit cells. There are two main class of EM models that have been presented and developed in the scientific literature:

1) Continuous Model (CM), where homogenization methods are employed to derive equivalent boundary conditions of the global RIS structure. The model is presented in the form of impedance boundary conditions that relate electric and magnetic field components that are tangential to either side of the metasurface [YFY19]. This approach is suitable for R-RIS and T-RIS structures based on large reconfigurable metasurfaces, where a dense array of subwavelength unit cells is characterized by continuous electric and magnetic surface current sheets. This homogenization procedure is depicted in Figure 2-1. More specifically, the modelling activity of RISE-6G makes use of the generalised sheet transition conditions (GSTCs) that captures the magneto-electric effect of the metasurface unit cell through equivalent surface and admittance impedances. This will be used in Sec. 2.3 to develop in house finite difference time domain (FDTD) codes that describes the EM field scattered from the RISs. Interestingly, the equivalent response of the metasurface can be also obtained via full wave simulations in the form of equivalent tangential fields, which define equivalent the surface currents in Figure 2-1 from which the scattered field is generated and propagated.
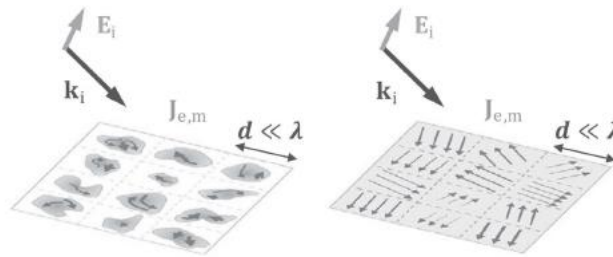
Figure 2-1 - Homogenization procedure applied to dense arrays of sub-wavelength metamaterials unit cells (reproduced from [DZD20]): An incident field E_i impinges onto the metasurface travelling along the direction dictated by the wave-vector k_i and equivalent electric J_e and magnetic J_m surface current densities are induced, which show variability on a sub-wavelength scale $d \ll \lambda$.

2) Discrete Model (DM), where the scattering properties of individual finite size unit cells are described in presence of nearby, mutually coupled, unit cells. The model is normally presented in matrix form and can be easily cast into a MIMO system model. In Sec. 2.4, models based on scattering and impedance matrices are presented. This approach is suitable for R-RIS, T-RIS, Reflectarray, and Transmittarray structures, and is appropriate to capture the response of individual unit cells with arbitrary (not necessarily periodic) arrangements within finite size structures. Interestingly, for metasurface-based structures, an alternative discrete formulation can be developed from suitable CMs by calculation of the equivalent tangential fields at macro-cell level, where unit cells are characterized in groups covering a RIS area of λ^2 . A DM model is then developed which accounts for the coupling among macro-cells and the radiation from the whole metasurface is calculated via antenna array theory.

Both the CM and DM formulations start from field-based solutions of the vector wave equation. For real-life structures as the prototypes reported in section 4 the obtained models are informed by full wave electromagnetic simulations of the individual antenna/unit cell, as described in Sec. 2.1. In limited cases treating idealized structures, e.g., dipole antenna/cell, the response function is known in closed mathematical form [GD21]. An example based on thin wire antennas will be discussed in detail in Sec. 2.4, with extensions to near field proximity and the presence of multiple RISs as well as passive (dipole-based) scatterers.

2.3 Continuous RIS models

We discuss two different methodologies to develop the RIS CM models, based on equivalent currents flowing through the metasurface upon incidence of an external radiation, into finite difference numerical schemes. This will facilitate: i) the integration of multiple and large RISs into propation channels with obstacles and walls; ii) the time domain analysis of the RIS response to wideband pulses.

2.3.1 T-RIS EM model by GSTCs and FDTD

We have started implementing a specific approach that has led to conceiving a CM of the RIS in the form of a locally modified FDTD scheme [VAC16].

In order to evaluate the performance of large scale RISs within wireless scenarios, an equivalent model of the underlying metasurface structure is needed for integration within full-wave EM simulation tools. The RISE-6G Participants AAU and CNIT (Ancona) have developed efficient FDTD codes over the last decades [MBM16]. We focus on T-RIS structures formed of planar metasurfaces, even though the code will be suitable for R-RIS modelling as well. The aim is to simulate RIS functionalities in terms of EM wave transformations, such as electromagnetic wave focusing, anomalous reflection, and controlled refraction. Figure 2-2 shows an arbitrary metasurface that transforms an incident wave into a reflected and transmitted wave with controlled amplitude and phase. It is further assumed that a RIS is thin with respect to the operation wavelength ($Lx \ll \lambda$). Therefore, the RIS is modelled as a zero-thickness current sheet that represents simultaneous tangential electric and magnetic field discontinuities.
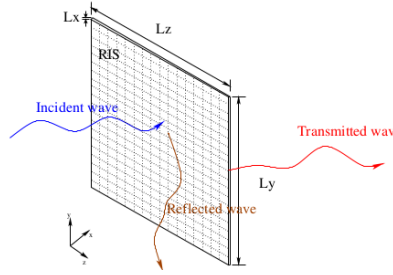
Figure 2-2 - Metasurface based RIS modelled in FDTD.

FDTD is a generally accepted and well-developed numerical method to analyze and design planar antenna structures. Briefly, the FDTD is based on the Yee method, which solves the Maxwell equations by iteration of discretized EM fields over a staggered numerical grid [BLY92]. The advantage of using time domain methods such as FDTD is that they compute the response of complex structures over a wide frequency range with a single simulation run [TAF95].

Due to electric and magnetic discontinuities introduced by metasurfaces, it is impossible to adopt the canonical Yee iterative scheme. In order to overcome this problem, a limited effort has been devoted to including the generalized sheet transition condition (GSTC) within FDTD algorithms. Considering the RIS depicted in Figure 2-2, where the RIS is placed between two identical media, the electric (E) field and magnetic (H) tangential fields are related to the electric and magnetic polarization densities, P and M respectively, by the following boundary conditions [VAC16]

$$\hat{x} \times \Delta \vec{H} = j\omega \vec{P}_{\parallel} - \hat{x} \times \nabla_{\parallel} M_x \qquad (2.1)$$

$$\Delta \vec{E} \times \hat{x} = j\omega\mu \vec{M}_{\parallel} - \nabla_{\parallel} \left(\frac{P_x}{\varepsilon} \right) \times \hat{x} \qquad (2.2)$$

$$\hat{x} \cdot \Delta \vec{D} = -\nabla \cdot \vec{P}_{\parallel} \qquad (2.3)$$

$$\hat{x} \cdot \Delta \vec{B} = -\mu \nabla \cdot \vec{M}_{\parallel} \qquad (2.4)$$

where $\nabla_\parallel = \left(\frac{\partial}{\partial z}\right)\hat{z} + \left(\frac{\partial}{\partial y}\right)\hat{y}$, **D** and **B** are the electric and the magnetic flux density respectively, $\boldsymbol{\varepsilon}$ is the electric permittivity whereas $\boldsymbol{\mu}$ is the magnetic permeability, $\boldsymbol{\omega}$ denotes the angular frequency and $\boldsymbol{j}$ denotes the imaginary unit.

In (2.1)-(2.4) the polarization densities are tensors related to the average tangential electric and magnetic fields as follows [VAC16]

$$
\begin{aligned}
\vec{P} &= \epsilon_0 \bar{\bar{\chi}}_{\text{ee}} \vec{E}_{\text{av}} + \bar{\bar{\chi}}_{\text{em}} \sqrt{\epsilon_0 \mu_0} \vec{H}_{\text{av}} \\
\vec{M} &= \bar{\bar{\chi}}_{\text{mm}} \vec{H}_{\text{av}} + \bar{\bar{\chi}}_{\text{me}} \sqrt{\frac{\epsilon_0}{\mu_0}} \vec{E}_{\text{av}}
\end{aligned}
\tag{2.5}
$$

where $\bar{\bar{\chi}}_{\text{ee}}, \bar{\bar{\chi}}_{\text{mm}}, \bar{\bar{\chi}}_{\text{em}} \ and \ \bar{\bar{\chi}}_{\text{me}}$ denote the electric and magnetic susceptibility tensors that express the response to the electric and magnetic excitation, whereas the subscript av stands for the average field on the metasurfaces' sides, ϵ_0 and μ_0 denote the free space permittivity and permeability respectively.

. Then, substituting the constitutive equations (2.5) in (2.1)-(2.4) we obtain an admittance tensor in matrix form [YFY19]

$$
\begin{pmatrix} \Delta H_y \\ \Delta H_x \\ \Delta E_y \\ \Delta E_x \end{pmatrix} = \begin{pmatrix} \tilde{\chi}_{ee}^{xx} & \tilde{\chi}_{ee}^{xy} & \tilde{\chi}_{em}^{xx} & \tilde{\chi}_{em}^{xy} \\ \tilde{\chi}_{ee}^{yx} & \tilde{\chi}_{ee}^{yy} & \tilde{\chi}_{em}^{yx} & \tilde{\chi}_{em}^{yy} \\ \tilde{\chi}_{me}^{xx} & \tilde{\chi}_{me}^{xy} & \tilde{\chi}_{mm}^{xx} & \tilde{\chi}_{mm}^{xy} \\ \tilde{\chi}_{me}^{yx} & \tilde{\chi}_{me}^{yy} & \tilde{\chi}_{mm}^{yx} & \tilde{\chi}_{mm}^{yy} \end{pmatrix} \cdot \begin{pmatrix} E_{x,\text{av}} \\ E_{y,\text{av}} \\ H_{x,\text{av}} \\ H_{y,\text{av}} \end{pmatrix}
\tag{2.6}
$$

The system (2.6) is underdetermined as it comprises four equations and 16 unknown susceptibilities, making it impossible to be solved directly. The $\tilde{\chi}$ symbols denote the frequency dependent surface susceptibility terms. Susceptibility tensors can be reduced according to the fundamental electromagnetic properties of the metasurface, i.e., reciprocity, loss and passivity. In fact, considering a reciprocal and lossless RIS allows for reducing the number of independent susceptibility components [ASC151, ASC152, AKG15, YFY19] to 4 unknowns.

We now discuss the inclusion of the GSTC (2.6) into the FDTD scheme. A well-known strategy to include thin material sheets in the Yee grid can be adopted for RIS structures. More precisely, the thin metasurface structure is collocated but between grid nodes, as shown in Figure 2-3 and Figure 2-4.
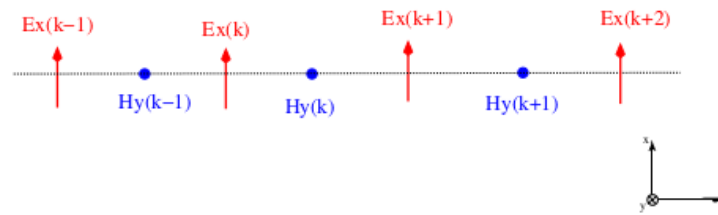
Figure 2-3 - Conventional 1-D FDTD Yee grid, propagation along the z axis.
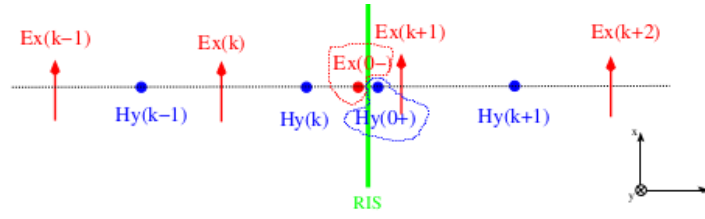
Figure 2-4 - Conventional 1-D FDTD Yee grid, RIS included as non-zero tickness structure placed at z=0, and addition of the two virtual nodes at z=0+ and 0-. Propagation along the z axis.

The 1-D scenario in Figure 2-3 and Figure 2-4 can be extended to 2-D and 3-D problems [VCC18]. Assuming the propagation occurs along the *z*-axis, the GSTC expressed in the time domain read [VCA18]

$$
\begin{aligned}
-\Delta H_y &= \varepsilon_0 \frac{d[\chi_{\text{ee}}^{xx} E_{x,\text{av}}]}{dt} \\
-\Delta E_x &= \mu_0 \frac{d[\chi_{\text{mm}}^{yy} H_{y,\text{av}}]}{dt}
\end{aligned}
\tag{2.7}
$$

For a correct FDTD run, virtual nodes with boundary conditions (2.7) must be added in the FDTD scheme, as depicted in Figure 2-4. In dealing with time domain derivative, we need to consider that the FDTD scheme is a "march-on-time" algorithm. Therefore, the update equation to solve the electric and magnetic fields must be causal. This implies a new formulation of the conventional FDTD update equations. Considering the electric field, while the conventional update equation is [VCA18]

$$
\begin{aligned}
E_x^n(k+1) &= E_x^{n-1}(k+1) \\
&+ \frac{\Delta t}{\varepsilon_0 \Delta z}\left[H_y^{n-\frac{1}{2}}(k+1) - H_y^{n-\frac{1}{2}}(k)\right]
\end{aligned}
\tag{2.8}
$$

the causal update equation with GSTC embedded in reads

$$
\begin{aligned}
E_x^n(k+1)A_{\text{ee}}^{xx,n} &= E_x^{n-1}(k+1)A_{\text{ee}}^{xx,n-1} \\
&+ \frac{\Delta t}{\varepsilon_0 \Delta z}\left[H_y^{n-\frac{1}{2}}(k+1) - H_y^{n-\frac{1}{2}}(k)\right] \\
&+ \frac{\chi_{\text{ee}}^{xx,n}}{2\Delta z}E_x^n(k) - \frac{\chi_{\text{ec}}^{xx,n-1}}{2\Delta z}E_x^{n-1}(k)
\end{aligned}
\tag{2.9}
$$

where

$$
A_{\text{ee}}^{xx,n} = 1 - \frac{\chi_{\text{ee}}^{xx,n}}{2\Delta z}
\tag{2.10}
$$

The same improvement holds for the magnetic field computation and these 1-D update equations can be easily extended to the more general 3-D case. The model will be extended to describe random EM fields generated within the RC for emulation of multi-path fading. Furthermore, the RIS-FDTD code will be important to carry out EMFEE performance assessment and testing as planned within the WP6 and WP7 activities.

2.3.2 R-RIS EM model by Huygens Box and FDTD

The RIS is assumed to be entirely enclosed in a Huygens' box with all the N RIS ports exposed (see Figure 2-5). The incoming wave from TX with fields $\vec{E}^{(TX)}$ and $\vec{H}^{(TX)}$ produces surface currents on the Huygens' box

$$\vec{J}_e^{(in)} = -\hat{n} \times \vec{H}^{(TX)} \tag{2.11}$$

$$\vec{J}_m^{(in)} = \hat{n} \times \vec{E}^{(TX)} \tag{2.12}$$

where $\hat{n}$ is the normal unit vector pointing out from the closed surface. Please note the opposite signs in (2.11) and (2.12) compared to usual Huygens box formulations—these are due to the currents radiating *inwards*. The fields $\vec{E}^{(TX)}$ and $\vec{H}^{(TX)}$ can be calculated analytically from the TX radiation pattern for arbitrary location of TX or assumed to have a form of a plane wave incident on RIS from arbitrary direction with θ or φ polarization. The latter method has been used for the prototype RIS modelling, as both TX and RX are assumed to be in the far field of RIS.
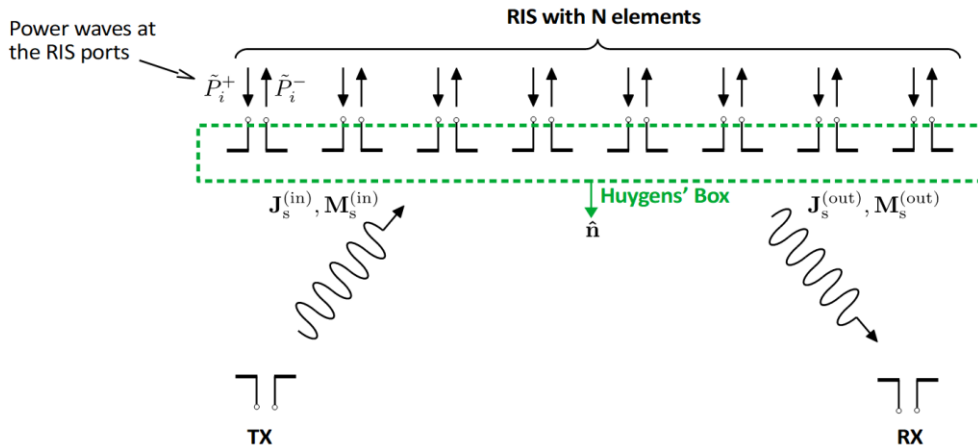
Figure 2-5 – Model of RIS based on Huygens' box with arbitrary number of RIS ports

For each set of incident fields and each i-th RIS port being excited by an incoming power wave $\tilde{P}_i^+$ the scattered fields $E^{(scat)}$ and $H^{(scat)}$ together with reflected power waves $\tilde{P}_i^-$ are calculated using electromagnetic simulation software. In our experiments we have used both the CST Microwave Studio with its T-, F- and I-solvers, and our AAU in-house EM simulation code AFC implementing the FDTD method. Obtaining the model requires in total $M + N$ simulations, where M is the number of TX positions, or alternatively the number of plane wave incidence angles for

both polarizations, and N is the number of RIS ports (equal to number of RIS elements if we limit ourselves to single port RIS elements).

The scattered fields are then again converted to equivalent surface currents, this time radiating *outwards*

$$\boldsymbol{J}_{\mathrm{s}}^{(\mathrm{out})} = \widehat{\boldsymbol{n}} \times \boldsymbol{H}^{(\mathrm{scat})} \tag{2.13}$$

$$\boldsymbol{M}_{\mathrm{s}}^{(\mathrm{out})} = -\widehat{\boldsymbol{n}} \times \boldsymbol{E}^{(\mathrm{scat})} \tag{2.14}$$

Now all outgoing waves can be calculated by near-to-far-field transform, either as a field in the position of RX, or as a collection of plane waves in arbitrary direction with θ or φ polarization if we assume RX to be in the far field of RIS.

With the above procedure, a generalized scattering matrix $\boldsymbol{S}$ can be obtained for any particular RIS. In our case, assuming plane waves, the matrix $\boldsymbol{S}$ has $M + N$ rows and columns, and fully characterizes the RIS with N ports for incoming and outgoing planes in M directions and for both polarizations. In practice, the plane waves are regularly distributed into directions in the entire space (or half-space for purely reflective RIS) and the stencil is governed by the highest spatial modes in the radiation of the particular RIS. The matrix $\boldsymbol{S}$ is eventually integrated with radiation patterns of TX and RX into a multi-point communication network using phasor transmission for- mulas.

The networking part is implemented as a function that outputs the total scattering or impedance matrix of the entire communication network, subject to input consisting of positions and orienta- tions of all the network elements: TX, RX and RIS. For constellations where the TX and RX positions do not fit into the planewave stencil of the matrix $\boldsymbol{S}$, linear interpolation is employed. Additional weighting coefficients can be added in each wireless link, emulating distorted propa- gation conditions (loss and delay) all the way down to NLOS scenarios.

The goal of the function is to be a useful cross-collaboration tool, because it can be easily used by researchers without background in electromagnetics as a "black box", while still being a phys- ical electromagnetic model inside. To this end, the function is now being used for channel char- acterization in RIS-augmented indoor environments together with WP4.

2.4 Discrete RIS models

2.4.1 T-RIS and Transmitarray scattering matrix and power budget

Bsides dealing with CM integration, we have developed a DM in the form of a hybrid full wave methodology based on scattering matrices. The outcome is an efficient numerical tool has been developed to define, synthetize, and optimize T-RIS and transmitarray antenna arrays.

In the proposed model, the focal source radiation pattern, the unit-cells scattering matrix, and their radiation patterns are used as input data for the in-house code that allows for computing the radiation performances of the entire array of (transmitting) unit cells. The input data can be

extracted by considering ideal unit-cells and focal sources, or alternatively by full-wave simulations.
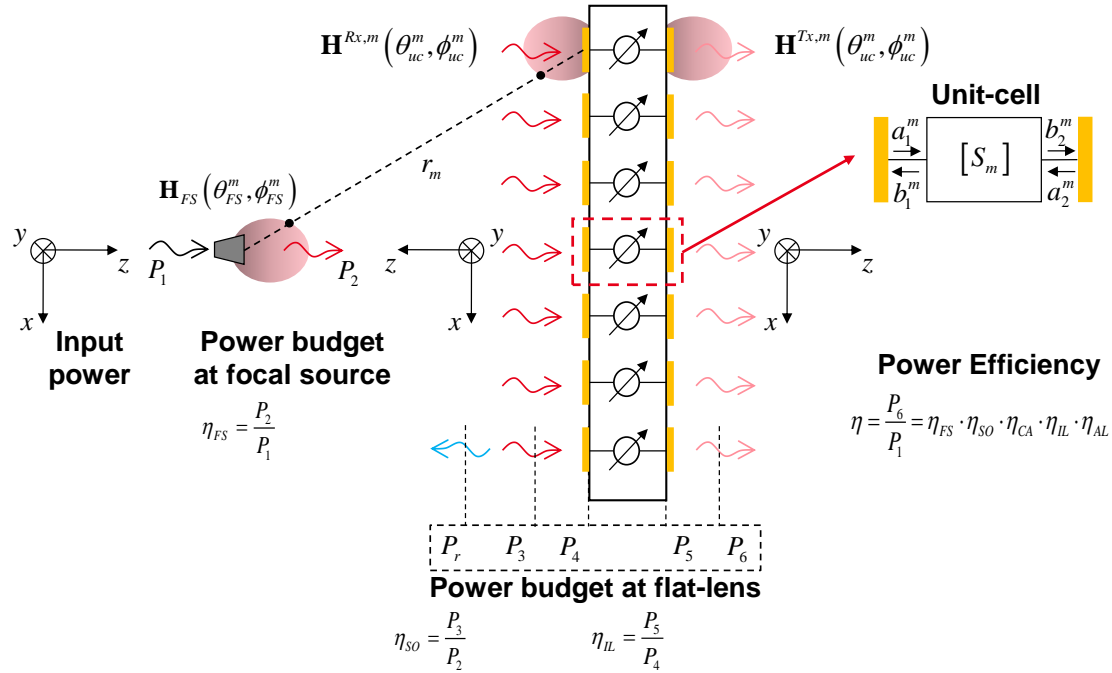
Figure 2-6 - Schematic view of a transmitarray and terms used in the numerical model.

Considering the structure of Figure 2-6, including M unit-cells, it is possible to define seven different power terms, defined as follows:

- P_1 is the input power on the focal source.

- P_2 is the power radiated by the focal source or by the focal array and is calculated considering the power density of the focal source $U_{FS}(\theta,\phi)$. Then, the focal source efficiency is calculated as $\eta_{FS} = P_2 / P_1$.

$$P_2 = \int_0^{2\pi}\int_0^{\pi} U_{FS}(\theta,\phi)\cdot\sin(\theta)\,d\theta d\phi \qquad (2.15)$$

- P_3 is the total incident power on the array aperture. Then, the spill-over efficiency is calculated as $\eta_{SO} = P_3 / P_2$. The incident power is calculated integrating the power radiated by the focal source on the array aperture.

- P_r is the total reflected power by the array aperture due to the non-perfect matching of the unit-cells. The mismatching of the unit-cell m is modeled considering its reflection coefficient $S_{11}^m(\omega)$. Considering the two-port model of the unit-cell in Figure 2-6

and the reflected power by the unit-cell m, we can calculate this term as $P_r = \sum_{m=1}^{M} P_r^m$, where

$$P_r^m = \left| b_1^m \right|^2 = \left| S_{11}^m(\omega) \cdot a_1^m \right|^2 \tag{2.16}$$

- P_4 is the collected or accepted power by the array aperture and is calculated considering the incident collected power by each unit-cell m ($P_4 = \sum_{m=1}^{M} P_4^m$). Consequently, the efficiency of the array in the receiver layer is calculated as $\eta_{CA} = P_4 / P_3$.

$$P_4^m = \left| a_1^m \right|^2 = \left| \sqrt{P_1} \frac{\lambda}{4\pi r_m} e^{-j\frac{2\pi r_m}{\lambda}} \mathbf{H}_{FS}\left(\theta_{FS}^m, \phi_{FS}^m\right) \cdot \mathbf{H}^{Rx,m}\left(\theta_{uc}^m, \phi_{uc}^m\right) \right|^2 \tag{2.17}$$

where $\mathbf{H}_{FS}\left(\theta_{FS}^m, \phi_{FS}^m\right)$ and $\mathbf{H}^{Rx,m}\left(\theta_{uc}^m, \phi_{uc}^m\right)$ represent the radiation patterns of the focal source and the receiving pattern of the unit-cell in the receiving side, respectively.

- P_5 is the transmitted power on the transmitting layer. It includes the insertion loss of the unit-cells. The term $\eta_{IL} = P_5 / P_4$ indicates the efficiency at the unit-cell level. Considering the two port model of the unit-cell in the **Erreur ! Source du renvoi introuvable.**, the transmission coefficients of the unit-cells $S_{21}^m(\omega)$, and the transmitted power by the unit-cell m we can calculated this term as $P_5 = \sum_{m=1}^{M} P_5^m$, where

$$P_5^m = \left| b_2^m \right|^2 = \left| S_{21}^m(\omega) \cdot a_1^m \right|^2 \tag{2.18}$$

- P_6 is the total radiated power by the T-RIS/transmitarray. The term $\eta_{AL} = P_6 / P_5$ indicates the efficiency of the unit-cell in the transmitting layer. This is calculated as $P_6 = \sum_{m=1}^{M} P_6^m$ and considering the coefficients $S_{22}^m(\omega)$

$$P_6^m = \left| b_{2tr}^m \right|^2 = \left| \sqrt{1 - \left| S_{22}^m(\omega) \right|^2} \cdot b_2^m \right|^2 \tag{2.19}$$

Considering these definitions, the antenna efficiency (ratio between realized gain and directivity) is calculated as:

$$\eta = \frac{P_6}{P_1} = \eta_{FS} \cdot \eta_{SO} \cdot \eta_{CA} \cdot \eta_{IL} \cdot \eta_{AL} \quad \eta = \frac{P_6}{P_1} = \eta_{FS} \cdot \eta_{SO} \cdot \eta_{CA} \cdot \eta_{IL} \cdot \eta_{AL} \tag{2.20}$$

In the proposed model, the gain of the transmitarray is extracted as:

$$G_{TA}(\theta,\phi) = \frac{U_{TA}(r,\theta,\phi)}{P_1/4\pi r^2} = \left| \sum_m b_{2tr}^m \mathbf{H}^{Tx,m}(\theta,\phi) \cdot e^{j\frac{2\pi}{\lambda}\sin(\theta)\cos(\phi)x_m} e^{j\frac{2\pi}{\lambda}\sin(\theta)\sin(\phi)y_m} \right|^2 \tag{2.21}$$

In (2.21) $\mathbf{H}^{Tx,m}(\theta_{uc}^m, \phi_{uc}^m)$ $\mathbf{H}^{Tx,m}(\theta_{uc}^m, \phi_{uc}^m)$ represents the radiation pattern of the unit-cell in the transmitting side.

2.4.2 R-RIS and Reflectarray impedance matrix and E2E model

In the first semester of the RISE-6G project, we further embraced the open challenge of developing an EM compliant DM, thus extending the limited yet remarkable research efforts reported in the scientific literature [PTH20, BG20, BKS19J]. A DM based on impedance matrices has been developed, which provides an operational E2E communication model for analysing and optimizing RIS-assisted wireless systems. The model is general in the sense that it captures the scattering of arbitrary N-port loaded RIS structures; it can be developed either from constitutive equations of antenna arrays and N-port scatterer [MH73], or from field solutions by moment methods [HVS17]. The caveats of applying this model to RIS prototypes devised in RISE-6G are elaborated in Sec. 2.5.

Initially, the impedance matrix DM has been computed and verified for a basic unit cell geometry: The thin-wire linear dipole antenna. The choice of thin-wire dipoles as RIS unit cells gives access to expressions of self- and mutual-impedances in closed mathematical form. For simplicity, both the transmit and the receive arrays are assumed to have thin-wire dipole radiation elements as well. Therefore, in such an all-dipole RIS assisted wireless link, complex-valued channel gains have a full theoretical prediction. The main features of the E2E model are: (i) derivation from Maxwell's equations and inclusion of generation, propagation, and scattering of the EM fields; (ii) inclusion of the joint amplitude and phase response of the unit cell, as well as mutual coupling between closely (subwavelength) spaced unit cells; and (iii) unique mapping between the voltages measured at the ports of a multi-antenna receiver and the voltages impressed at the ports of a multi-antenna transmitter. Thus, the proposed communication model is E2E, mutual coupling, and unit cell aware. More specifically, we introduce a circuit-based communication model for RIS-assisted wireless systems that is derived through the mutual impedances between all existing radiating elements (transmit/receive antennas and RISs) [PTG18]. We prove that the impact of (i) the incident EM fields (impressed by a generator or scattered/induced); (ii) the voltage generators at the transmitter and the load impedances at the receiver; and (iii) the tunable load impedances that control the passive scatterers of the RIS, is jointly considered and is explicitly unfolded in the proposed E2E communication model.

The derivation of the E2E DM model starts from identifying the port terminals of all the antenna radiating elements (of both transmitter and receiver antenna array) and RIS unit cells. After identifying port currents $[I_T, I_S, I_R]$ and voltages $[V_T, V_S, V_R]$, one writes the constitutive equations of transmit array, receive array, and RIS unit cell array in open circuit, viz.,

$$\begin{aligned}
V_T &= Z_{TT}I_T + Z_{TS}I_S + Z_{TR}I_R \\
V_S &= Z_{ST}I_T + Z_{SS}I_S + Z_{SR}I_R \\
V_R &= Z_{RT}I_T + Z_{RS}I_S + Z_{RR}I_R
\end{aligned} \tag{2.22}$$

Besides the presence of self-impedances, $[Z_{TT}, Z_{SS}, Z_{RR}]$, it is worth noticing that the constitutive equations are coupled to each other via mutual impedances $[Z_{TS}, Z_{TR}, Z_{SR}]$, for which reciprocity holds. We seek for a linear relation between received and transmitted voltages in the form

$$V_R = \mathcal{H}_{E2E} V_T \tag{2.23}$$

Eliminating the RIS impedances yields the complex valued channel gain between transmitter and receiver

$$\mathcal{H}_{E2E} = \left(1_{N_R \times N_R} + \mathcal{P}_{RSR} Z_L^{-1} - \mathcal{P}_{RST} \mathcal{P}_{GTST} \mathcal{P}_{TSR} Z_L^{-1} \right)^{-1} \mathcal{P}_{RST} \mathcal{P}_{GTST} \tag{2.24}$$

with propagating matrices defined as

$$\mathcal{P}_{GTST} = Z_G + \mathcal{P}_{TST} \tag{2.25}$$

$$\mathcal{P}_{XSY} = \mathcal{Z}_{XY} - \mathcal{Z}_{XS}(Z_{\text{RIS}} + \mathcal{Z}_{SS})^{-1} \mathcal{Z}_{SY} \tag{2.26}$$

where, in (2.24)-(2.26), Z_G and Z_L denote the generator and load termination impedance, respectively. Generator and load terminations of $50\,\Omega$ are used in the computation throughout this section. The Z_{RIS} denotes the termination of the RIS unit cells, which will be varied under an optimisation algorithm to achieve the optimal operation state of the RIS. Note that Z_G, Z_L and Z_{RIS} are diagonal matrices. Interestingly, the model configures as a MIMO communication model of the composite channel (both LOS and virtual LOS through the RIS) between antenna arrays and RIS.

The result in (2.24) is reported as **Theorem 1.** In [GD21], where a detailed proof is given. Furthermore, in **Corollary 1.** [GD21], an asymptotic approximation for the far-field communication in SISO systems is found as

$$\mathcal{H}_{E2E} = \mathcal{Y}_0(\mathcal{Z}_{RT} + \mathcal{Z}_{RS}\Phi_{SS}\mathcal{Z}_{ST}) \tag{2.27}$$

where

$$\boldsymbol{\mathcal{Y}_0} = \boldsymbol{Z_L}\,(\boldsymbol{Z_L} + \boldsymbol{\mathcal{Z}_{RR}})^{-1}(\boldsymbol{Z_G} + \boldsymbol{\mathcal{Z}_{TT}})^{-1} \tag{2.28}$$

with Z_L and Z_G load and generator impedances respectively, $\mathcal{Z}_{RR}$ and $\mathcal{Z}_{TT}$ input impedance of Rx and Tx antennas respectively, denotes the mismatching factor at both transmitter and receiver, and

$$\boldsymbol{\Phi_{SS}} = (\boldsymbol{\mathcal{Z}_{SS}} + \boldsymbol{Z_{RIS}})^{-1} \tag{2.29}$$

denotes the state of the RIS, established by both the (full rank) mutual impedance matrix $\mathcal{Z}_{SS}$ and the equivalent circuit model captured by the (diagonal) RIS impedance of the circuitry loading the ports of passive RIS unit cells $\boldsymbol{Z_{RIS}}$.

The wireless communication link that we model is depicted in Figure 2-7, showing the interaction (impedance) matrices present in the far-field approximation of the E2E model in (2.27)-(2.29).
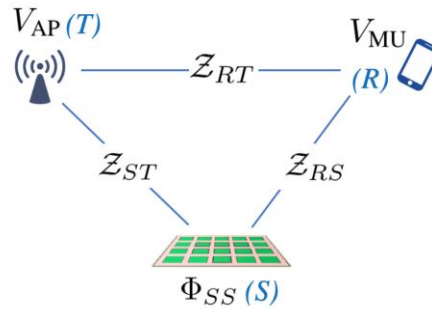
Figure 2-7 - Interaction impedances for RIS-assisted wireless link.

2.4.2.1 Numerical examples with dipole-based R-RIS

Let us consider the wireless system in Figure 2-8, in which a transmitter with N_T antennas and a receiver with N_R antennas communicate through an RIS that is made of $N_S = M \times N$ passive scatterers. For illustrative purposes, the transmit antennas, the receive antennas, and the passive scatterers are cylindrical thin wires of perfectly conducting material whose physical length is ℓ and whose radius $a \ll \ell$ is finite but negligible with respect to ℓ (thin wire regime). The inter-distance between adjacent radiating elements is denoted by d. All thin wires are co-polarized, but the model is general enough to consider any radiating element and passive scatterer that operates within the minimum scattering antennas [PTG18].
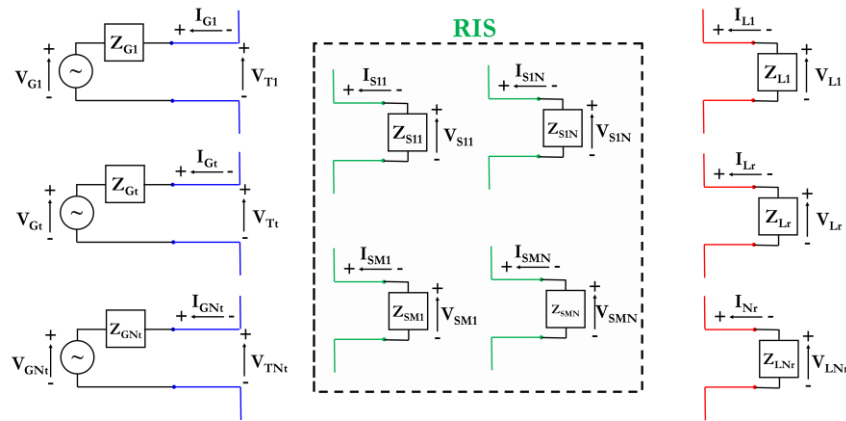
Figure 2-8 - Thin-wire dipole based RIS-assisted wireless link.

Full-wave simulations have been adopted to implement this all-dipole communication system, where a RIS-assisted SISO wireless communication link has been created to verify and test the limits of the impedance-based DM. The implemented system is depicted in Figure 2-9.

The verification has been done using the method of moments implemented in CST Microwave Studio. As depicted in the upper part of Figure 2-9, the TX and RX dipoles are positioned at arbitrary positions with respect to RIS array. In this model, the dipoles are modelled either as cylinders or as wires of varying radii, all co-polarized. The impedance matrix of the entire system is in good agreement with the analytical thin-wire model when the dipole radii converge to zero.
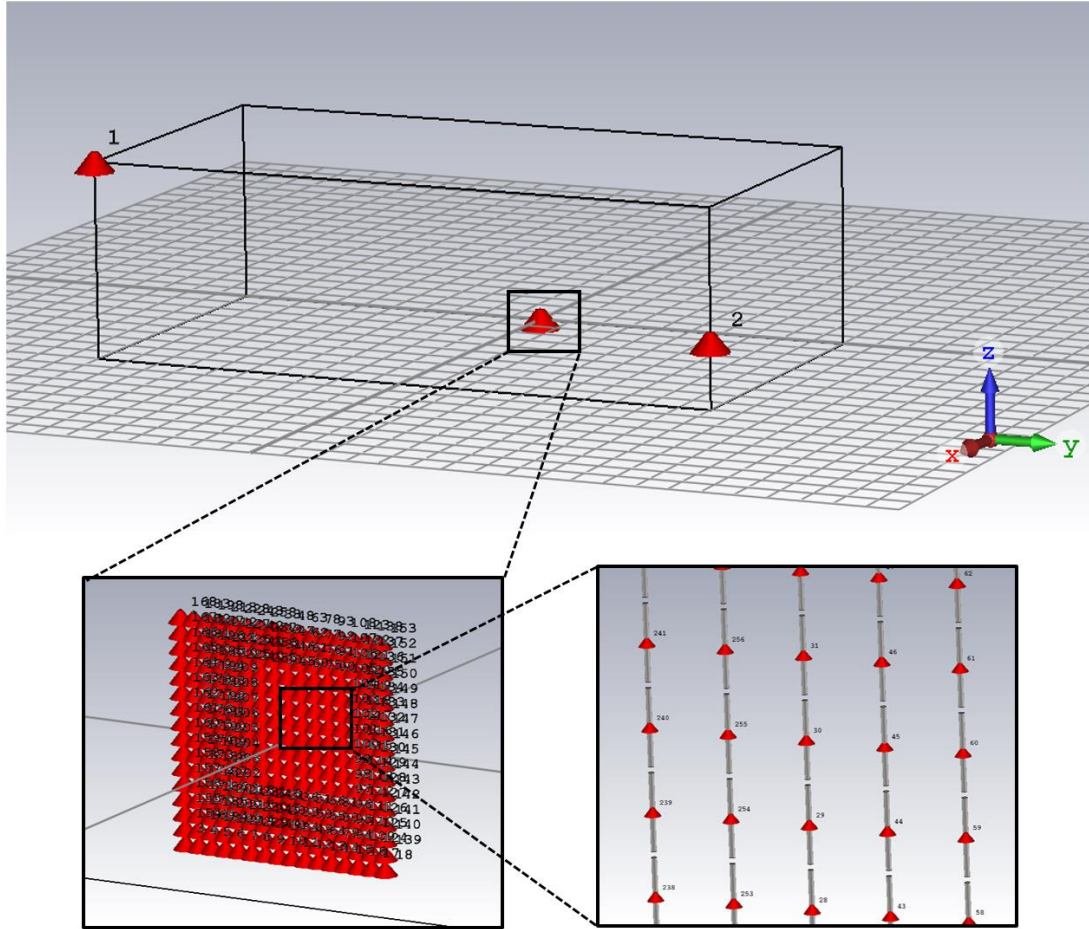
Figure 2-9 - Full-wave simulation of the thin-wire dipole model using CST Microwave Studio.

The model has been further exploited to understand the role of mutual coupling in communication-oriented optimization procedures. Inherently, the channel gain of the dipole-based RIS-assisted SISO wireless link has been computed using well known expressions of self- and mutual-impedance of thin wire linear antennas. More explicitly, the diagonal entries of the impedance matrices $\mathcal{Z}_{SS}$, $\mathcal{Z}_{RS}$, and $\mathcal{Z}_{ST}$ configure as self-impedances of form $Z_s = R_z + jX_s$ of the infinitesimally thin-wire dipole of total physical length $\ell = \lambda_0/2$ operating at $k_0 = 2\pi/\lambda_0$ is given as

$$R_S = \frac{\Gamma - \text{Ci}(2\pi) + \ln(2\pi)}{4\pi\varepsilon_0 c} \;\; ; \;\; X_S = \frac{\text{Si}(2\pi)}{4\pi\varepsilon_0 c} \tag{2.30}$$

The off-diagonal entries of the impedance matrices $\mathcal{Z}_{SS}$, $\mathcal{Z}_{RS}$, and $\mathcal{Z}_{ST}$ configure as mutual impedance of form $Z(r) = R_A(r) + jX_A(r)$, and show high frequency dependence on the separation distance r while it depends weakly on ℓ,

$$R_A = \frac{2\text{Ci}\left(\frac{2\pi r}{\lambda_0}\right) - \text{Ci}(\xi+\pi) - \text{Ci}(\xi+\pi)}{4\pi\varepsilon_0 c} \;\; ; \;\; X_A = \frac{-2\text{Si}\left(\frac{2\pi r}{\lambda_0}\right) + \text{Si}(\xi+\pi) + \text{Si}(\xi-\pi)}{4\pi\varepsilon_0 c} \tag{2.31}$$

Where $\xi = \pi\sqrt{1 + 4r^2/\lambda_0^2}$

In (2.30) (2.311), $\text{Ci}(\cdot)$ and $\text{Si}(\cdot)$ denote the cosine and sine integral functions respectively. The constant ε and Γ are the vacuum electric permittivity and Euler constants, respectively.

Consider the RIS-assisted wireless MIMO link of Figure 2-10, where all-dipole transmit and receive antenna arrays are positioned at different heights and communicate through an all dipole RIS (with green elements).
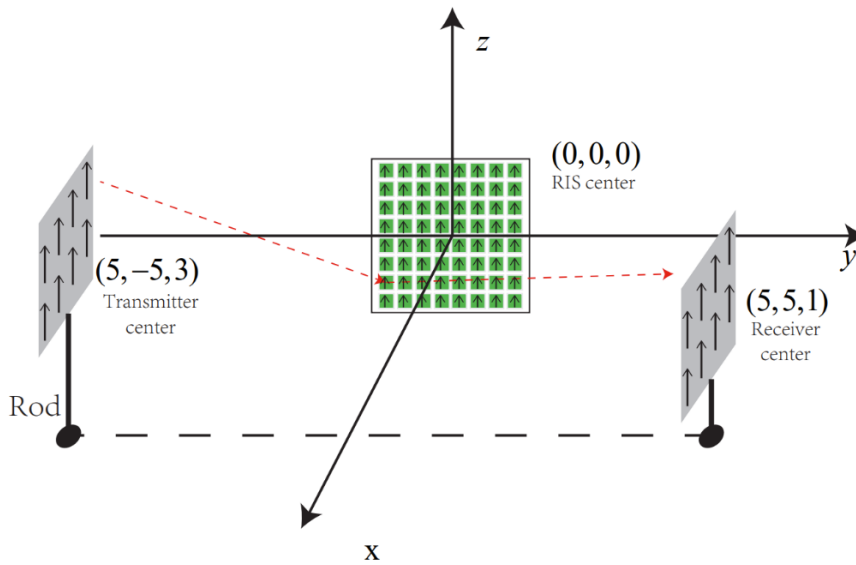
Figure 2-10 - RIS-assisted all-dipole MIMO wireless link.

 Figure 2-11 shows the numerical results of channel gain against the spacing between RIS unit cells for a planar array of dipoles loaded with arbitrary impedance values, parameterized with the number of RIS unit cells. It can be noticed that close spacings between unit cells give rise to an improvement of one or two order of magnitudes in the power transferred across the SISO link. Also, increasing the number of elements within the same physical area improves the channel gain via mutual coupling, and the performance of a RIS with ideal (non-quantized) impedance control gets close to the performance of a continuous tile as pointed out in [NJS21].
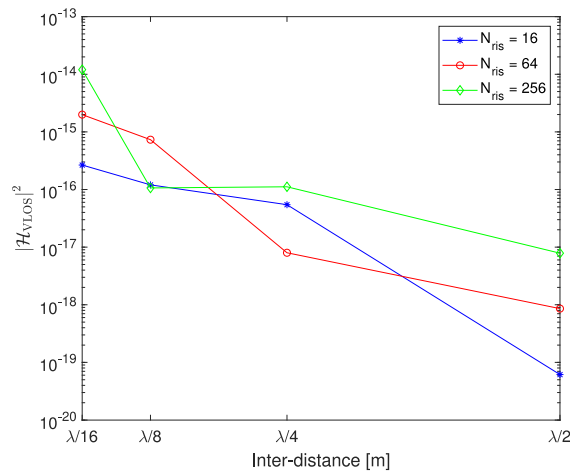
Figure 2-11 - RIS-assisted MIMO Wireless Link operating in a closed environment.

The importance of considering the mutual coupling between RIS unit cells has been the subject of a more in-depth study concerning the optimisation of the RIS using the channel model (2.27)-(2.29). It is found that higher channel gains could be achieved if mutual coupling is included as a constrains in the optimization procedure. This is shown in Figure 2-12 and more details can be found in [QD21].
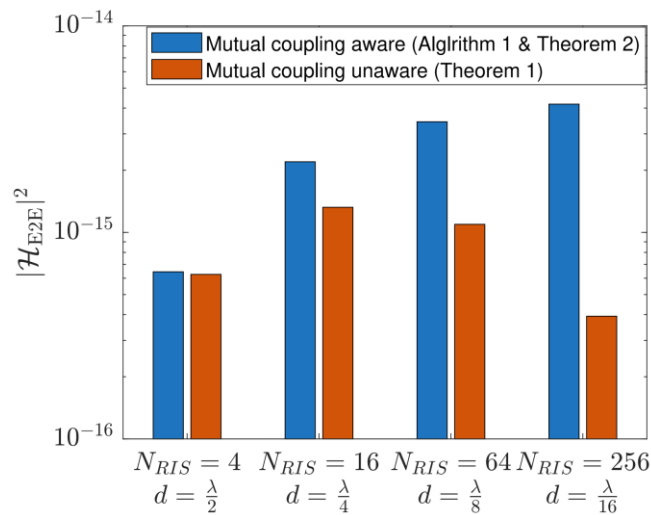
Figure 2-12 - RIS-assisted MIMO Wireless Link operating in a closed environment.

RIS modelling offers simple yet effective circuit-based representations of distributions of sub-wavelength particles. We expect the active impedance matrix $\mathcal{Z}_{SS}$ to become diagonal for large RISs with a high density of unit cells per wavelength, hence only the input impedance of a unit cell with periodic boundary conditions is required to populate the E2E model. Therefore, a simplified equivalent circuit of (unloaded, untuned) unit cells radiating within a metasurface structure can be adopted to derive the input impedance that populated the active impedance matrix diagonal. Inherently, resonant unit elements are described as LC resonators in circuit theory of a meta-surface. They exhibit frequency dispersive property and can be either active or passive

(driven by voltage or excited by an electric or magnetic field). Examples of such particles are the Split-Ring Resonators (SRRs) [SMS06], the Electric LC (ELC) [SPV00] resonators and their Babinet equivalents Complementary SRRs (CSRRs) [FLL04], and the Complementary ELCs (CELCs) [HGS08]. Each subwavelength meta-surface element can be modeled as a polarizable dipole with an equivalent RLC response, and its frequency response takes the following Lorentzian form [MBI17]

$$a(f) = \frac{Ff^2}{f_0{}^2 - f^2 + j\kappa f} \qquad (2.32)$$

where F, f_0, and κ are the element-dependent oscillator strength, resonance frequency, and damping factor. By externally controlling $f_0 = \frac{1}{2\pi \sqrt{LC}}$ where L, C are the inductance and the capacitance of the equivalent circuit, which can be succeeded by modifying the geometry of the metamaterial element, modifying the local dielectric environment, or by integrating lumped passive or active elements into the circuit for each unit element [SYM17], the meta-surface becomes a Reconfigurable Intelligent Surface (RIS) [HC09]. The quality factor of the resonant meta-surface QF is introduced as the ratio $\frac{\omega_0}{\kappa}$ relating to the bandwidth and the magnitude of $a(f)$. In Figure 2-13, the element response magnitude is presented versus a range of frequencies. Two different values for the angular resonance $\omega_0 = 2.75\ GHz$ and $3.5\ GHz$ are selected as well as three different values for the quality factor $QF = 10, 25,$ and 50. It is observed that the response function always peaks at ω_0 and as the QF becomes larger, the bandwidth becomes smaller and the magnitude larger. Considering a passive N-element RIS, the frequency representation of the output signal at the n-th element is given by:

$$r_n(\omega) = \phi_n(\omega) y_n(\omega) \qquad (2.33)$$

where $y_n(\omega)$ is the DTFT equivalent of the baseband received signal $y_n[t]$ at that element and $\phi_n(\omega)$ denotes the DTFT of (2.32) which is given by:

$$\phi_n(\omega) = \frac{F_n \omega^2}{\omega_n^2 - \omega^2 + j\kappa_n \omega} \qquad (2.34)$$

where ω is the discretized angular frequency, and ω_n is the angular resonance frequency. In vector notation, $r(\omega) \in C^{N \times 1}$ is the output signal at all N RIS elements:

$$r(\omega) = \Phi(\omega) s(\omega) \qquad (2.35)$$

where $\Phi(\omega) = \text{diag}\{\phi_1(\omega), \dots, \phi_N(\omega)\}$ and $s(\omega) \in C^{N \times 1}$ contains the input signal at all N RIS elements.
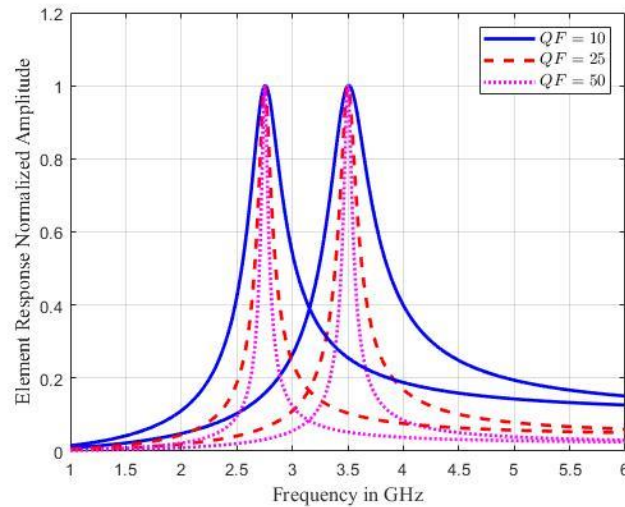
Figure 2-13 - The element response magnitude of a resonant unit element versus a range of frequencies for different values of ω_0 and QF.

Further work will be devoted to understanding the relation between the frequency dependent (wave) response (2.34) with the (port) RIS state matrix (2.29). Furthermore, we will develop an end-to-end model that incorporates a wideband wave reflection coefficient that accounts for the quality factor of specific RIS unit cells.

2.4.2.2 Near field R-RIS effects

A simple, yet representative, model has been developed to show the role of RIS in improving the channel diversity even where multi-path fading is not profitable, i.e., where the communication configures within the near field of the transmitter. Figure 2-14 illustrates a 2x2 MIMO antenna communication system scenario. The two Tx dipole elements and the two Rx dipole elements are arranged in a parallel configuration. However, due to the isotropic radiation pattern of linear antennas, and assuming the two TX dipoles do beamform towards Rx (and RIS), the LOS signal reaching the Rx is weak. Therefore, a question is whether the RIS retro-reflector can improve the strength of the received signal while improving channel diversity. We remark that also the RIS is modelled as an array of co-polarized dipoles, in parallel configuration with the Rx antenna elements. In Figure 2-14 the Tx and Rx dipoles, as well as the RIS array, are denoted by red, blue and green bullet points, respectively.
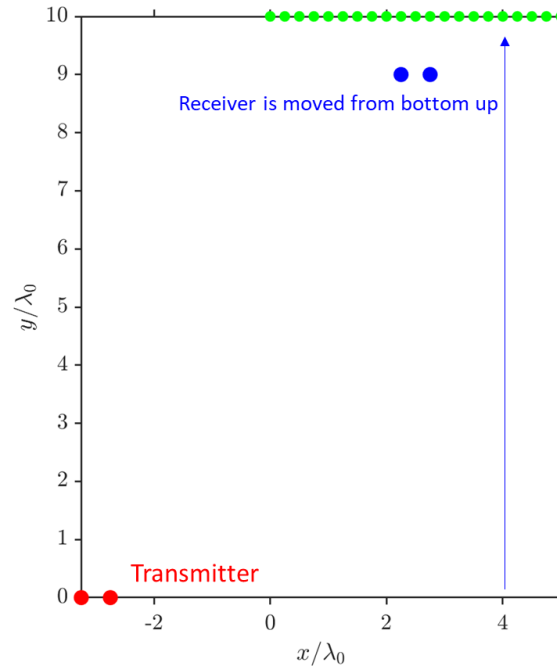
Figure 2-14 - RIS-assisted MIMO wireless link operating in a quasi-open environment. Each dot represents a (half-wavelength) dipole in co-polarized configurations.

Using (2.27)-(2.29) the antenna impedance matrix has a block structure that reflects the spatial configurations of Tx (*T*), Rx (*R*), and RIS (*S*) dipoles, viz.,

$$\mathcal{Z} = \begin{bmatrix} \mathcal{Z}_{TT} & \mathcal{Z}_{TS} & \mathcal{Z}_{TR} \\ \mathcal{Z}_{ST} & \mathcal{Z}_{SS} & \mathcal{Z}_{SR} \\ \mathcal{Z}_{RT} & \mathcal{Z}_{RS} & \mathcal{Z}_{RR} \end{bmatrix} \tag{2.36}$$

Based on the configuration in Figure 2-14, the communication figure-of-merit is calculated based on the E2E communication channel matrix $\mathcal{H}_{E2E}$, given in (2.27)-(2.29).

Figure 2-15 shows the Shannon Channel Capacity C computed for the $\mathcal{H}_{E2E}$ channel matrix for various distances of the Rx from the RIS array. Three different RIS termination have been considered as the non-optimal cases, i.e., as if the ports of all the RIS dipoles are terminated to open (5×10^5 Ω), matched (50 Ω) and short (0 Ω) circuit load. The Shannon capacity has been calculated as

$$C = \log_2 \left[\det \left(1 + \frac{\rho}{n} \mathcal{H}_{E2E} \mathcal{H}_{E2E}^{\dagger} \right) \right] \tag{2.37}$$

It can be observed from Figure 2-15, that the capacity C is flat and less fluctuating, with a starting point at ~0.005 bit/s/Hz, suggesting that LOS between Tx and Rx dominates. As the separation distance between Tx and RX increases, the role of the RIS becoming more evident. Furthermore, Figure 2-15 implies that regardless of the RIS termination, the RIS improves the communication capacity as the Rx antenna gets closer to the RIS while getting further away from the Tx.
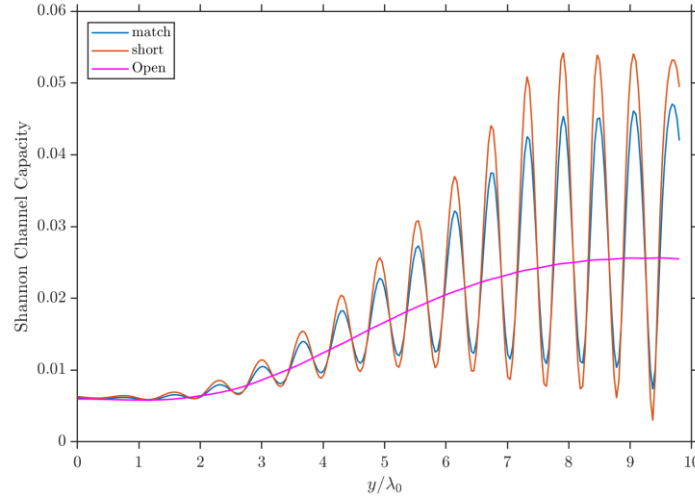
Figure 2-15 - Shannon Capacity of wireless MIMO communication in the presence of RIS array.

To further to investigate the role of RIS, the diversity of the communication channel is computed as the effective rank R_{eff} [V07] of the E2E channel matrix:

$$R_{eff} = \exp[-\textstyle\sum_i \sigma'_i \ln(\sigma'_i)], \ \sigma'_i = \frac{\sigma'_i}{\sum_i \sigma'_i} \tag{2.38}$$

where σ'_i are the eigenvalues of the Grahm matrix $\mathcal{H}_{E2E}\mathcal{H}^{\dagger}_{E2E}$. The behaviour of the diversity is shown in Figure 2-16 also as the function of distance y. Regardless of the RIS termination impedance, the diversity R_{eff} coalesce when the Rx gets close to the RIS, implying that the communication is dominated by the RIS. The opposite occurs when the Rx gets close to the Tx: There are more equally strong communication channels. However, the maximum diversity is achieved at intermediate distance gathering contributions from both the direct LOS and the virtual LOS, thus exploiting the full composite channel.
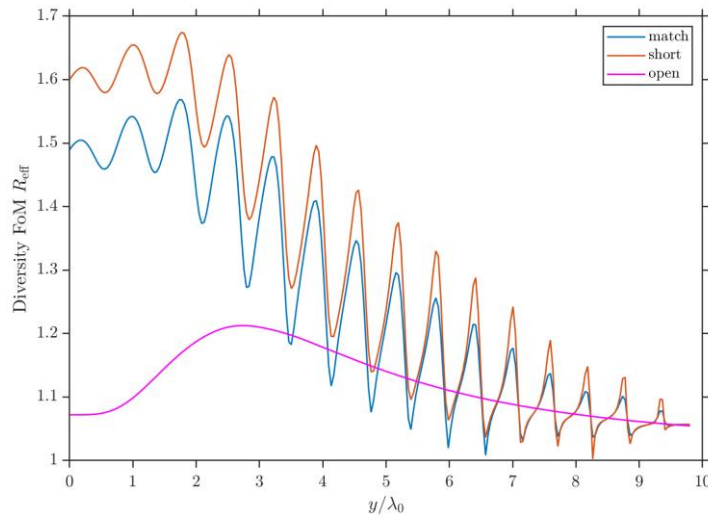
Figure 2-16 - Diversity of wireless MIMO communication in the presence of RIS array.

2.4.2.3 Multiple R-RIS and passive scatterer model

The impedance model has been generalized to include the presence in the propagation channel of both multiple RISs and obstacles. This extends the model relevance to beyond LOS in free-space, paving the way to modelling real-life quasi-free-space scenarios. The extension starts from noticing that $\mathcal{Z}_{SS}$ has a block diagonal structure, with square block matrices augmenting the self-impedances (diagonal) entries.

$$\mathcal{Z}_{SS} \leftarrow \begin{bmatrix} \mathcal{Z}_{SS} & \mathcal{Z}_{SS,SC} \\ \mathcal{Z}_{SS,SC} & \mathcal{Z}_{SC} \end{bmatrix} \tag{2.39}$$

Also, since in (2.39) the sub-script S has been used to index the non-transmitting nor receiving dipoles of the RIS, this will correspond to the presence of both passive scatterers and RIS arrays within the channel. The matrices $\mathcal{Z}_{ST}$ and $\mathcal{Z}_{RS}$ need to be augmented accordingly. The end-to-end channel transfer function model given in (2.27)-(2.29) is general and with minimal modification can be used to model the presence of obstacles in addition of RISs. Sec. 3.2 will demonstrate the use of the generalised model described here to model the impact of *randomly* positioned obstacles in RIS-assisted propagation channels.

The workflow of modelling the communication between Tx, Rx and RIS in the presence of obstacle starts with the calculation of self and mutual (radiation) impedances of all the radiating components including obstacles. That is, here, obstacles are considered to have self and mutual impedances calculated at virtual ports whose terminals. The so obtained self- and mutual impedances can be embedded into $\mathcal{Z}_{SX}$ or $\mathcal{Z}_{XS}$ where X can be of transmitter or receiver. The termination impedance $\mathcal{Z}_{RIS}$ appearing in (2.29), will then be modified to include the termination of the obstacle via

$$\mathcal{Z}_{RIS} \leftarrow \begin{bmatrix} \mathcal{Z}_{RIS} & \mathbf{0} \\ \mathbf{0} & \mathcal{Z}_{\text{obstacle}} \end{bmatrix} \qquad (2.40)$$

Finally, $\mathcal{Z}_{\text{obstacle}}$ has been assumed to be short-circuited, i.e., $\mathcal{Z}_{\text{obstacle}} = 0$, in order to mimic the scatterer passivity. It is important to note that the modification described here has assumed that obstacle elements are indeed passive and non-reconfigurable, while RIS elements are reconfigurable via tunable loads. This allows for the calculation of an end-to-end transfer function following the model .

The test case considered in our study is illustrated in Figure 2-17. In this case, a RIS (green dipoles) is placed at $y = 7\lambda$ away from the transmitter Tx (red dipole) and receiver Rx (blue dipole). The RIS has N_G unit elements with separation of 0.25λ. The square obstacles are made of cluster of (black) dipoles, as well, also 0.25λ apart for a total obstacle width of 3λ. The obstacles can be rotated to create dynamic fading.
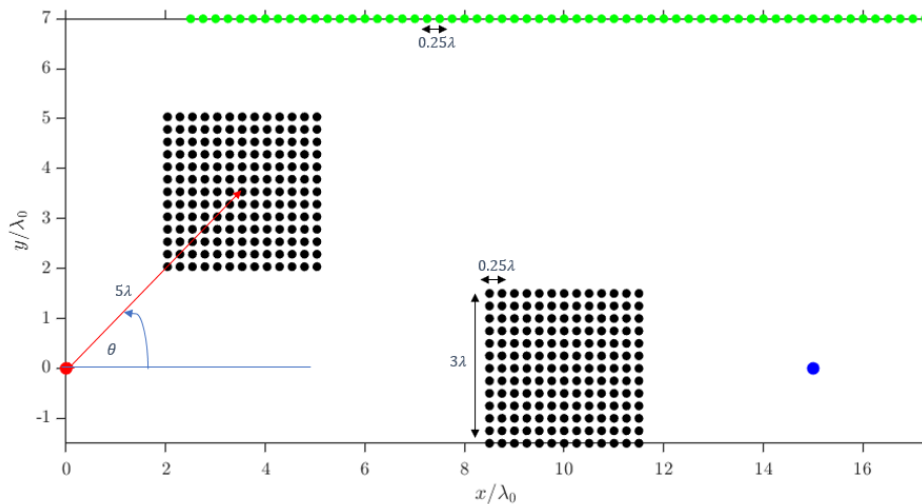
Figure 2-17 - SISO communication in the presence of rotatable obstacle.

Based on this configuration, the impedance matrix (2.40) and the gain of the H_{E2E} are calculated for different number of RIS unit elements, N_G. Here, the RIS is assumed to be terminated either by all short-circuits (0 Ω), open-circuits (50×10^9 Ω) or matched loads (50 Ω), see Figure 2-18. An optimisation algorithm is being developed in collaboration with the Partner NEC based on error estimate minimisation approach that employs RISs to equalize the channel.
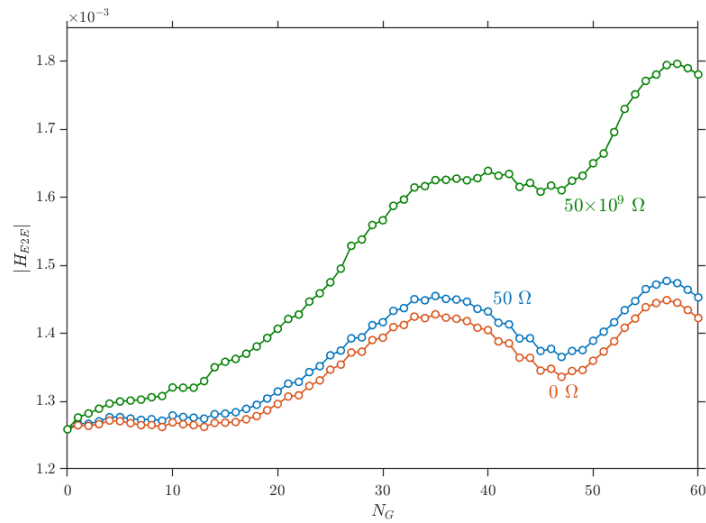
Figure 2-18 - Communication gain in the presence of obstacle and RIS.

The impact of the rotating the obstacle has also been considered. The obstacle will create a shadow region towards the RIS from the Tx at $\theta = 0$ that completely obstructs the direct line of sight at $\theta = 0.25\pi$. This is shown in Figure 2-19.
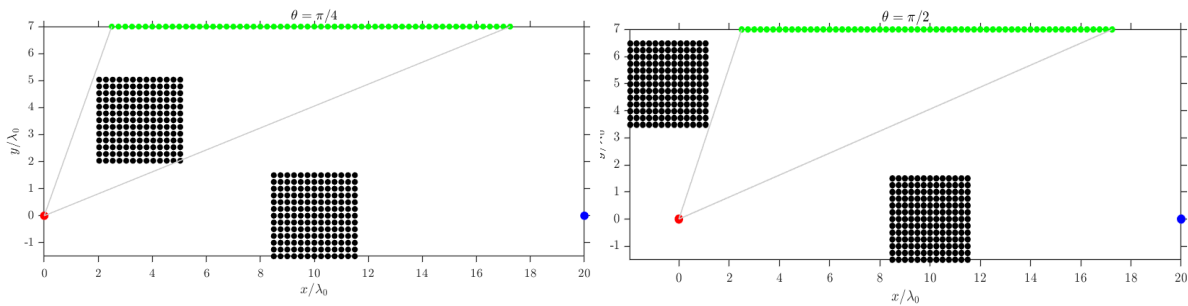
Figure 2-19 – Movable obstacle creating NLOS (left) and LOS (right) between the transmitter and the RIS.

Figure 2-20 shows the improvement of the channel gain with in the RIS-assisted communication link. Here, the RIS unit elements are terminated by optimal loads obtained by a genetic algorithm for each value of θ. The case where there is no RIS is included for comparison.
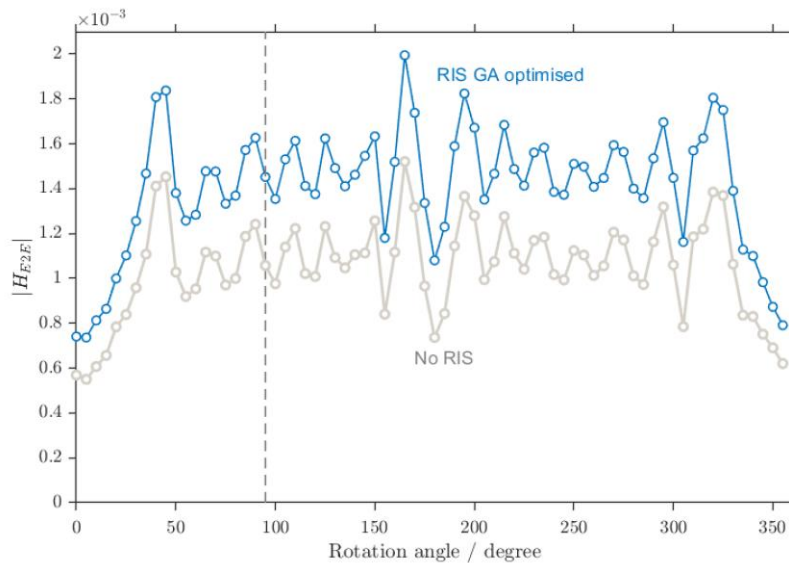
Figure 2-20 - Rotating the obstacle around the transmitter.

2.5 Application to RIS designs and model validation

2.5.1 Impedance Model of GNW R-RIS prototypes: Sub-6 GHz

The simulation layout for the RIS prototype 1) is reported in Figure 2-21 and consists of two co-polarized linear dipole antennas in the far-field of a RIS with 2x2 unit cells. The Tx and Rx dipole antennas, as well as the RIS, operate at a frequency of 5.2 GHz; the numerical simulations were therefore performed over a wide frequency bandwidth ranging from 4 to 6 GHz. The unit cell design used to conveniently simulate this finite size R-RIS has been developed by GNW and has the topology of two folded dipoles. The prototype has been simulated through CST Dassault Microwave Studio. The method that we used to verify the E2E model starts by extracting the impedance matrices identified in Sec 2.4.2. The interactions between Tx/Rx antenna and RIS unit cells is calculated by a frequency domain solver in the form of open circuit impedance matrices. It is interesting to point out that to build the end-to-end matrix, we have defined discrete ports within the unit cells. Those ports are left in open circuit or terminated by an equivalent circuit of the p-i-n diode in turn. Given that each unit cell has two p-i-n diodes, one for each wave polarization, only the folded dipoles co-polarized with the Tx and RX dipoles have will be used for RIS reconfiguration. However, the general impedance matrix of the E2E system in this configuration consist of 10 total ports: 8 that will be used for RIS configuration via p-i-n diodes, with the 8 diodes replaced by discrete ports, plus the two feed ports of the dipole antennas. The resulting impedance matrix will therefore have dimensions 10x10.
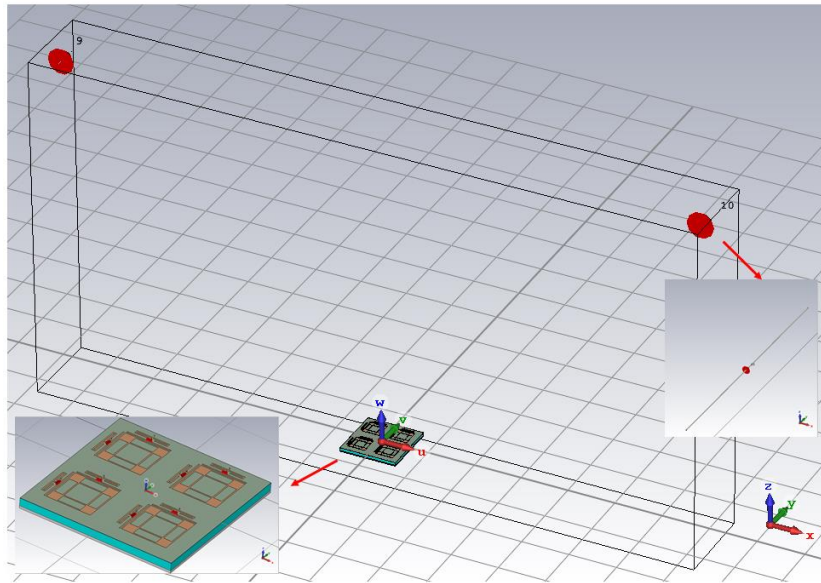
Figure 2-21 - Simulation layout of the RIS prototype provided by GNW.

An independent simulation has been carried out to extract the complex valued voltage-to-voltage channel gain between the two linear dipole antennas, with RIS unit cells loaded by the equivalent circuit of a p-i-n diode, either in ON or OFF state, as detailed in Sec. 2.4. The simulation layout of the RIS has been reported in Figure 2-22 together with the equivalent circuits of the p-i-n diodes.
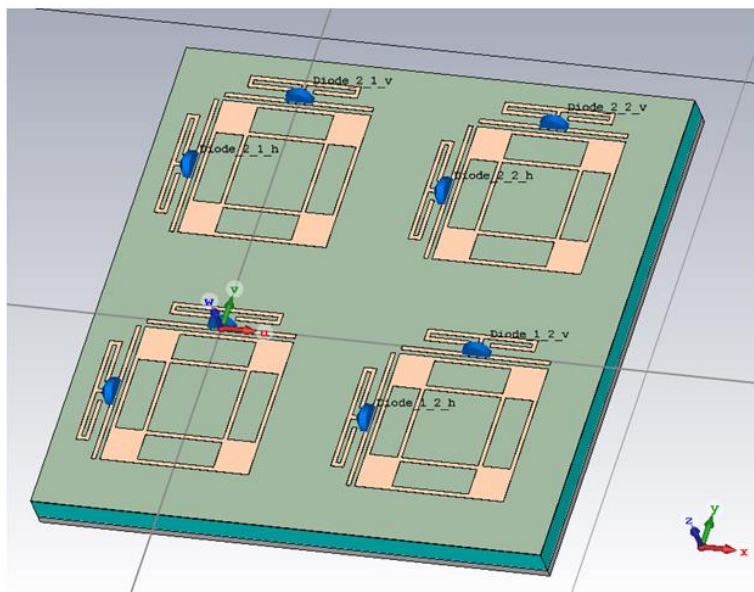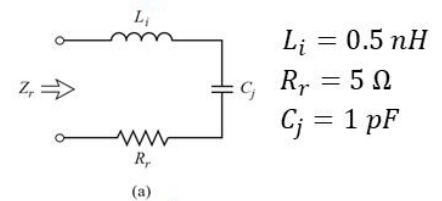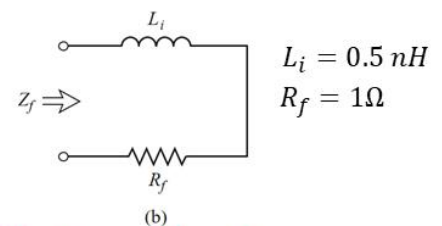
Figure 2-22 - RIS unit cells loaded by the equivalent circuit of a p-i-n diode.

Figure 2-23 reports a satisfactory comparison between the predicted channel gain obtained with the impedance model in Sec. 2.4, specialised to the RIS prototype 1) - referred to as $|H_{E2E}|$ - and the composite channel gain obtained from full-wave simulation for a selected distribution of unit cell loadings – referred to as $|Z_{21}|$. The p-i-n diodes denoted by subscript letter h in Figure 2-22, placed along x-axis, are in ON state, while those arranged along the y-axis, denoted by letter v, are in OFF state.
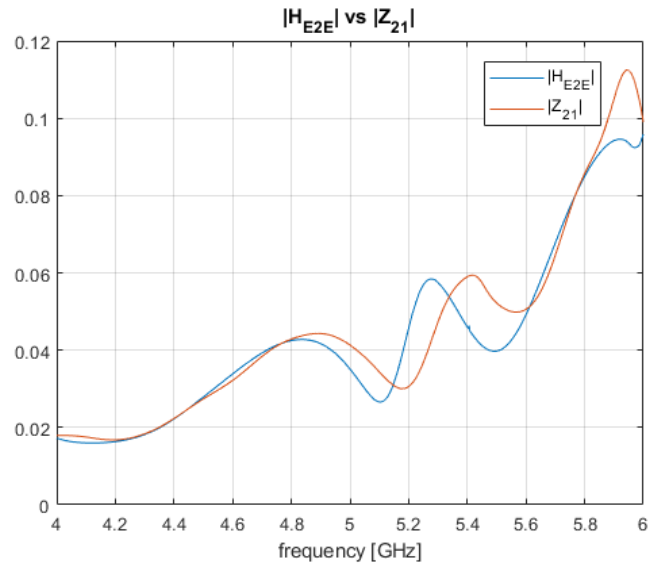
Fig-

2.5.2   Impedance Model of CEA R-RIS prototypes: mmWave

The
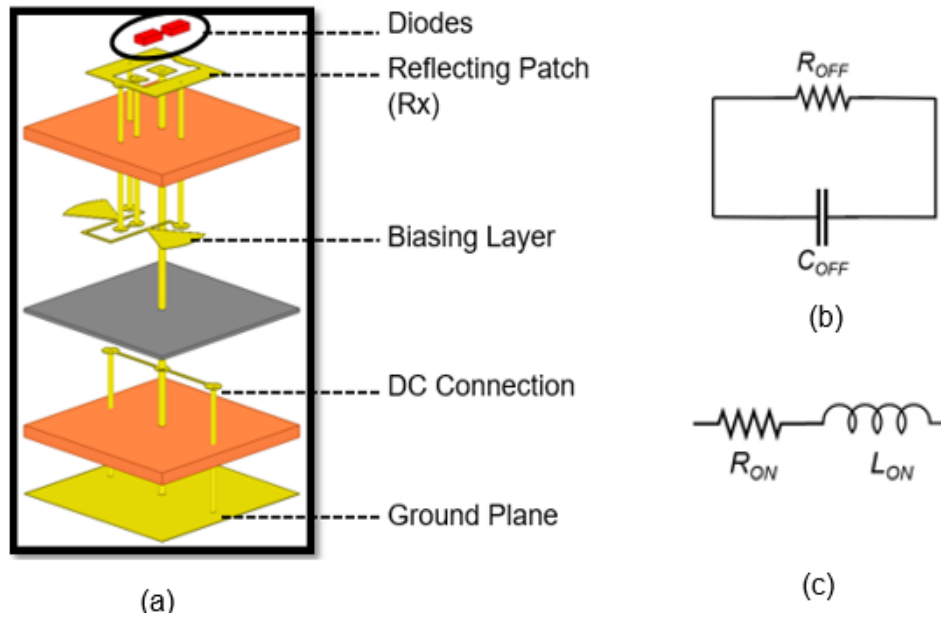
Fig-

The approach used to validate the End-to-End transfer function model given in $\mathcal{H}E2E = \mathcal{Y}_0(\mathcal{Z}_{RT} + \mathcal{Z}_{RS}\Phi_{SS}\mathcal{Z}_{ST})$ (2.27)-$\Phi SS = (\mathcal{Z}_{SS} + \mathcal{Z}_{RIS})⧄ - 1⧄$ (2.29), starts by establishing all impedance matrices presented in the HE2E model such as Z_{RT} related to the impedance between the Receiver and the Transmitter, Z_{RS} is the impedance related to Receiver dipole antenna and the R-RIS structure, Z_{ST} is the impedance related to the R-RIS structure and transmitter dipole antenna, Z_{RIS} is the impedance of the R-RIS structure obtained by switching diode states, , Z_{SS} is the active impedance obtained with discrete ports which replaced the diodes positioned in the R-RIS. To generate all impedances described in the use of the general HE2E model, all scenarios are simulated in Ansys EM HFSS can be described as follows in Figure 2-25:

- Scenario 1: In this configuration, all active elements in the R-RIS unit cell are changed by lumped ports and the dipole antennas are also excited with lumped ports: the general impedance matrix with all ports (10 ports) is extracted with Matlab to calculate the End-to-End transfer function model H_{E2E} of the system. The resulting active impedance Z_{SS} matrix has 10x10 dimensions (8 ports in the R_RIS Structure and 2 in the dipole antennas)

- Scenario 2: The second configuration is presented by active elements placed in 2×2 R-RIS unit cells which are biased in State 000 and only the dipole antennas R/T are excited with lumped ports. Consequently, the impedance Z_{21} (the impedance of the receiver-transmitter) is extracted to be compared with H_{E2E} calculated from the simulation Multi-ports elements.

- Scenario 3: The third configuration is presented by the active elements placed in 2×2 R-RIS unit cells which are biased in State 180 and only the dipole antennas R/T are excited with lumped ports. Therefore, the impedance Z_{21} (the impedance of the receiver-Transmitter) is extracted to be compared with the End-to-End transfer function model H_{E2E}.
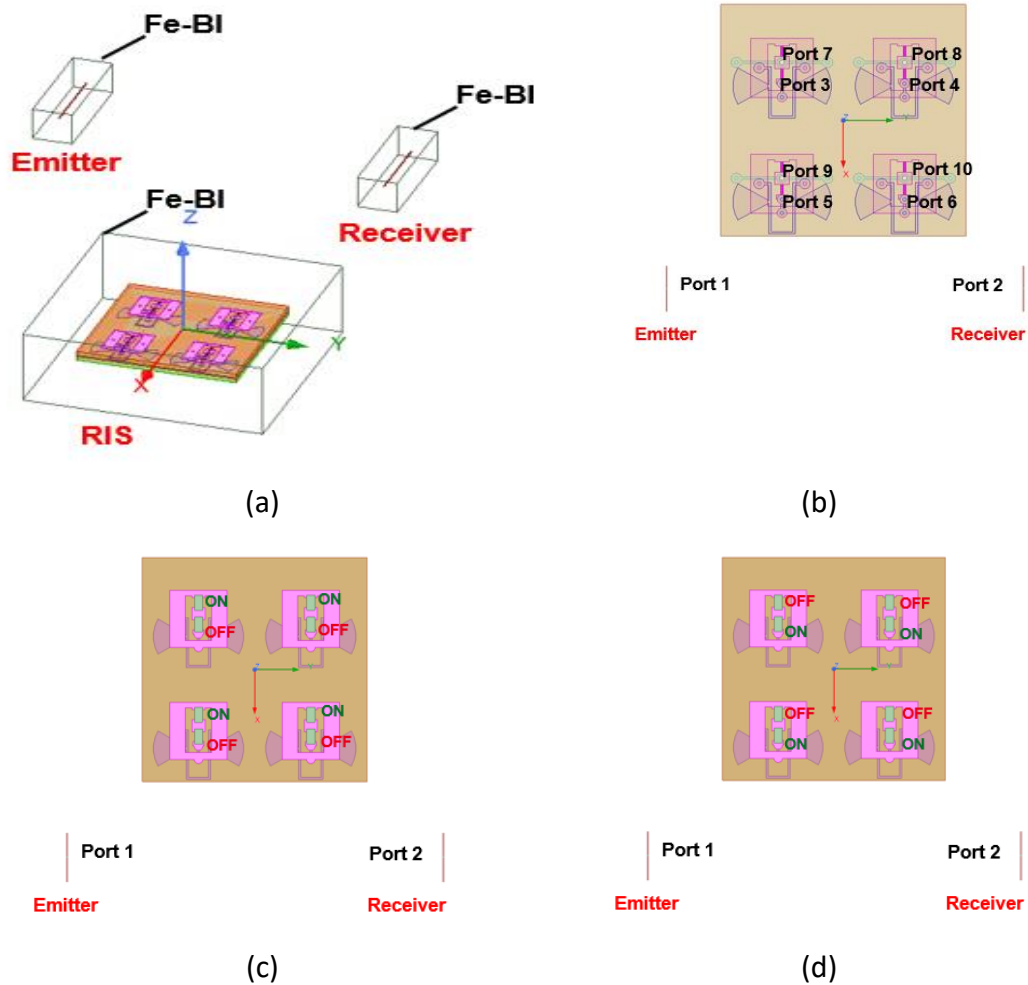
Figure 2-25 (a) Simulation layout of the R-RIS prototype provided by CEA, (b) Multi-ports R_RIS configuration, (c) R-RIS Configuration in state 0°, (d) R-RIS Configuration in state 180°.

In this section, we report the comparison between the predicted End-to-End transfer function obtained with the proposed model in Sec. 2.4.2, applied to the R-RIS design and the impedance Z_{21} extracted from Ansys HFSS obtained with simulations of the loaded RIS in the two states. The simulation results of impedance model has been extracted with a Matlab script, which outputs the total scattering or impedance matrix of the multi-port configurations to validate the End-to-End transfer function model HE2E. As we can see, the impedance modal plots referred to as proposed model are in good agreement with the Z_{21} extracted from the Ansys HFSS simulation with diodes in 0° state cases. Furthermore, we have also extracted active impedance from the unit cell placed in Periodic Boundary Conditions and used this approach to validate the proposed HE2E transfer modal in the infinite case of R-RIS arrays.
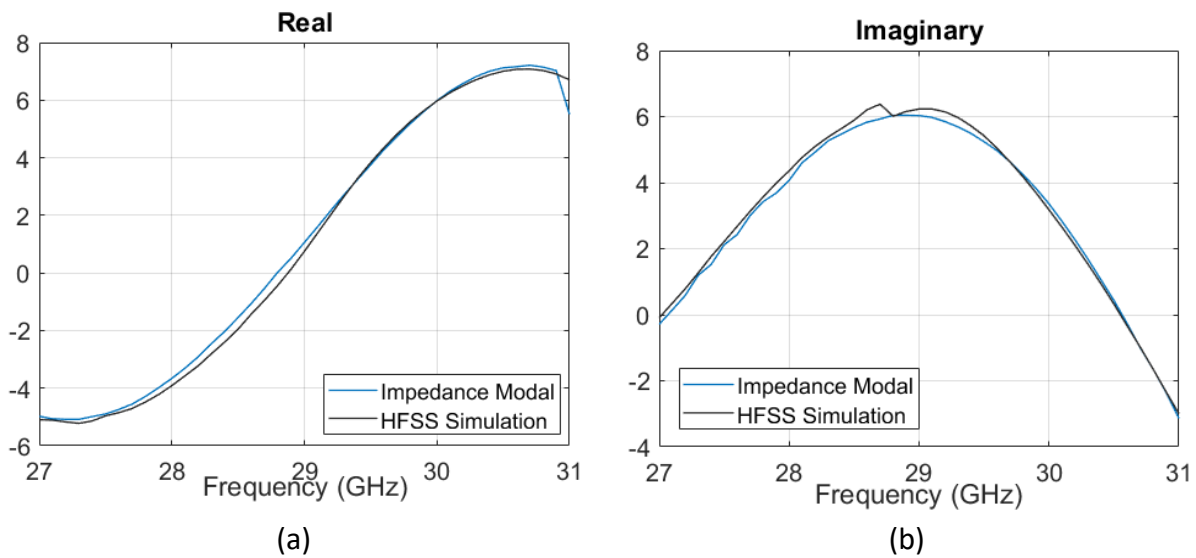
Figure 2-26 Comparison between the Impedance model (blue solid curve) and the predicted impedance Z_{21} extracted from HFSS Simulator obtained with simulations of the loaded RIS (solid black curve) in case 0: Real part (a), Imaginary Part (b)

Additionally, the Periodic boundary Condition (PBCs) are often desired for approximating a large R-RIS structure by using one unit cell. PBCs can be used in Ansys HFSS Software to imitate the characteristics of an infinite array of identical unit-cells.

The R-RIS 1 bit unit cell is presented in the form of PBCs that relate electric and magnetic field according to the structure that are tangential to either side of the proposed unit cell. This method is suitable for R-RIS structures based on large reconfigurable R-RIS arrays.

The active impedance Z_{SS} results obtained with the infinite boundary condition of the unit cell will be used and repeated to create a diagonal form matrix and to validate the End-to-End transfer function obtained with the proposed model in Sec. 2.4.2.

Figure 2-27 reports the results of the End-to-End transfer function obtained with the proposed impedance model and the impedance extracted from HFSS Simulator obtained with simulations of the 2×2 R-RIS unit cells compared to the model used the Z_{SS} impedance extracted from PBCs in the one of two cases. As we can see, the impedance modal plots referred to as proposed model are in good agreement by using Z_{SS} extracted with PBCs infinite boundary conditions. Hence, this approach validate the proposed HE2E transfer modal in the infinite case of R_RIS arrays.

(a)

(b)
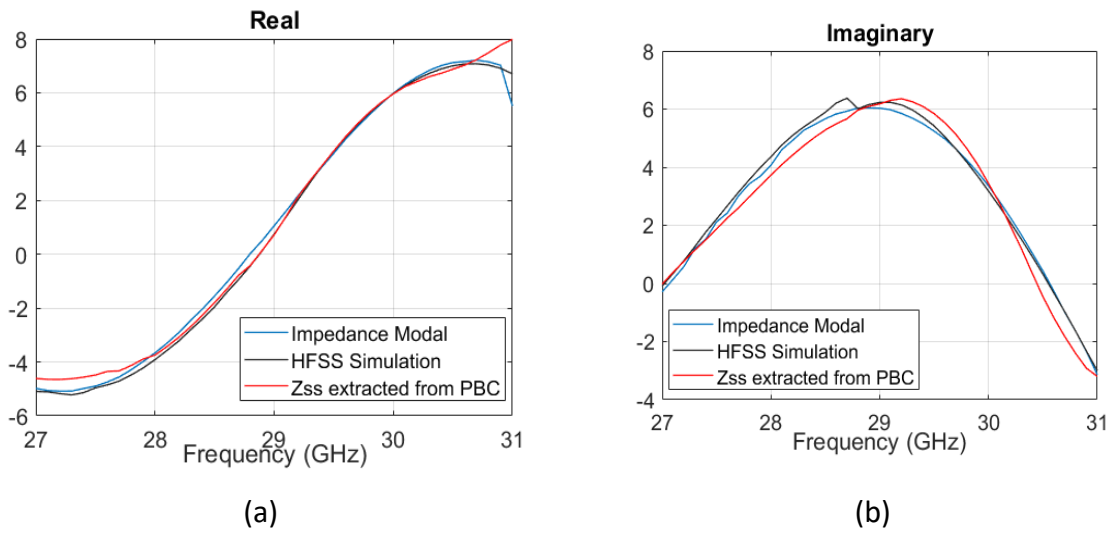
Figure 2-27 Comparison between the Impedance model (blue solid curve) and the predicted impedance Z_{21} extracted from Ansys HFSS Software obtained with simulations of the loaded RIS (solid black curve) and the Z_{SS} impedance extracted from PBCs in case 0° (Red solid curve): Real part (a), Imaginary Part (b)

3   RIS channel modeling and sounding

In this section we present the different modelling approaches to include RIS in the radio channel environment. Most of them are independent of frequency and can be translated to target wavelength. The sounding in real environment and reverberation chamber is limited to a set of frequencies around 28 GHz and 3.5 GHz.

3.1   Random Coupling Model for NB fading inclusion

The operation of RIS-assisted antenna arrays inside highly reflecting environments is considered as depicted in Figure 3-1 RIS-assisted SISO Wireless Link operating in a closed environment Figure 3-1, where the composite channel between transmitter and receiver is formed of a direct LOS and a VLOS through the RIS.
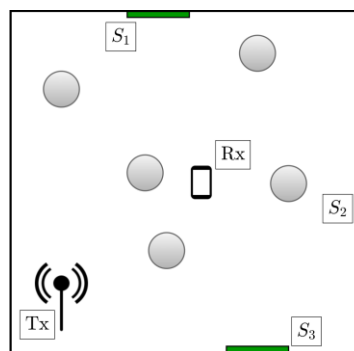
Figure 3-1 RIS-assisted SISO Wireless Link operating in a closed environment

The EM waves leave the transmit array, bounce around the room and arrive at the receive array via multiple propagation paths generated by wall/object reflections. The wireless transmission in confined environments is thus clearly affected by rich multipath fading. This impairment is underpinned by the geometry of the room, as well as by the EM material characteristics of walls and objects within the room. In high frequency wireless systems, EM waves propagate form many, tens to hundreds, wavelengths before hitting a wall or an object inside the environment. Upon interference, the EM field form a myriad of stationary waves that co-exist within the room confined space and whose distribution change as boundary condition change. This form of mixing is clearly a complex process, which is highly sensitive to perturbation in space and frequency. In this condition, a statistical characterization of the EM field is allowed via the theory of statistical ensembles. The situation is like that of a large-scale EM environment for EMC testing, e.g., the reverberation chamber (RC), which is known to sustain wave mixing and chaos due to the presence of a mechanical mode stirrer that break the room symmetry and changes the boundary conditions.
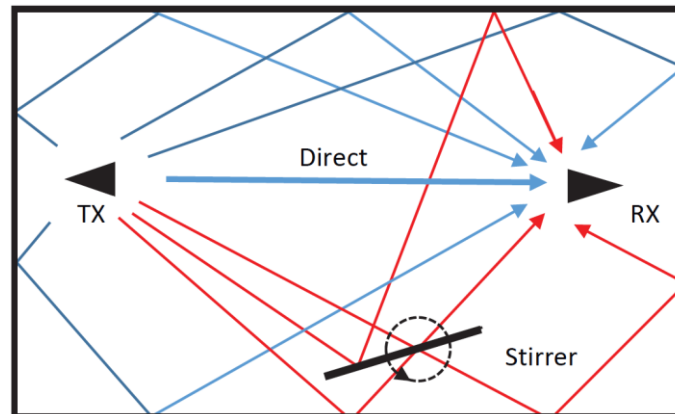
Figure 3-2 RIS-assisted MIMO Wireless Link operating in a closed environment (reproduced from [MBB20]).

Inherently, we will use the random coupling model (RCM) to model the channel response of the reverberation chamber for EMF enhancement metrics in WP6 and for performance assessment and testing in WP7 of the project. Figure 3-3 shows the CNIT-TI RC facility adopted for validation. While we defer an in-depth description of the CNIT-TI RC facility and the EMFEE measurement and validation procedure to future deliverables, here we assume that multi-path fading is driven by EM reverberation originating in confined propagation environments. Importantly, this will facilitate the WP6 activity as tuning RC losses mitigate the reverberation strength and retrieves average outdoor propagation conditions.
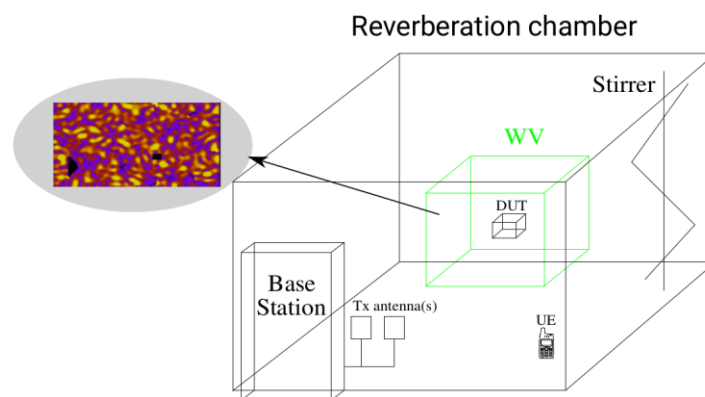
Figure 3-3 Reverberation chamber equipped by a LTE base station, MIMO transmitting antennas, and equipment under tests (reproduced from [MBB20]).

Furthermore, it becomes evident that wall installation of RISs inside an RC is particularly convenient, and technical procedures adopted for the operation of a Base Station in the CNIT-TI RC facility can be also used to control the RIS matrix of reflection coefficients remotely.

The RCM describes the behaviour of antenna arrays when they operate within a highly reflective, wave chaotic, EM environment. The statistical model develops the effect of multi-path fading in impedance matrices by first principles. Starting from Maxwell's equations, port voltages are defined as phasor coefficients of the tangential electric field expansion on basis modes. Port

currents are phasor coefficients of the surface current density expansion on conformal basis functions. The boundary-value problem is formed upon application of the Dirichlet/Neumann cavity boundary conditions. In free space, the boundary value problem is solved in terms of impedance matrix relating voltages and currents, whose element configures as a reaction integral. In interior boundary value problems involving cavities, the solution leads to an impedance matrix element that configures as a sum over discrete cavity eigenmodes. In compact form, the impedance matrix of a multiport antenna array or scatterer can be written as a distorted random matrix of the form

$$\mathcal{Z}^{env} = j\,\mathcal{X}^{rad} + [\mathcal{R}^{rad}]^{\frac{1}{2}}\;\xi\;[\mathcal{R}^{rad}]^{\frac{1}{2}} \tag{3.1}$$

where the free space impedance is given by $Z_{rad} = jX_{rad} + R_{rad}$, and the (normalized) cavity impedance is obtained as

$$\xi_{ps} = -\frac{j}{\pi}\sum_n \frac{w_{np}w_{ns}}{k^2 - k_0^2 - j\alpha} \tag{3.2}$$

with coupling coefficient w_{ns} given by zero mean unit width uncorrelated gaussian random variables. Note that the random impedance matrix shows the variate transformation that include the statistical (system independent) effect of environment backreaction (3.2) in the deterministic (system independent) free-space radiation of the antenna array. Environment walls are assumed to be perfect electrical conductors and losses are added perturbatively via the average loss factor α [GYX14]. The average loss factor has the physical meaning of an average number of eigenmodes overlapped at the operation frequency, and it is defined as

$$\alpha = \frac{k^2}{\Delta k^2 Q} \tag{3.3}$$

where Q is the average quality factor of the reflective cavity, or confined EM propagation environment, hosting the wireless transmission. Furthermore, the loss factor is related to the average coherence bandwidth of the EM environment

$$B_C = \frac{k^2}{\Delta k^2} \tag{3.4}$$

with Δk^2 average nearest-neighbour mean spacing between environment resonances. From (3.4) it is evident that the RCM predicts the NB fading occurring within the cavity bandwidth B_C. Since they represent statistical parameters that vary with the cavity/environment realization, both the quality factor and the coherence bandwidth are subject to fluctuations. For a perfect wave chaotic RC, the distribution functions of Q [AG12] and B_C [AG15] have been calculated and verified experimentally [AAS14] in the EMC community. However, their role in wireless device testing as well as wireless propagation channel emulation via RC over the last decade has been pointed out in [MBB20]. The loss factor of a specific EM environment can be estimated from scattering parameters, not necessarily measured through the antenna system adopted in the wireless communication link. Procedures to carry out such estimation are either based on

frequency-domain measurements [GDA16] or on time-domain measurements [ARA19]. Aperture losses can also be included in the RCM by either analytical [GAA15] or full wave [MPD20] computation of the aperture admittance.

In the previous section, we treated the RIS as an antenna array in passive mode. This implies that in an impedance model, we need to identify the RIS ports corresponding to unit cell terminals, which is the physical section marking the division between loading tunable circuitry and metasurface/RIS. It is worth noticing that depending on integration technologies, it could be challenging to de-embed the equivalent circuit impedance from planar structures. Here we keep this interpretation, and we consider the impairment of the three interaction paths, Tx-Rx, Tx-RIS, and RIS-Rx, due to multi-path fading within an indoor environment. It is worth remarking that, differently from a geometric approach that generates clusters of scatterers randomly, the RCM based approach considers the wave complexity driven by the reflecting boundary, and the moving objects are considered to contribute to field mixing creating statistically independent realizations of the same chaotic environment over time. The presence of objects adds to the absorption process, and this is accounted for by the environment quality factor. For every interaction path in the RIS assisted system, the environment realizations are captured by a statistical ensemble of path impedances (3.1) with same loss factor and different eigenmode coupling and eigenenergy in (3.2). Upon application of the RCM statistical prescriptions and focusing the analysis on SISO wireless links where Tx, Rx, and RIS are in far-field to each other, the end-to-end transfer function becomes a complex-valued random scalar of the form Section 2

$$\mathcal{H}_{E2E}^{env} \approx \mathcal{Y}_0 \left(\mathcal{Z}_{RT}^{env} + \mathcal{Z}_{RS}^{env} \, \Phi_{SS} \, \mathcal{Z}_{ST}^{env} \right) \tag{3.5}$$

Which gives the received signal y upon the transmitted signal x

$$y = \mathcal{H}_{E2E}^{env} \, x + n \tag{3.5a}$$

where the approximation symbol is due to the free-space mismatching $\mathcal{Y}_0$ and RIS state Φ_{SS} terms, and n is the Gaussian distributed electronic noise $n \sim \mathcal{N}(0, \sigma_n^2)$ at receiver. In the high loss regime, $\alpha > 1$, those terms are not affected by the multipath fading as they describe the unit-cell interactions on a small spatial scale compared to the dimensions of the confined EM environment. More in-depth work is ongoing, where statistical moments of the SNR are calculated assuming statistical uncorrelation between the random vectors $\mathcal{Z}_{RT}^{env}$, $\mathcal{Z}_{RS}^{env}$, and $\mathcal{Z}_{ST}^{env}$, defined by mutual impedances, viz.,

$$\begin{aligned}
\mathcal{Z}_{RT}^{env} &= [\mathcal{R}_{RR}^{env}]^{\frac{1}{2}} \; \xi_{RT} \; [\mathcal{R}_{TT}^{env}]^{\frac{1}{2}} \\
\mathcal{Z}_{RS}^{env} &= [\mathcal{R}_{RR}^{env}]^{\frac{1}{2}} \; \xi_{RS} \; [\mathcal{R}_{SS}^{env}]^{\frac{1}{2}} \\
\mathcal{Z}_{ST}^{env} &= [\mathcal{R}_{SS}^{env}]^{\frac{1}{2}} \; \xi_{ST} \; [\mathcal{R}_{TT}^{env}]^{\frac{1}{2}}
\end{aligned} \tag{3.6}$$

with multi-variate Gaussian distributed normalized impedances

$$\xi_{RT} \sim \mathcal{N}(0, \sigma_{RT}^2)$$
$$\xi_{RS} \sim \mathcal{N}(\mathbf{0}, R_{RS}) \qquad (3.7)$$
$$\xi_{ST} \sim \mathcal{N}(\mathbf{0}, R_{ST})$$

where no coherent part of the multi-path fading appear due to blockage (NLOS) of direct path and paths through the RIS. In (3.7), σ_{RT} is the standard deviation of the direct path, and R_{ST} and R_{RS} are the correlation matrices that capture the spatially correlated fading within the interaction paths through the RIS from transmitter and to receiver respectively. The multi-variate Gaussian model implies the presence of obstructions, hence the NLOS condition between Tx and RX and between RIS and Tx/Rx. This situation can be created in a controlled way in RC facilities. Given the definition of the random signal-to-noise-ratio in presence of receiver noise,

$$SNR = \frac{|\mathcal{H}_{E2E}^{env}|^2}{\sigma_n^2} \qquad (3.8)$$

the expectation value over correlated multi-path fading realizations is found to be

$$\mathrm{E}[SNR] = \mathrm{Tr}[\widehat{\Phi}] + \sigma_{RT}^2 \qquad (3.9)$$

while the variance over correlated multi-path fading realizations is found to be

$$\mathrm{Var}[SNR] = 2\,\mathrm{Tr}[\widehat{\Phi}^2] + \left(\mathrm{Tr}[\widehat{\Phi}]\right)^2 + 2\sigma_{RT}^2\mathrm{Tr}[\widehat{\Phi}] + \sigma_{RT}^4 \qquad (3.10)$$

with $\widehat{\Phi} = \sigma_n^{-2} R_{ST}\Phi^{\dagger}R_{RS}\Phi$. The moment generating function (MGF) of the SNR has been derived, whence expectation and variance are computed by derivative of the MGF for the LOS case. Since the final expressions obtained in closed mathematical form are lengthy and involved, only the special cases (3.9) and (3.10) have been reported for the sake of brevity. In the complete theory, the LOS condition for the three interaction paths have been also considered.

Figure 3-4 shows the comparison between SNR obtained by using the optimization procedure in [XD21] and the non-optimized case with $\Phi = a\mathrm{I}$ and $\mathrm{R} = \mathrm{I}$.
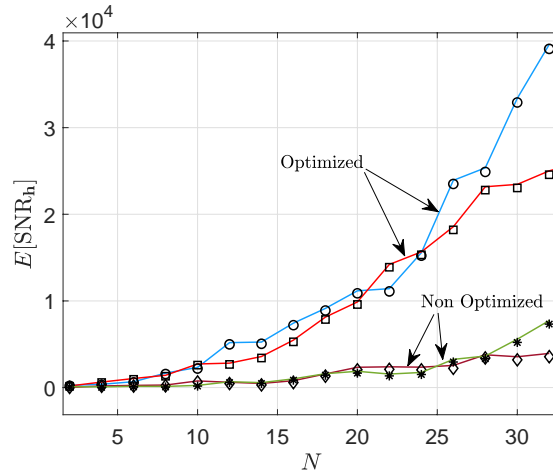
Figure 3-4 RIS-assisted SISO Wireless Link operating in a closed environment.

A random E2E MIMO communication model based on impedance can be easily obtained from the form [ADD21].

The model presented in this section can be used to derive the metrics statistics associated with the KPI evaluation. A first step towards this goal is to derive the distribution of the ergodic channel capacity of RIS-assisted SISO systems $\chi = \log_2(1 + \rho |\mathcal{H}_{E2E}^{env}|^2)$, which is computed for selected values of ρ. Closed form mathematical expressions for the channel capacity have been derived.

3.2 RIS link with random (and moving) scatterers

To investigate the impact of scatterers to the communication, the impedance-based model presented in section 2.4 has been extended. The model is based on the thin wire dipole system, with an inclusion of random dipole-like scatterers. As a reference, the power of the communication channel in the absence of RIS and scatterers for a SISO system separated by $9\lambda_0$, see Figure 3-5 vis $\left|\underline{\mathcal{H}_{E2E}}\right| = 0.0062$. More specifically, the communication transfer function based on the impedance model [GD21] is used throughout this section.
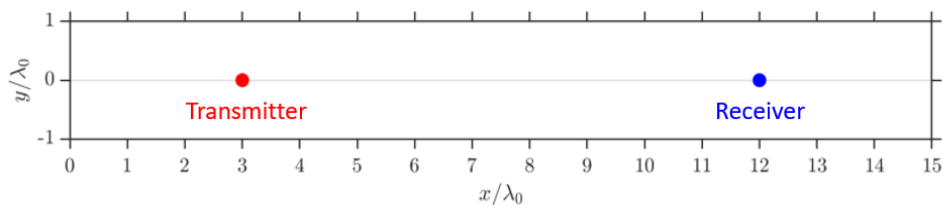
Figure 3-5 SISO communication reference configuration

Another benchmark case shown in Figure 3-6, where there is no scatterers but in the presence of RIS. In this case there are 50 half-wavelength dipoles centred at $x = 7.5\lambda_0$ with inter-separation distance of $0.25\lambda_0$.
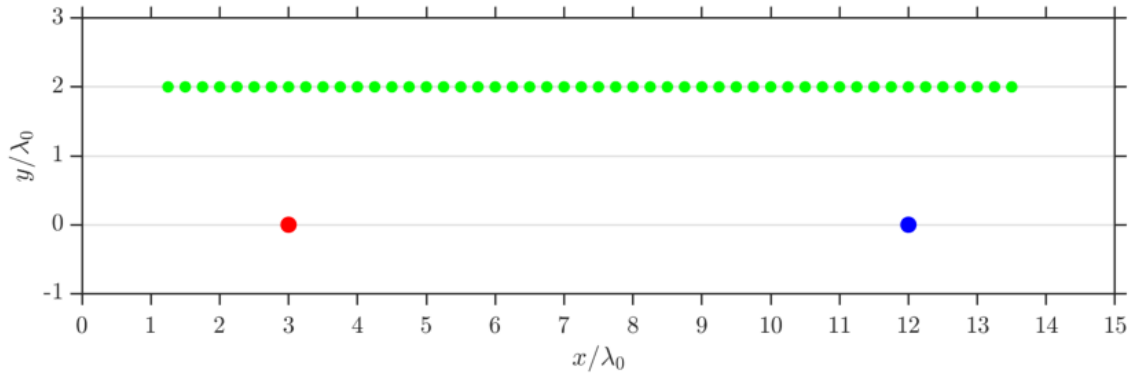
Figure 3-6 SISO communication reference configuration in the presence of RIS

The termination of the RIS is now obtained via Genetic Algorithm (GA) optimisation, whereby the GA is task to find $\boldsymbol{Z}_{\mathrm{RIS}}$ for maximum communication gain $\left|\underline{\underline{\mathcal{H}}}_{E2E}\right|$. Please note that as GA is a stochastic optimisation, the optimised parameter may be of the local optimum not global. Using this termination and in the absence of scatterers, the channel gain is found to be $\left|\underline{\underline{\mathcal{H}}}_{E2E}\right| = 0.0108$.
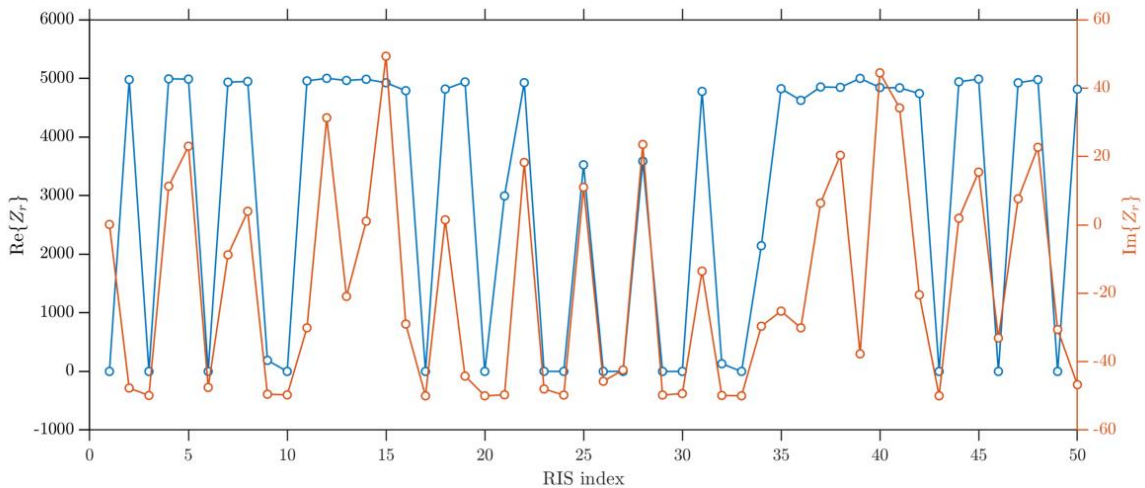
Figure 3-7 RIS impedance termination obtained via Genetic Algorithm for the specific configuration of Fig. 3-6.

Subsequently, using the GA obtained RIS termination impedance Monte-carlo simulations is performed to evaluate the impact of randomly position scatterers. Note that during the Monte

Carlo simulation the RIS termination impedance is fixed, i.e., statically terminated RIS, this is due to the expensive computation cost if GA is performed for each Monte Carlo realisation. Efficient optimisation protocol which will be developed in order to allow a fast dynamic RIS system.
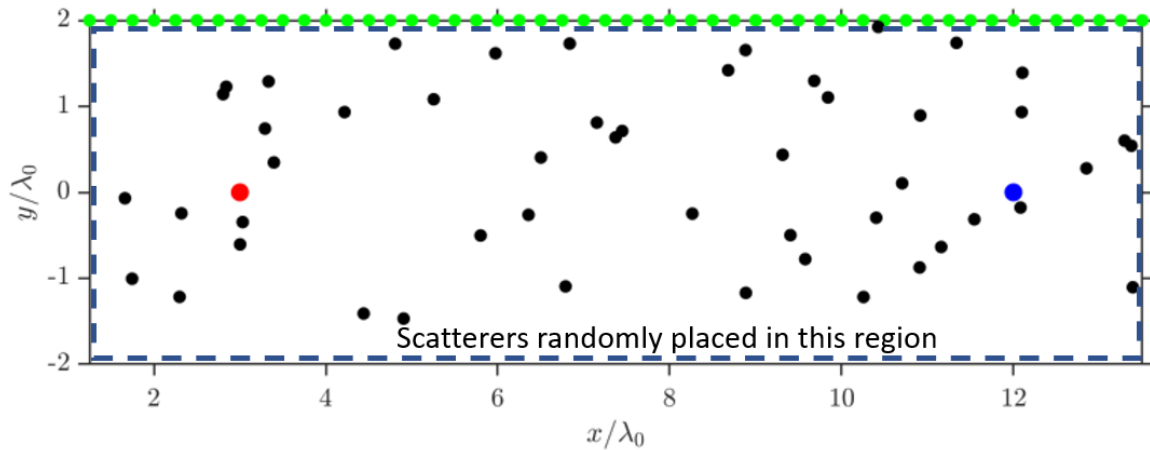
Figure 3-8 Monte-carlo simulation of the SISO communication in the presence of randomly positioned scatterers.

The Probability Densities Function (PDF) of the channel gain $\left|\underline{\mathcal{H}}_{E2E}\right|$ are shown in Figure 3-9.

These PDF are obtained for different number of scatterers, with or without RIS. The dashed lines denote the channel gain in the absence of scatterers, i.e., 0.0062 and 0.0108. For a small number of scatterers, the RIS improve the robustness of the communication channel. While the effectiveness of RIS reduces in the presence of the scatterers, there is higher probability of obtaining high channel gain in the presence of RIS than in the absence of RIS. Again, note that this is static RIS, we believe that dynamically tuneable RIS will significantly improve the performance of the communication.
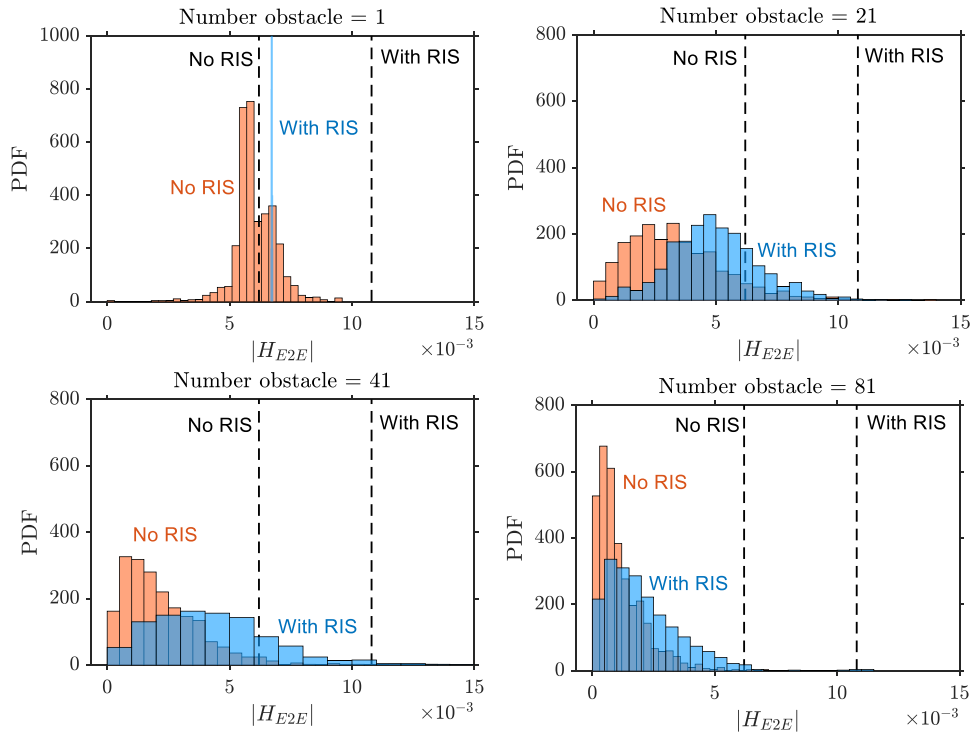
Figure 3-9 PDF of the channel gain $\left|\underline{\underline{\mathcal{H}}}_{E2E}\right|$.

3.3 RIS scattered field approximation

The incorporation of EM RIS response within coverage planning tools is grounded on the fundamental development of a high frequency asymptotic approximation of the RIS scattered field upon oblique incidence of plane waves. We start from considering a transmitter that is far away from a RIS and a receiver that is in the far field of the RIS and does not have direct LOS with the transmitter. The transmitter radiates a uniform TE plane wave that impinges onto a pixelated reflective surface

$$\mathbf{E}^i = \left(\hat{\mathbf{y}}\cos\theta^i + \hat{\mathbf{z}}\sin\theta^i\right) e^{-jk\left(y\sin\theta^i - z\cos\theta^i\right)}$$
$$\mathbf{H}^i = \hat{\mathbf{x}}\,\frac{1}{\eta}\,e^{-jk\left(y\sin\theta^i - z\cos\theta^i\right)} \tag{3.11}$$

where η is the free space wave impedance, k is the wavenumber, and θ^i the incidence angle
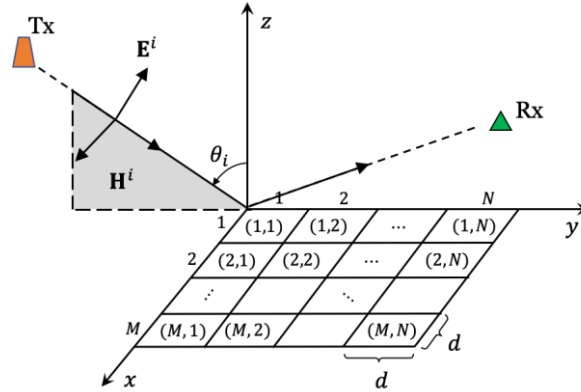
Figure 3-10 TE-polarized plane wave incident on the RIS.

The plane wave induces an equivalent surface current density on the metasurface, which reads

$$\mathbf{J}^s = \hat{\mathbf{y}} \frac{2}{\eta} r(m,n) e^{-jky\sin\theta^i} \tag{3.12}$$

if each pixel has a unit magnitude reflection coefficient $r(m,n) = e^{j\psi(m,n)}$ with $\psi(m,n) \in [0,\pi]$ in a binary RIS. The calculation of the vector potential yields the RIS scattered field in the far field:

$$\begin{aligned}
\mathbf{E}_\theta^s &= \mathcal{C}(r)\,\mathcal{E}_\theta^s(\theta^s,\varphi^s,\theta^i)\,\mathcal{A}^s(\theta^s,\varphi^s,\theta^i) \\
\mathbf{E}_\varphi^s &= \mathcal{C}(r)\,\mathcal{E}_\varphi^s(\theta^s,\varphi^s,\theta^i)\,\mathcal{A}^s(\theta^s,\varphi^s,\theta^i)
\end{aligned} \tag{3.13}$$

where $\mathcal{C}(r) = -j\,\frac{kd^2}{2\pi}\frac{e^{-jkr}}{r}$, the element radiation pattern is defined as

$$\begin{aligned}
\mathcal{E}_\theta^s(\theta^s,\varphi^s,\theta^i) &= \cos\theta^s \sin\varphi^s \operatorname{sinc}X \operatorname{sinc}Y \\
\mathcal{E}_\varphi^s(\theta^s,\varphi^s,\theta^i) &= \cos\varphi^s \operatorname{sinc}X \operatorname{sinc}Y
\end{aligned} \tag{3.14}$$

and the RIS array factor is defined as

$$\mathcal{A}^s(\theta^s,\varphi^s) = \sum_{m=1}^{M}\sum_{n=1}^{N} e^{j\psi(m,n)} e^{jk_x md} e^{jk_y nd} \tag{3.15}$$

with

$$k_x = k \sin \theta^s \cos \varphi^s$$
$$k_y = k(\sin \theta^s \sin \varphi^s - \sin \theta^s)$$
$$X = \frac{kd}{2} \sin \theta^s \cos \varphi^s$$
$$Y = \frac{kd}{2}(\sin \theta^s \sin \varphi^s - \sin \theta^s)$$

As part of the RISE-6G effort, the field (3.13) has been used in [PRL21] to optimize the radar cross section (RCS) of binary and quaternary RISs via statistical mechanics tools. More precisely, the RCS has been recast into an Ising Hamiltonian where the reflection phases play the role of spin degrees of freedom. Since optimizing a large RIS require exploring a large parameter space, we have proposed method based on quantum annealing to find the optimal operational state of the RIS for both focusing and suppression of electromagnetic radiation in free-space.

In order to support the performance analysis of multi-user communication of interest in WP6, simultaneous energy focusing on a prescribed user while suppressing towards an unintended user has been demonstrated using the quantum annealing (QA) to design the optimal RIS state. This is shown in Figure 3-11

(a)   (b)
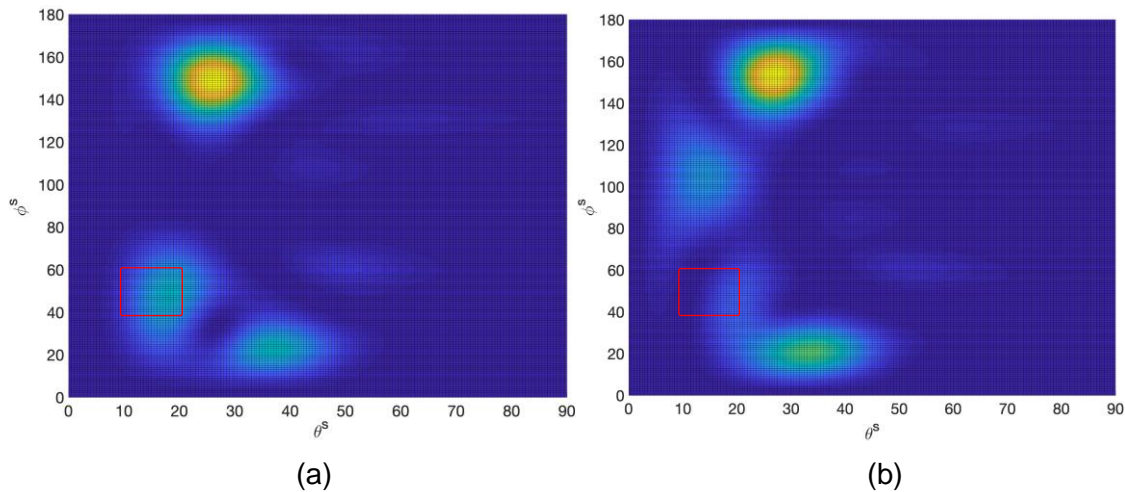
Figure 3-11 Simultaneous focusing and suppression

Creating arbitrary phase shifts of the local reflected wave can be achieved with low profile structures with subwavelength metallic texture on a grounded substrate, as shown in Figure 3-12. There, a single pixel is composed of 7x7 metallic patches with $h < p < a \ll \lambda$. Variation of p and a results in a continuous phase shift of the impinging wave provided $d \sim \lambda$.
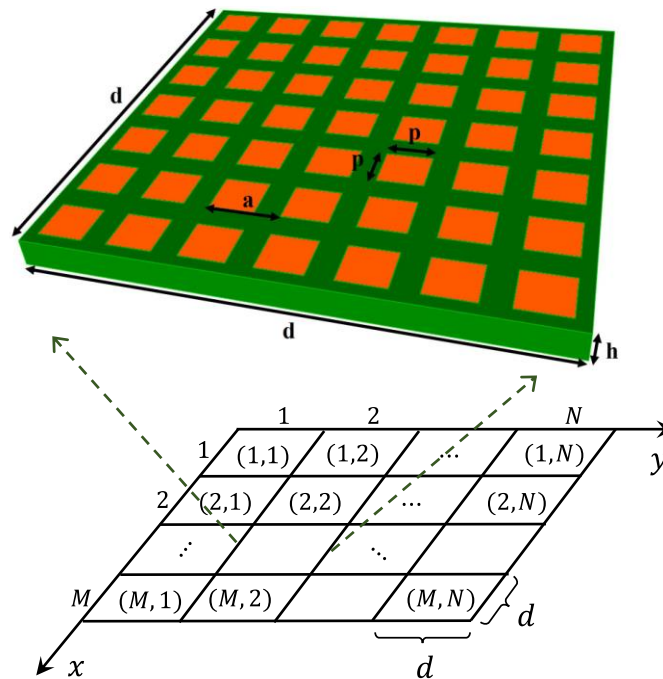
Figure 3-12 Metasurface structure and subwavelength ($h < p < a \ll \lambda$) textured pixel realization.

The QA optimization has been extended to a quaternary RIS: An anomalous reflector at $\theta^s = 20$ degrees and $\varphi^s = 20$ degrees has been demonstrated, which results in the phase shift mask here below.
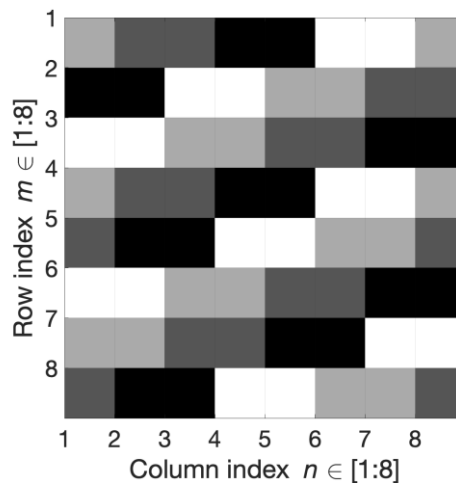
Figure 3-13 Reflection phase mask for the optimized 8x8 metasurface structure

The optimised RCS in Figure 3-14(a) shows a focusing spot with very low side lobes at specular and other spurious directions. The RCS predicted by the physical optics model in Figure 3-14 (a) has been verified by full wave boundary element simulations reported in Figure 3-14 (b).

(a)   **(b)**
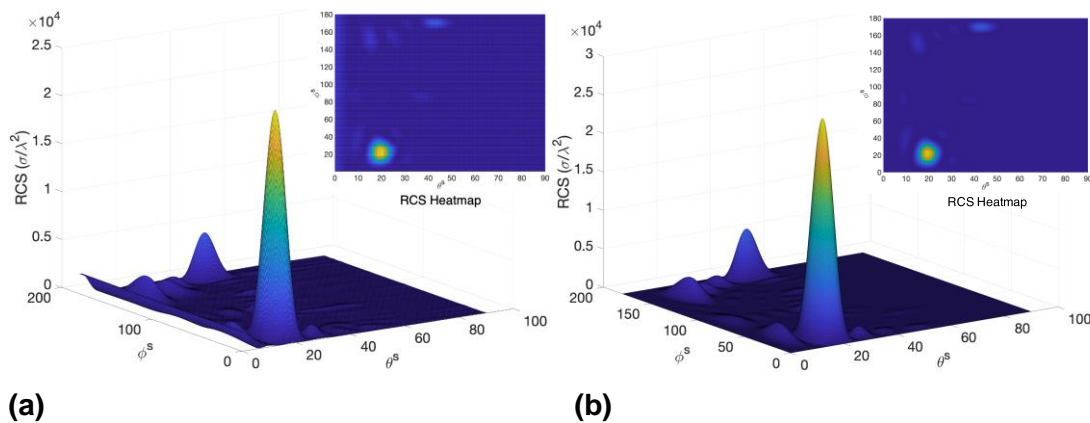
Figure 3-14 Comparison between geometrical optics and full wave computation

Further work is ongoing to apply the QA optimization methodology to the impedance-based MIMO model, which will be described within the next reporting period.

3.4 Deterministic RIS channel modelling by RT-DEA

The physical optics model, derived for both the TE and the TM polarizations of the EM field scattered by the RIS, constitutes the starting point for the integration of the RIS response in ray tracing (RT) algorithms. In RISE-6G, we will use the dynamical energy analysis (DEA) method: an RT scheme based on energy flow equations that are computed on discrete meshes. Differently from conventional shoot and bounce RT methods, DEA is based on phase-space (joint spatial angular domain) representation of waves, and it propagates densities of rays through the numerical space by iterative application of a compact operator derived from the boundary integral equation of the confined space. It has been shown already in viboacoustics that DEA is able to compute the energy flow in refined FEM meshes [HGG16], also mitigating numerical dispersion via directional basis functions [CCR21]. Furthermore, the ability of DEA of capturing statistical inhomogeneity and anisotropy within complex multi-connected environments with high losses has been showed recently via comparison with power balance methods [FBP21].

In RISE-6G we have undertaken two lines of research to achieve a flexible and efficient coverage planning tool for multi RIS mobile networks beyond 5G:

1. Representation of the RIS scattered field in phase-space. This starts from the calculation of the Wigner function and produces the ray based, classical scattering function by frequency averaging. Upon incidence of a partially coherent field impinging onto the RIS, the spatial field-field correlation of the scattered field can be readily derived from the physical optics model of Sec. 3.3.

2. Generation of numerical meshes from CAD models. In order to enable the DEA compliant numerical domain construction of the two field trials offered by the Partners CRF and SNCF, it is necessary to convert the CAD models typically used to model 3D environments, like Autodesk AutoCAD (.dwg files) and Autodesk Revit (.rvt files), into appropriate numerical 3D meshes based on tetrahedral elements. A diagram summarising the conversion procedure for generating DEA compliant meshes starting from AutoCAD and Revit CAD models is shown in Figure 3-15
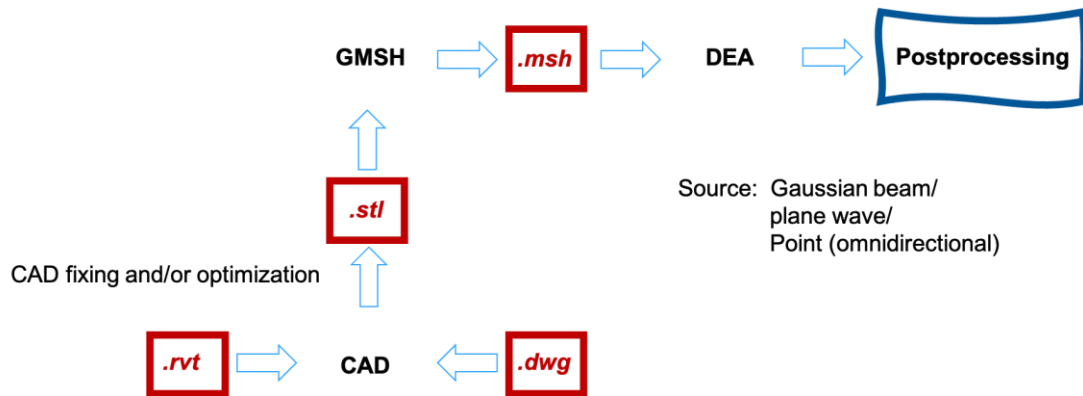
Figure 3-15 Procedure to generate DEA-compliant meshes from CAD models

The first step is then to generate an .stl file from models in Autocad or Revit format. This procedure can be performed directly by exporting the source files in.stl format from these CAD tools. An optimisation step may be necessary, for example to export only a portion of the model of interest, such as a single room within a large building. This output .stl file describes only the surface geometry of the three-dimensional objects without any representation of color, texture or other common CAD model attributes.

To illustrate this initial conversion, Figure 3-16 shows the 3D CAD model of the CRF Smart Factory on the left and the equivalent conversion in. stl format on the right. It is already interesting to note that not only the volume contained in the walls, roof and perimeter elements of the entire structure should be meshed, but also the volume of air contained within the various rooms.
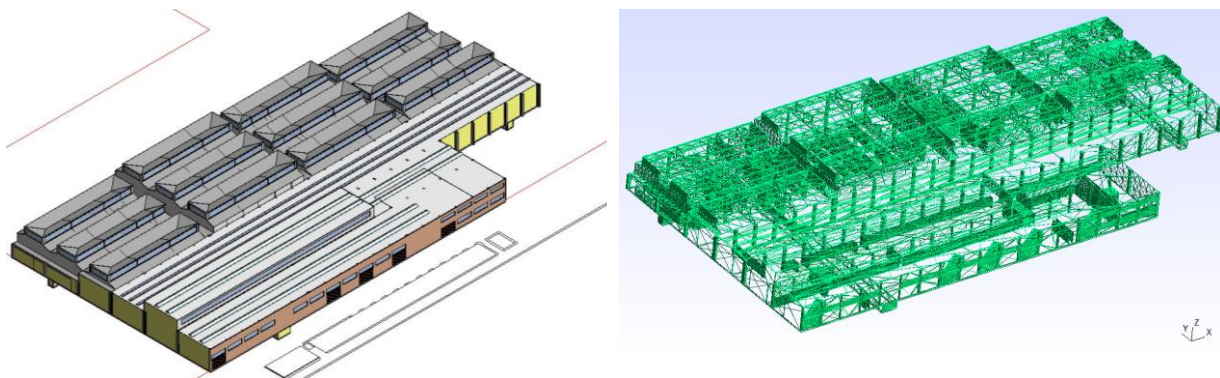
Figure 3-16 CAD Model of the CRF Smart factory: Autodesk Revit .rvt file on the left and the file converted in .stl format on the right.

The next conversion step is to process the file in .stl format with Gmsh, an open source 3D finite element mesh generator with a built-in CAD engine, to generate a numerical tetrahedral mesh fully compliant with DEA.

To simply illustrate what mentioned above, in Figure 3-17 is shown the conversion of a simple canonical surface like a sphere with Gmsh software. In Figure 3-17 (a) is reported the .stl file

corresponding to the only surface of the sphere, while in Figure 3-17 (b) is shown the 3D tetrahedral mesh of the sphere, or the output file produced by Gmsh.

Starting from this surface, it is then possible to create a volume within that surface and apply the desired tetrahedral 3D mesh, specifying the global mesh size factor. Once the 3D mesh has been created, it is also possible to assign a certain material to a certain sub-portion of the volumetric mesh considering the correct electromagnetic parameters to properly inform DEA.

(a)   (b)
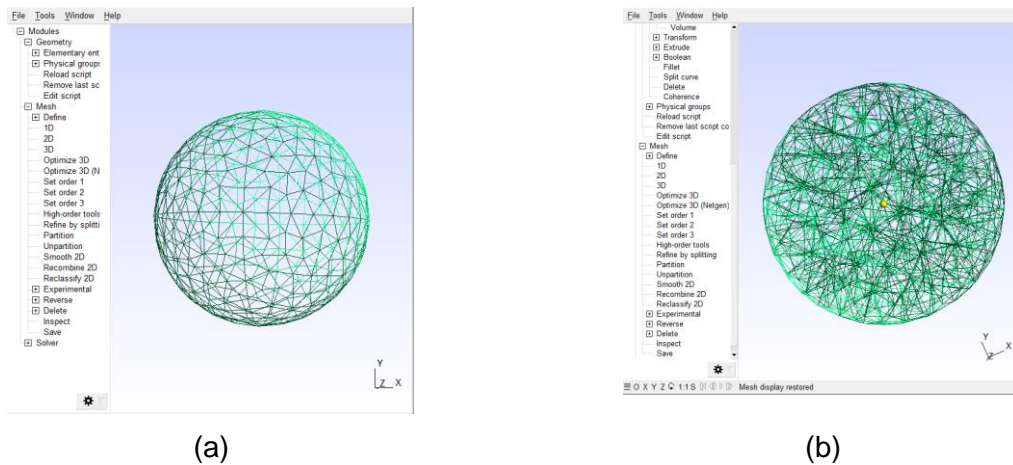
Figure 3-17(a) File .stl representing the surface of a sphere, (b) 3D tetrahedral mesh of the sphere generated with Gmsh software.

The current work therefore involves the automatic generation of a fully DEA-compatible 3D mesh from complex structures such as CRF's Smart Fab already shown.

Ultimately, the activities 1. and 2. will coalesce in the RIS-assisted channel design and characterization of the smart factory (CRF) and train station (SNCF) environments.

3.5   Effective roughness scatterer model for RIS

In this paragraph we introduce an approach for modelling the scattering from a general finite-size and non-ideal RIS. The model is conceived for being integrated into currently available ray- based models, such as ray tracing and ray launching methods, which are recognized as the most suitable and efficient deterministic models for realistic radio propagation simulations in man-made environments. Several ray-based models discretize ordinary surfaces into surface elements (also called "tiles") in order to simulate diffuse scattering (by using, e.g., the effective roughness (ER) model [DFV+07]) and/or to achieve a good computational efficiency through parallel computing algorithms [LU19]. In the present work, we leverage the tile-based approach to simulate the anomalous scattering from an RIS (also referred to as anomalous reflection or re-radiation in the sequel), by using a method based on Huygens' principle. The proposed methodology for modelling an RIS within a ray-based propagation simulator is sketched Figure 3-18.
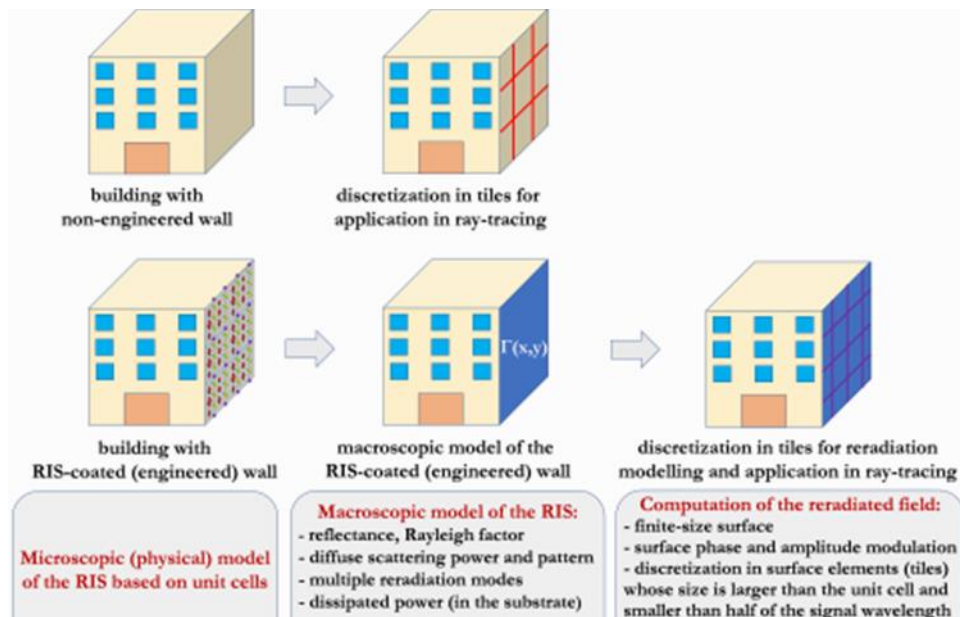
Figure 3-18 Comparison between non-engineered walls and RIS-coated walls: Proposed methodology and integration in ray-based models [VVD+22].

While ordinary surfaces are simply discretized to apply efficient ray-based models, RIS-coated surfaces are first homogenized and described through a proper spatial modulation function r(x, y), which accounts for anomalous reradiation, and are then discretized to apply computation procedures similar to those utilized for ordinary surfaces. The scattering from an RIS surface is therefore decomposed into "typical" scattering effects, such as specular reflection, diffraction, diffuse scattering, and anomalous reradiation. While the former effects are treated by using well-established theories and methods, such as geometrical optics, the uniform theory of diffraction, and the ER model, the anomalous reradiation is treated by using the Huygens-principle approach, by integrating it into currently available frameworks for the discretization of surfaces and for parallel computation. The key feature of the proposed model is satisfaction of the power balance between the different scattering modes, which is enforced by using a parameter-based approach. Summarizing, the model is based on two steps: i) the definition of the global power balance between conventional and anomalous scattering modes, and ii) the computation of the scattered field as a coherent sum of multiple contributions, including conventional and anomalous reradiated modes.

We introduced a general parametric approach for modelling scattering from a finite-size RIS, which is suitable for integration into ray-based models. The proposed model is macroscopic, as it is agnostic to the specific microscopic (unit cells) physical implementation of the RIS, which is instead characterized by macroscopic parameters. The model explicitly takes into account diffuse scattering, in addition to the desired and undesired reradiation modes, it is not limited to flat metasurfaces, and it can be easily generalized for application to refractive metasurfaces (not considered here for brevity).

The method is conceived to be integrated into advanced discrete ray-based models [Lu07], and it can be efficiently implemented on parallel computing platforms.

The model is tested and validated against results available in the literature, which are based on theory, full-wave simulations, and measurements conducted on manufactured RISs. The results

confirm the generality and accuracy of the proposed approach, as well as the non-negligible impact that multi-mode reradiation and diffuse scattering may have on the total scattered field and, notably, on the far-field radiation pattern of a finite-size RIS.

Ideal Phase-Gradient Reflector: The first case study corresponds to an ideal metasurface that introduces ideal phase shifts to the reflected fields, with the goal to reradiate a single incident plane wave towards a target direction in the absence of dissipation and undesired reradiated modes. We consider a $7 \times 7 \ m^2$ large RIS that lies in the *xy* plane and introduces a linear phase modulation such that $d_{\chi m}(x')/dx' = k(sin\theta_i - sin\theta_r)$, where θ_i is the angle of incidence and θ_r is the desired angle of reflection. Being an ideal case, we assume for the other parameters in (12): $m = 1, R = 1, A_m(x', y') = 1$.

The RIS operates at 3 GHz and is illuminated normally ($\theta_i = 0$) by a plane wave that is linearly polarized in the *y*-direction and whose intensity is 1 V/m. The desired angle of reradiation is $\theta_r = 60$ degrees. The reradiated field is computed with the integral model iis reported in Figure 3-19. The locations illustrated lie in the radiative near-field region of the RIS, since the Fraunhofer far-field distance is approximately equal to 1000 m for the considered setup. We observe that the electric field is steered towards the desired angle of reflection. As expected, in addition, we observe edge- diffraction fringes that are due to the finite size of the RIS.
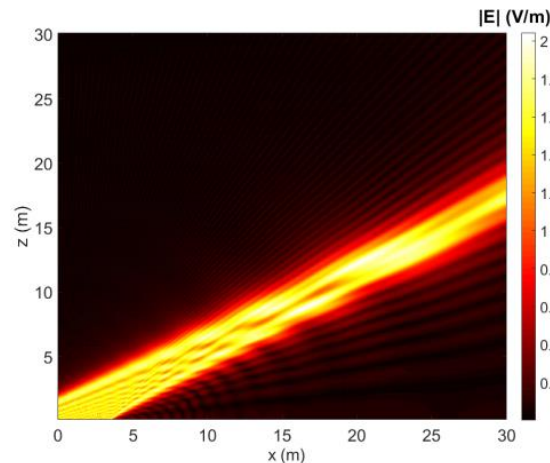
Figure 3-19 Reradiated field [V/m] in the xz plane from a $7 \times 7 \ m^2$ RIS that is located in the xy plane and is centered at the origin. Setup: 3 GHz operating frequency, normal incidence, reflection towards the angle of 60 degrees [VVD+22].

For comparison, we compute the reradiated electric field by using the antenna-array mode. The comparison shows that the relative error is less than $1 - 2\%$ for most of the observation points.
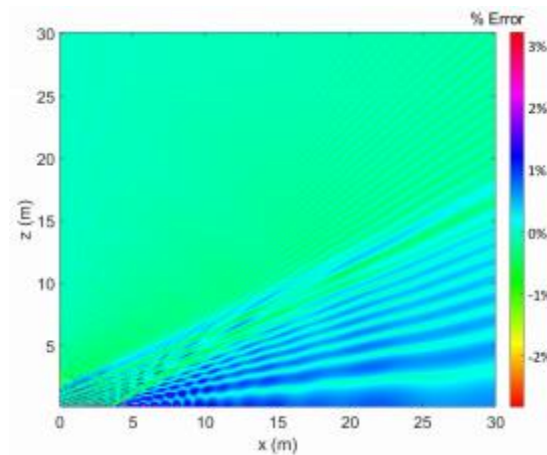
Figure 3-20 Relative error (in percentage) of the antenna-array model with respect to the integral formulation [VVD+22].

.

Lossless Anomalous Reflector (with parasitic modes)

To evaluate the capabilities of the proposed model to account for the presence of parasitic reradiated modes, we consider the metasurface analyzed in [DT21, Fig. 9]. This case study corresponds to a phase-gradient RIS that is lossless, periodic, and is optimized based on the locally periodical approximation. In [DT21], the metasurface is characterized with the aid of electromagnetic simulations and on an approximate analytical framework based on Floquet's theory. In this example, the RIS is illuminated by a normally incident plane wave at 3 GHz. The modulation period of the metasurface is $D = 0.1064$ m and the size of the RIS is $10D \times 10D$. The reradiated field is evaluated at a distance equal to 22.64 m, which is close to the Fraunhofer far-field boundary. The reradiation pattern is illustrated in Figure 3-21 (a) and is obtained by using the antenna- array formulation in the absence of losses and diffuse scattering, as in [DT21]. The reradiated field is computed by taking into account two anomalous reradiated modes that are combined with specular reflection and diffraction. Specifically, specular reflection and diffraction are obtained with state-of-the-art ray- based methods. Specular reflection, anomalous reradiation, and diffraction are appropriately weighted according to the power- balance principle

Diffuse Scattering

This case study is on the impact of diffuse scattering that originates from design trade-ofs, construction non-idealities and/or the deposit of dust on the surface of the RIS. To the best of our knowledge, no specific experimental results on modelling diffuse scattering from engineered surfaces exist in the literature. Thus, we con- duct a parametric study, in order to assess the potential impact of diffuse scattering on the radiation pattern of an RIS. The numerical results are shown in Figure 3-21 (b) for different values of the scattering parameter S in (11). The metasuface considered is the lossless anomalous reflector analyzed above. In Figure 3-21 (b), we study the impact of diffuse scattering under the assumption that 40% ($S^2 = 0.4$) or 80% ($S^2 = 0.8$) of the incident power is diverted into Lambertian diffuse scattering according to the power-balance constraint in (11). Although the considered values for S may be overestimated, we chose them to make the curves more readable. This shows the important role that diffuse scattering can play in RIS-aided.
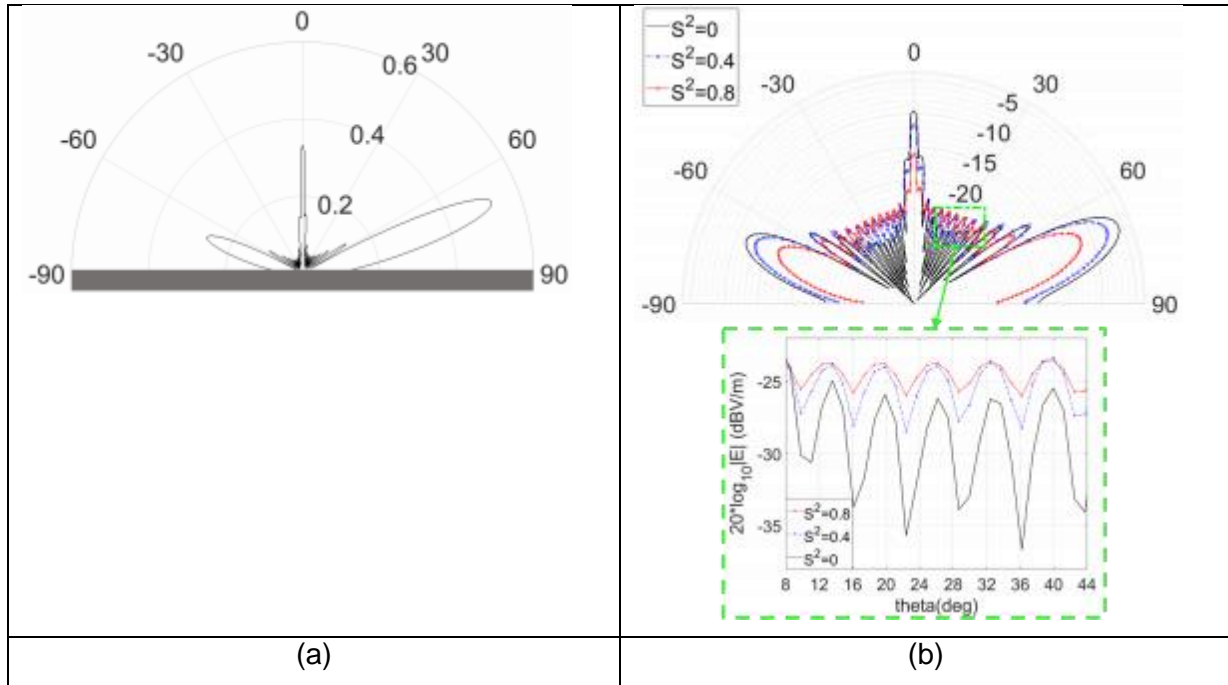
Figure 3-21 (a) Radiation pattern of the lossless anomalous reflector in [20]. Setup: normal incidence and the desired angle of reflection is 70 degrees. (b) Far-field (dBV/m) scattering pattern of the lossless anomalous reflector considered in [20] in the absence of difuse scattering (reference black curve), and in the presence of 40% (blue curve) and 80% (red curve) of the incident power diverted into diffuse scattering [VVD+22].

3.6 RIS enabled channel sounding and modelling

In this section we describe the channel sounding and characterization activities enabled by RIS.

In particular we first show a channel measurement campaign employing a T-RIS by CEA. Then the preliminary results of a joint CEA-GNW measurement campaign are shown.

3.6.1 T-RIS enabled channel sounding

In this section we describe two indoor channel measurement campaigns performed by employing a T-RIS (Figure 3-22 (a)) or a Virtual Cubic Array VCA antenna (Figure 3-22 (b)).

(a) T-RIS   (b) Omnidirectional VCA
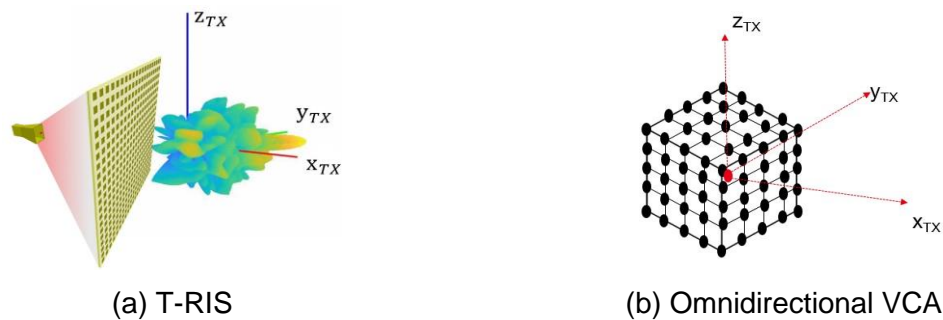
Figure 3-22 T-RIS based antenna (a) and VCA (b) schemas.

The channel measurements were conducted in a laboratory room. The dimensions of the room were 12 m × 6 m . The laboratory room is furnished with tables, chairs, desktops, sofas, and a television as depicted in the Figure 3-23(a)-(b). The left wall of the room comprises mostly of glass windows and the right side wall also has a part with a glass window. On the roof, there is also a metallic positioner. The measurement setup is based on a Vector Network Analyzer (VNA) operating in the 26-30 GHz frequency range. The receive side (RX) and the transmit side (TX).

(a)   (b)
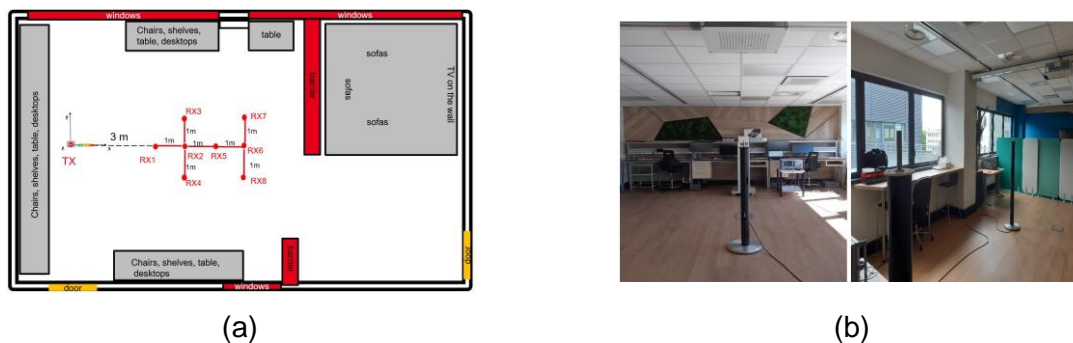
Figure 3-23 Indoor channel measurement campaign : measurement floor plan (a) and environment (b).

The antenna were both at a height of 1.52 m above the ground. While on the RX side a wideband monopole (around 0 dBi gain) antenna was employed in both setups, two different strategies were implemented on the TX.

The T-RIS based measurement setup (Figure 3-22 (a)) is based on 20 × 20 surface elements implementing a circularly polarized transmitarray [9], [10], presenting 18.7 dBic in the main

steering direction, $\phi_s = 0°$, while at maximum steering angle investigated, i.e. $\phi_s = \pm60°$ the gain drops to 11.94 dBic, because of the array factor effect. In this measurement campaign for each RX position, different phase distribution on the 400 unit cells are implemented to scan the environment and vary the main steering direction ϕ_s, from -60° to 60° by step of 5°. In the VCA setup, a wideband monopole antenna placed on a X-Y-Z scanner performs a 5 × 5 × 5 spatial grid of a half-wavelength grid step, i.e. 5 mm (Figure 3-22 (b)).

Multipath estimation and T-RIS embedded

Starting from the VCA channel measurements, the UWB SAGE algorithm was used for the MPCs detection and channel parameters estimations. Only MPCs of significant power were considered in this work (10 dB above the noise floor). The maximum number of resolvable MPCs to be estimated was set to 100. The stopping criteria was when more than 95 percent of the measured channel power had been estimated, or otherwise, when the maximum number of the resolvable MPCs had been reached. Fig. 3 shows the azimuth angle of departure (AoD) and elevation angle of departure (EoD) polar plots for the receiver position RX5: each circle on the figures represents a detected MPC, whose colour is the power and the radial distance is the travelled distance in meters.
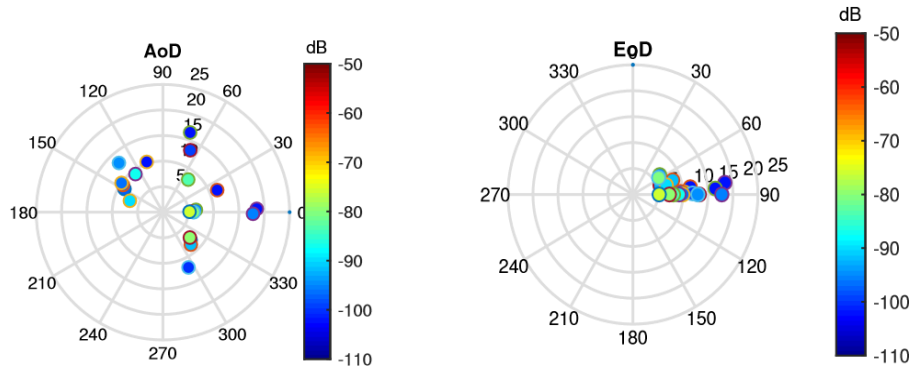
Figure 3-24 Power Angular Delay Profile (PADP) extracted from VCA measurements in the azimuth plane (left) and elevation plane (right) for receiver position RX5.

Let us consider the angular dependent channel impulse response extracted from VCA measurements as:

$$h(\tau, \Omega_{AoD}, \Omega_{AoA}) = \sum_{l=1}^{L} \alpha_l \cdot \delta(\tau - \tau_l) \cdot \delta(\Omega_{AoD} - \Omega_{AoD,l}) \cdot \delta(\Omega_{AoA} - \Omega_{AoA,l}) \quad (3.16)$$

where the *l*-th MPC is characterized by its amplitude (α_l), delay (τ_l), angle of departure $\Omega_{AoD,l}$ and angle of arrival $\Omega_{AoA,l}$. Starting from this estimation, the objective is to embed T-RIS effect on the channel and compare it with the real measured one with the T-RIS.

The T-RIS vector transfer function can be written as:

$$\mathbf{H}(f, \theta, \phi, \theta_s, \phi_s) = \sum_{m} \frac{\lambda}{4\pi r_m} e^{-j\frac{2\pi}{\lambda}r_m} \mathbf{H}_{FS}(\theta_{FS}^m, \phi_{FS}^m) \cdot \mathbf{H}_{RX,m}(\theta_{uc}^m, \phi_{uc}^m) \cdot S_{21}^m(f) \cdot \mathbf{H}_{TX,m}(\theta_{uc}^m, \phi_{uc}^m)$$

$$(3.17)$$

where $\mathbf{H}_{FS}(\theta_{FS,}^m, \phi_{FS,}^m)$ is the radiation pattern of the source illuminating the surface, $\mathbf{H}_{RX,m}(\theta_{uc}^m, \phi_{uc}^m), \mathbf{H}_{TX,m}(\theta_{uc,}^m \phi_{uc}^m)$ respectively represent the radiation patterns of the *m*-th unitcell in the receiving side and of the *m*-th unit-cell in the transmitting side. r_m represents the distance between the source and the *m*-th unit-cell. Each unit cell will present a transmission coefficient $S_{21}^m(f)$, whose phase is controlled by a 1-bit PIN diode architecture, implementing either a $0°$ or $180°$ variation. *f* is the frequency index, θ, ϕ are the pattern elevation and azimuthal angles respectively. Finally θ_s, ϕ_s are the elevation and azimuthal steering angles, obtained thanks to the phase distribution over the unit-cells.

Hence for a given phase distribution on the T-RIS, i.e. for an aimed steering angle (θ_s, ϕ_s), we can embed its effect on the channel by replacing in Eq. (1) the *l*-th MPC amplitude with:

$$\alpha_l^{emb} = \alpha_l \cdot H(f, \theta = \theta_{AoD,l}, \phi = \phi_{AoD,l}, \theta_s, \phi_s) \qquad (3.18)$$

where $\mathbf{H}(f, \theta = \theta_{AoD,l}, \phi = \phi_{AoD,l}, \theta_s, \phi_s)$ is the transfer function of the T-RIS from Eq. (2) in the given angle of departure $\Omega_{AoD,l} = (\theta_{AoD,l}, \phi_{AoD,l})$, neglecting here the polarization for simplicity of notation. In practice, given that we used on RX side a vertically polarized antenna, we consider in the following analysis the embedding with only the main polarization (given the small effect from the cross-polarised contribution).

Measured Channel vs Synthesized Channels

In this section, we will discuss the main results obtained. For the receiver positions RX1, RX2, RX5 and RX6, the steering angle $\phi_{s,max}$, corresponding to the main lobe direction where the maximum power is received, is $\phi_{s,max} = 0°$, while for the receiver positions RX3, RX4, RX7 and RX8, the main beams are in the steering directions $\phi_{s,max} = 15°, -15°, 10°$, and $-10°$ respectively.

The T-RIS was found to decrease both the path loss and delay spread (DS) for all receiver positions in the main lobe direction. As an example we consider here RX5 position. Figure 3-25 shows the UWB-SAGE estimated MPCs, i.e. the Power Angular Delay Profile (PADP) with omnidirectional antennas. We then consider T-RIS embedding in the full 3D plane or just 2D plane, hence forcing $\theta_{AoD,l}$=90°. Figure 3-26 shows the 2D pattern embedding at the position RX5 for $\phi_{s,max} = 0°$. We can see that the embedding process results in some significant paths whose AoDs do not lie within the T-RIS range [-90°:1:90°] being eliminated. We can also see that the power of the MPCs whose AoDs are within the half power beamwidth (HPBW) are amplified while those outside HPBW are decreased when the embedding is performed using the radiation pattern for $\phi_{s,max} = 0°$. A similar behaviour is observed for the other receiver positions when embedded with the radiation patterns corresponding to ϕ_s. Figure 3-26 shows the 2D and 3D radiation pattern embedding ($\phi_{s,max} = 0°$), which takes into account both the azimuth and elevation planes for the position RX5. We can notice that some significant paths whose AoDs do not lie within the T-RIS range [-90°:1:90°] were eliminated. We can clearly see that 3D embedding impacts the MPCs in both the azimuth and elevation planes. Considering the T-RIS patterns for ϕ_s= 50° at position RX5, we can see the 2D and 3D embedding results in Figure 3-27. Indeed, the MPCs within the main beam direction are significantly impacted, showing the spatial filtering nature of the T-RIS.
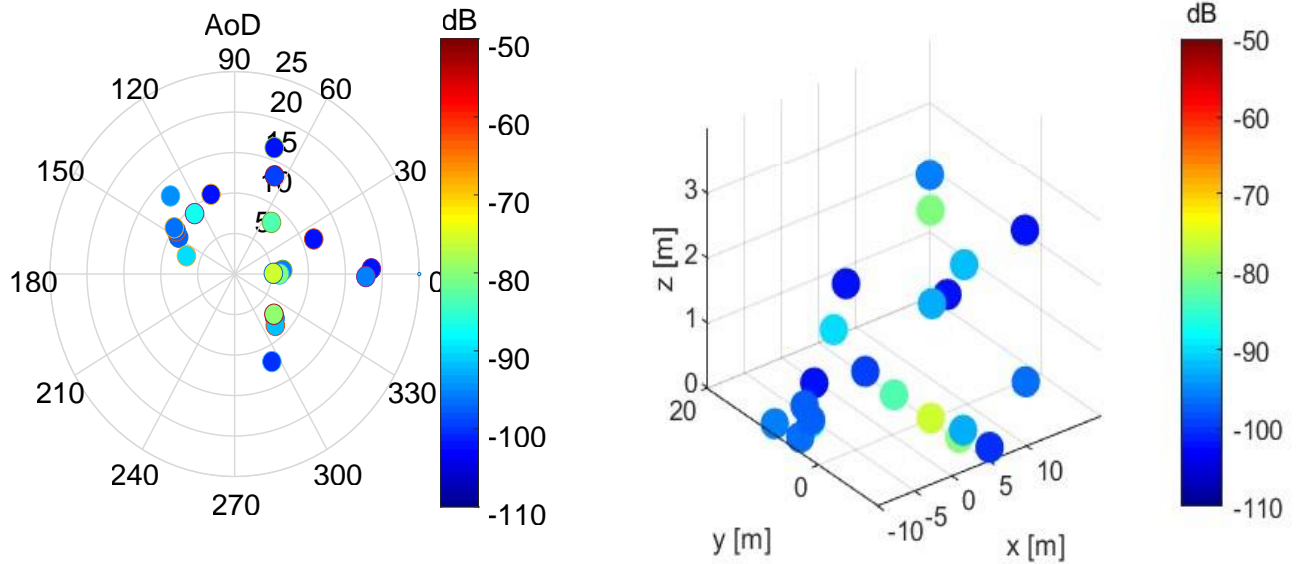
Figure 3-25 Omnidirectional PADP extracted from VCA measurements: 2D (left) and 3D (right).
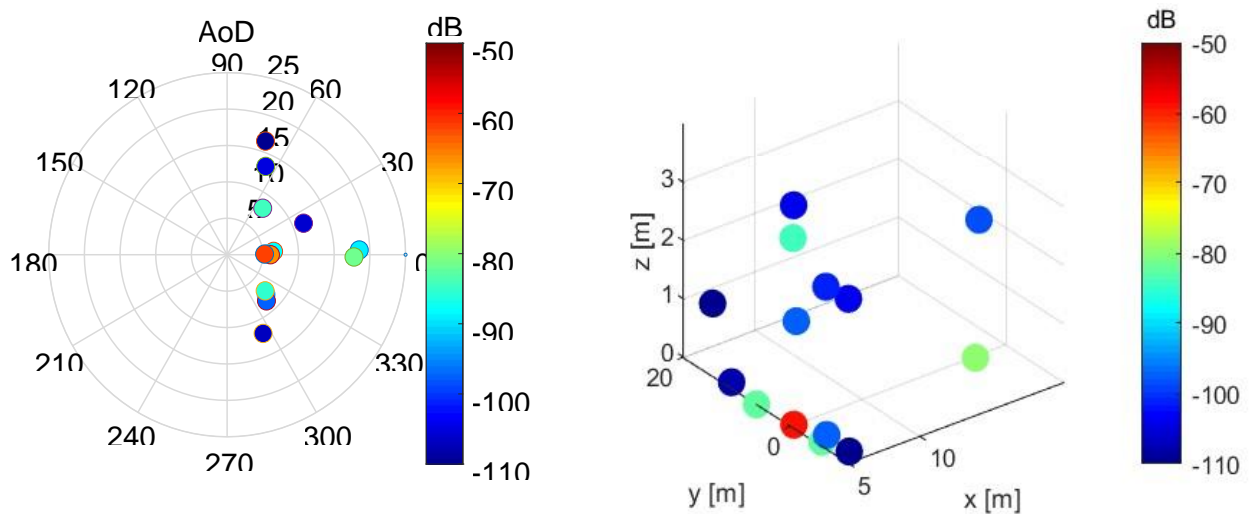
Figure 3-26 PADP with T-RIS embedding for ϕ_s= 0°. 2D pattern embedding (left), 3D pattern embedding (right)
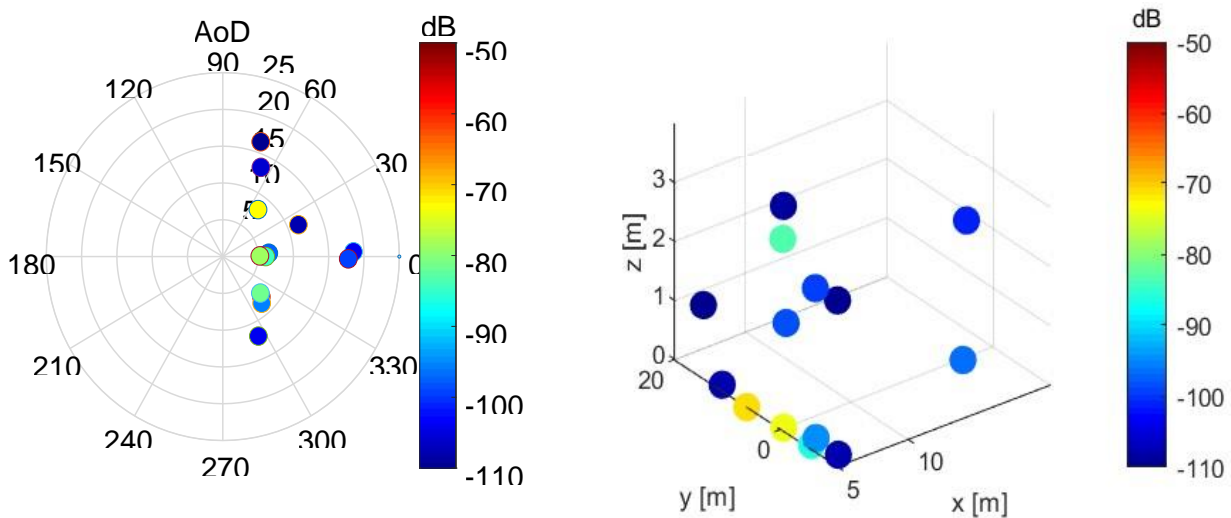
Figure 3-27 PADP with T-RIS embedding for ϕ_s= 50°. 2D pattern embedding (left), 3D pattern embedding (right)

With respect to the PDPs, Figure 3-28 shows a comparison of the actual T-RIS measured channel PDP (in blue color) with the PDPs of synthesized channels (in red, green and black colors). The synthesized channels involve the plugging in or embedding of the measured 2D and simulated 3D T-RIS radiation patterns to the UWB SAGE extracted MPCs from the VCA measurement setup. From the aforementioned figures, we can observe that the 3D synthesized channel closely resembles the actual measured channel as it corrects the overestimation of secondary MPCs powers encountered in the 2D synthesized channels. It is worth mentioning that there is a 3 dBi peak gain difference between the 2D T-RIS measured gain pattern and the 3D T-RIS simulated gain patterns, with the latter being higher. As expected embedding in the 3D dimension improves the quality of the model especially for secondary MPCs that could come at elevation angles far from the azimuth plane.

However, the process here involves only the MPCS that are extracted from UWB-SAGE, while it is well known that dense multipath components (DMCs) yield an important energy contribution . Hence, here we artificially add the DMCs extracted from VCA measurements to add them to the 3D synthesized channel. The PDP in black corresponds to the result of adding DMCs from the high resolution algorithm estimation to the 3D synthesized channel.
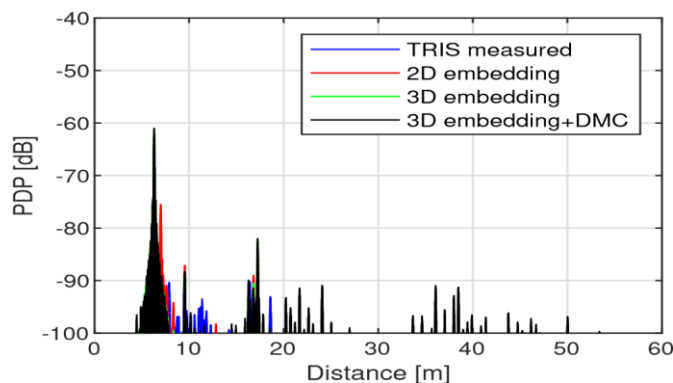
Figure 3-28 Example of PDP comparison: actual measured PDP vs synthesized PDPs.

Impact on channel characteristics

We employed the conventional power law model (4) to model the distance dependent channel gain:

$$G_{dB}(d) = G_0 - n \cdot 10 \cdot \log_{10}\left(\frac{d}{d_0}\right) + X_\sigma$$

(3.19)

where G_0 is the intercept in dB at the reference distance d_0 set to 1 m. The path loss exponent n indicates the decrease in channel gain as a function of the distance d between the transmitter and receiver. Both G_0 and n are obtained from the intercept and slope of the best-fit to (4) according to the minimum mean square error. X_σ is the variation due to long-term fading effects and is characterized through a normal distribution with zero mean and a standard deviation σ in dB. Figure 3-29 shows the channel gain comparison of the VCA measured channel, T-RIS measured channel and the synthesized channels in the maximum direction.

We can see that the VCA measured channel comprises the least channel gain and this is due to the presence of high gain T-RIS in the other cases. We can also see that the synthesized channel (considering the measured 2D T-RIS gain patterns), in red color, is lower compared to the actual measured T-RIS channel, in blue color, because the channel gain in the actual measured T-RIS channel includes the diffuse components which are not present in the synthesized channel. The synthesized channel considering measured 2D T-RIS gain pattern is also lower than the simulated 3D channel because of the 3dBi gain difference between the measured and the simulated T-RIS gains. The channel gain model parameters are given below. We observe that adding back the DMCs to the 3D embedding channel results in an improvement of the 3D model.

Table 3-1 Channel Gain model parameters

Scenario	G_0[dB]	n	σ[dB]
VCA meas	-61.2	1.63	0.54
TRIS meas	-47.1	1.44	0.56
2D embedding	-49.9	1.54	1.1
3D embedding	-45.1	1.9	0.5
3D embedding +DMC	-46.7	1.4	0.8

.

Table 3-2 Delay Spread Model Parameter

Scenario	a[ns/m]	b[ns]	σ_T[ns]
VCA meas	0.33	9.6	1.54
TRIS meas	0.64	5.03	0.5
2D embedding	0.06	5.5	0.6
3D embedding	0.19	4	0.47

3D embedding + DMC	0.32	14.8	1.26

The root mean square delay spread (DS), is the square root of the second central moment of the power delay profile (PDP). For a multipath channel, the DS is a measure of duration of time over which most of the symbol energy from the transmitter arrives to the receiver. The root mean square delay spread is calculated using the mean delay (the first moment of the PDP). To model the delay spread, we followed $\tau_{rms}[ns] = a \cdot d + b + X_\tau$ where a represents the delay spread, b is the intercept and X_τ denote a zero mean Gaussian random variable with standard deviation σ_τ. The delay spreads appear to increase with increasing transmitter-receiver separation distance. The delay spreads after adding back the DMCs are indeed higher as shown in the figure. In overall, the T-RIS cases (excluding the 3D embedding + DMC case) are characterized by lesser delay spreads than the VCA case and this is due to the high T-RIS gain and directivity. With regards to the angular spreads, not reported here for sake of briefness, we observed that the VCA channel is more spread in the azimuth plane (reaching values of over 50°) and less spread in the elevation plane (values around 5°) whereas the T-RIS synthesized cases are characterized by small angular spreads in both planes (less than 10°).
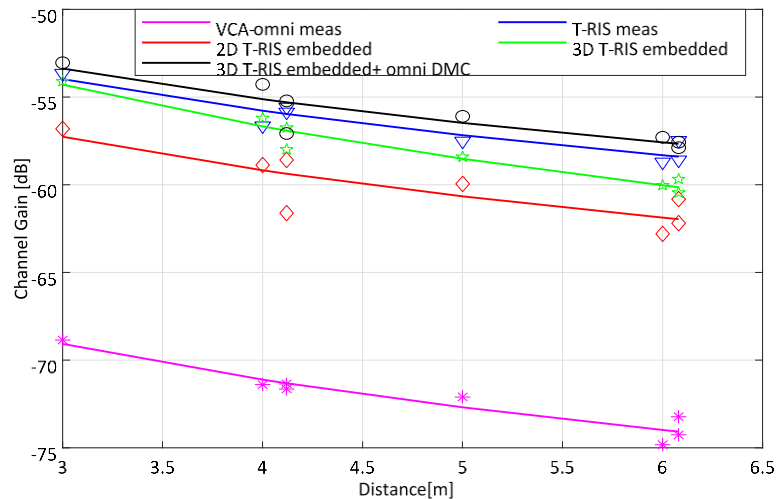
Figure 3-29 Channel gain comparison: measurements vs models.

In this paper, we evaluated how the structure of the channel is geometrically modified when a transmitting reconfigurable surface is employed instead of omnidirectional monopole scanning spatial grids. Starting from the MPCs extracted from the Virtual Cubic Array measurement setup, we embedded surface effect by knowing its radiation pattern for a given phase distribution and aimed steering angle. In our scenarios, the synthesized channel considering only the azimuth plane embedding (2D embedding) results in an overestimation of the powers of the secondary MPCs whose AoDs are within the half power beamwidth of the T-RIS. Performing 3D embedding, the synthesized channel highly resembles the actual T-RIS measured channel, since elevation information can effect multipath components amplitude. The large scale parameters showed that the high gain and directivity of the TRIS results in reduced path losses, delay and angular spreads. However considering only specular components do not seem enough to fully reproduce the measured results. As a first attempt we include dense multipath components (DMCs) to the 3D embedding channel improving channel gain model, but delay spread is slightly overestimated.

3.6.2 R-RIS enabled channel sounding and modelling

In order to integrate the impact of RIS into channel modelling, measurements of propagation channels in environments where RIS is present are needed. Before carrying out any measurement, a preparation step is necessary. In this step, the user must define the scenarios, schedule the campaign, decide which antennas to use, what are the parameter setups (frequency band, number of samples), channel sounding technique, estimate the link budget, etc. and the most important question, why measure. For RIS-enabled channel measurements, one must consider how to configure the direction of RIS beam in order to have an optimal gain in the desired direction, i.e. the receiver direction.

Therefore, in order to test the mastery of configuration of RIS, measurements were carried out in controllable environment, i.e. anechoic chamber, where only the direct path and the RIS scattering component were allowed to occur. The central frequency of 28 GHz with a bandwidth of 4 GHz were considered. The frequency step was set to 5 MHz, resulting in 801 as number of samples. The channel transfer function was recorded using a VNA where the transmit power was set to 10 dBm and an IFBW of 100 Hz was considered.

Horn antennas that have a gain of 20 dB at 28 GHz were considered. The RIS developed by Greenerwave is based on an electronically tunable metasurface with binary phase modulation and it forms 10 cm x 10 cm made up of 400 unit cells periodically placed every 0.5 cm (λ/2) on a rectangular lattice of 20x20 pixel. The RIS was developed for two linear polarizations over a wide frequency range around 28.5 GHz. Thus, an overall of 400 diodes to control vertical polarization and 400 diodes to control horizontal polarization. In order to control each pixel of the RIS, an FPGA control board was designed and programmed. The FPGA board can be connected to the desktop through LAN or USB interface and is controlled with a Python or MATLAB code. Therefore, the developed software allows to independently change the state of each diode on the RIS providing the required reflection properties across the whole RIS.

Preliminary measurements have been performed in CEA anechoic chamber and results will be exploited in the next period.
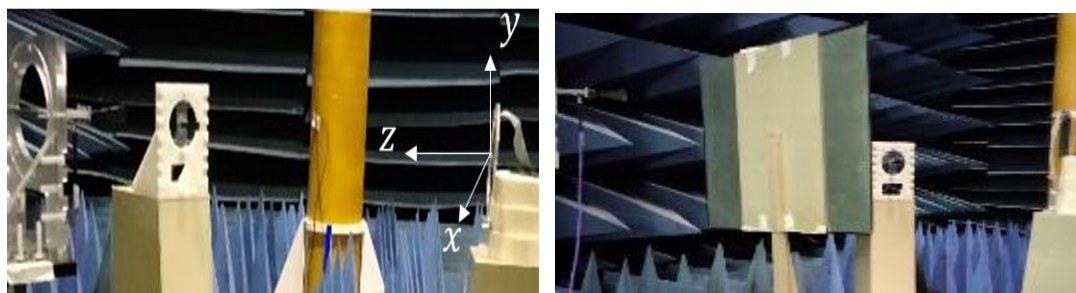
Figure 3-30 - Measurement scenario in the presence of RIS

3.7 Reverberation chamber channel emulation for RIS evaluation

Usually, the RC is adopted in EMC tests. Besides its conventional use, it can be also adopted in order to replicate real life environments such as indoor and outdoor scenarios, i.e. building

room, urban region, etc [LSR14]. The capability of the RC to replicate those environments allows us to save both time and money as opposed to in situ tests.

Two key parameters useful to characterize a propagation channel are the time delay spread, which indicates the spread between signal components as they are coming to the receiver, considering the time of arrival of the earliest and latest multipath components [HSP12, BGM15] and the power delay profile (PDP) which indicates the intensity of the received signal through the multipath channel as function of the time delay spread [SGF15].

$$\tau_{RMS} = \frac{\sqrt{\int_0^\infty (t - \tau_{ave})^2 \cdot \text{PDP}(t)dt}}{\int_0^\infty \text{PDP}(t)dt} \tag{3.20}$$

$$\text{PDP}(t) = \langle |h(t)|^2 \rangle_N \tag{3.21}$$

where $<.>_N$ means the ensemble average over N stirrer positions.

The replication of the propagation condition is made by controlling the power delay profile (PDP) and time delay spread, especially its root mean square value. These values have to match the value reported in the standard related to the desired scenario to be replicated [GFE09, PDP12]. These values can be tuned by adding a certain number, and position, of absorbing materials within the RC.

Here below we report different trends of the PDP as function of the chamber's load [MBB21]. In those cases, also the value of the τ_{RMS} are reported and we can note that the larger reduction of the PDP occurs in the "UHL" configuration [BGM15, MBB21]. UHL stands for ultra high load configuration, and denotes the case where the larger amount of absorbing material is added within the RC.
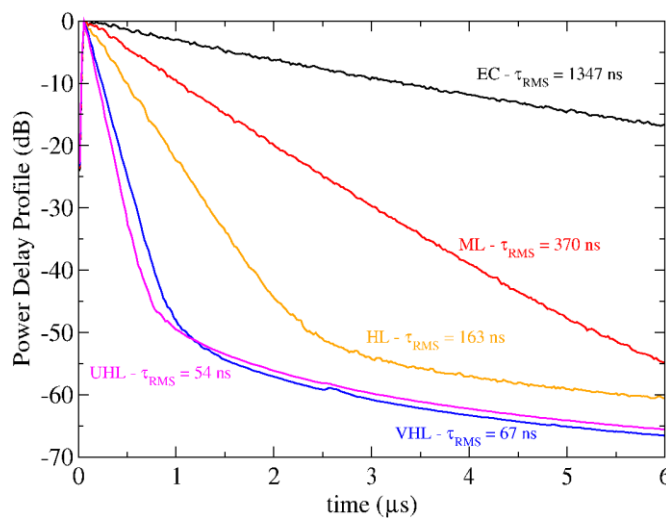
Figure 3-31 Evaluated τ_{RMS} and PDP for different chamber loading condition of the CNIT facility.
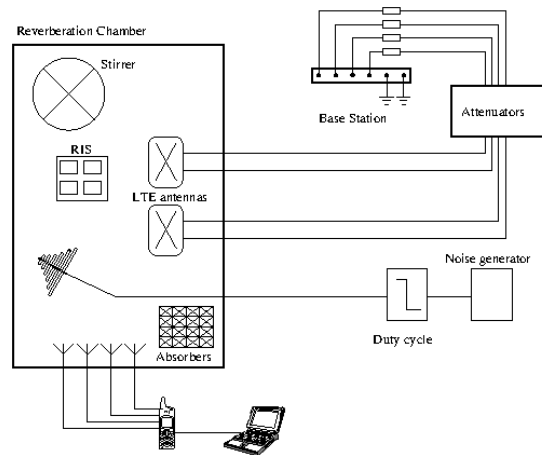
Figure 3-32 Sketch of the test environment setup where all the instruments are connected and RIS(s).

Figure above shows a possible setup where the RC is equipped by stirrer, MIMO antennas, absorbing materials and dedicated devices used in order to get channel parameters. The RC is fed by commercial base station connected to the live network of the mobile operator.

This setup allows us to measure KPIs of the emulated channel in a real scenario by means of the RC [MBM15, BMB17, MBC17].

The RIS(s) are included into the RC, by using mobile monopoles to collect transferring data it is possible to evaluate the benefit given to the insertion of RIS(s) on the overall wireless system.

4 RIS design and prototyping

4.1 Introduction

As presented before in the SoTA, RISs are fabricated similarly to known antenna concepts, which need to be opportunely redesigned to take into account the multi-function, EE, scalability, and flexibility paradigms required in B5G and envisioned for future 6G networks. In SoTA, several fixed-beam architectures based on reflectarrays, transmitarrays, or metasurfaces have been demonstrated up to sub-THz [GTB16], but in the case of electronically-tunable RISs, excluding the pioneer demonstrations of the RISE-6G's partners CEA, GNW, and CHAL d the complex phased arrays based on monolithic microwave integrated circuits [SGV19], only few prototypes have been demonstrated up to the Ka-band (26-40 GHz).

Recently it has been suggested to equip RISs with receiving antennas in order to extract information about the wireless channel from the impinging signal at the RIS [AV21], [TAA21]. This way, the overhead costly procedure of estimating the cascaded channel is avoided. In [LPP19], it is proposed to use the concept of Hypersurfaces with a control network that iterates over the active element states until the power sensed is maximized. The channel estimation is obtained by comparing the element states with a lookup table that contains the states to achieve full absorption for specific impinging waves. In [MBJ19] the smart meta-surface integrates additional sensors and controls the meta-surface with a sensing feedback system. The authors of [ASA21] introduce the concept of a Hybrid Reconfigurable Intelligent Surface (HRIS) that reflects and simultaneously senses a portion of the impinging waves. In [AAS21], a full-wave proof-of-concept and hardware design for an HRIS (a small portion of the incident wave is coupled to an array of sensing waveguides and the rest is reflected) is presented and the sensing capability is demonstrated with an AoA estimation example. Finally, in [ZSA21], for a multi-user uplink system empowered with HRIS, the individual channels identification problem is solved, and the results show notably reduced overhead.

In Deliverable 3.2, we will present in detail the main concepts, designs and characterizations of the RIS that will be developed in the framework of RISE-6G. In this document, we will simply give a brief overview of the main RIS concepts that we have started to develop since the beginning of RISE-6G. Of course, the final prototyping will be fixed based on the demonstrator needs in WP7.

Regardless of the physical concept behind them (usually the hybridisation of at least two resonances) and the central electrical component used to make them reconfigurable, the development of RIS always follows the same general procedure. The first step consists in designing the RIS unit cells. This numerical step allows to study and tuned the future properties of the RIS. Indeed, the main properties of a RIS are fixed by the key parameters of their unit cells. Among those parameters, the most noteworthy are :

- The unit cells central frequency and frequency bandwidth

- The physical mechanism for controlling locally the EM waves, i.e. whether the RIS will control the EM waves by applying a phase shift and/or amplitude modulation to the reflected or transmitted field.

- The core electrical component used to control the different states of the RIS (Pin diodes, varactors, MEMS,…)

- The number of state of the unit cells. For instance, a binary or 1-Bit unit cell based on Pin diodes is able to switch between two states that are characterized by their phase shift and mean dissipation.

- The number of components of the reflected electric field tangential to the unit cells plane that are independently control. A single pol unit cell control only one component whereas a dual pol is able to control independently both components of the EM field.

- The spacing between the unit cells.

After the numerical design, the second step consists in an experimental characterization of the unit cell. In order to experimentally verify the properties of the designed unit cell, a set of unit cell with slightly variable set of parameters are fabricated. There are several characterization methods depending on physical mechanism upon which the unit cells are based but also their dimensions. After the validation of the properties the different unite cells samples, the parameters which provides lower dissipation and better phase shift are selected.

The final step is to use the selected unit cell to manufacture the RIS. An important part of this step is the layout of the unit cells on the PCB, the routing of the various electrical components, the interface connectors and the PCB layouts which, in the end, will give us an operational RIS that can be remotely controlled. The RIS is finally tested experimentally to validate its properties.

An other important part in the development of RIS is the design and fabrication of the control board that define the hardware (USB, Ethernet,..) and software (C, Matlab, Python,…) interfaces between the RIS and the user.

4.1   Status of the main RIS design

In the table here below we list the status of main RIS design, concept and prototypes and we give few illustrations of unit cells and RIS already designed or under development. Part of them (named in Green) could fulfil the requirements for a demo but precise alignment with the PoC requirements, especially with respect to the bands, are expected for final RISE-6G design.

Table 4-1 RISE-6G prototypes and concepts

	Unit cells key parameters						Unit cells design & characteriztion status : Green=done ; Orange=Ongoing		RIS dimensions	control board	Unique prototype or product
	RIS nature	Central frequency	Bandwidth	Polarization controlled	spacing	Core techno					
GW-1	Reflective binary	5.2 GHz	500 MHz	double pol	λ/2	Pin diode	Num	Exp	28cmx23cm - 76x2 elements	Usb interface- Pyhton+Matlab	product
GW-2	Reflective binary	28 GHz	>3GHz	double pol	λ/2	Pin diode	Num	Exp	10 cmx10cm 15 cm x 15 cm	FPGA based, Usb + Ethernet interface- Pyhton+Matlab	product
GW-3	Reflective binary	28 GHz	>3GHz	double pol	λ/2 or 3 λ/2	Pin diode	Num	Exp	10 cmx10cm 15 cm x 15 cm 20cm x20 cm	FPGA based, Usb + Ethernet interface- Pyhton+Matlab	product
GW-4	Reflective binary	26.5 GHz	>3GHz	double pol	λ/2	Pin diode	Num	Exp	10 cmx10cm 15 cm x 15 cm	FPGA based, Usb + Ethernet interface- Pyhton+Matlab	product

ID	Type	Band	Frequency	Polarization	Spacing	Element	Num	Exp	Size	Control	Proto
									20cm x20 cm		
GW-5	Reflective/or Transmitive binary	3.5 Ghz	-	single pol	λ/2	Pin diode	Num	Exp	-	Wireless control via energy harvesting from a RFID reader	proto
CEA-1	T-RIS 1-bit	X	1.8 GHz	Single LP	λ/2	Pin diode	Num	Exp	30cmx30cm 400 elements	Usb interface µcontroller Matlab	Proto
CEA-2	T-RIS 1-bit	Ka	> 3 GHz	Dual CP + Dual LP	λ/2	Pin diode	Num	Exp	10cmx10cm 400 elemnts	Usb interface µcontroller Matlab	Proto
CEA-3	T-RIS 1-bit	Ka	8 GHz	Single LP	λ/2	Pin diode	Num	Exp	10cmx10cm 400 elemnts	Usb interface µcontroller Matlab	Proto
CEA-4	T-RIS 2-bit	Ka	> 3 GHz	Single LP	λ/2	Pin diode	Num	Exp	7cmx7cm 196 elemnts	Usb interface µcontroller Matlab	Proto
CEA-5	T-RIS 2-bit	Ka	> 2 GHz	Dual CP + Dual LP	λ/2	Pin diode	Num	Exp	120cmx120cm 576 elemnts	Usb interface µcontroller Matlab	Proto
CEA-6	T-RIS 2-bit R-RIS 1_bit	Ka	> 3 GHz	Single LP	λ/2	Pin diode	Num	-	120cmx120cm 576 elemnts	Usb interface µcontroller Matlab	Proto Change of control board
AAu-1	Reflective	3.7 GHz	200 MHz	double pol	λ spacing	MEMS	Num	-	-	segments with 2x2 patches sharing a control board	proto
ORA-1	Reflective (continous phase)	25.8GHz	3.25 GHz	single pol	-	Varactor	Num	Exp		Under dev.	proto
ORA-2	Reflective (continous phase)	5,5 GHz	0,8 GHz	single pol	-	Varactor	Num	Exp		RA ready. Logic control under test	proto
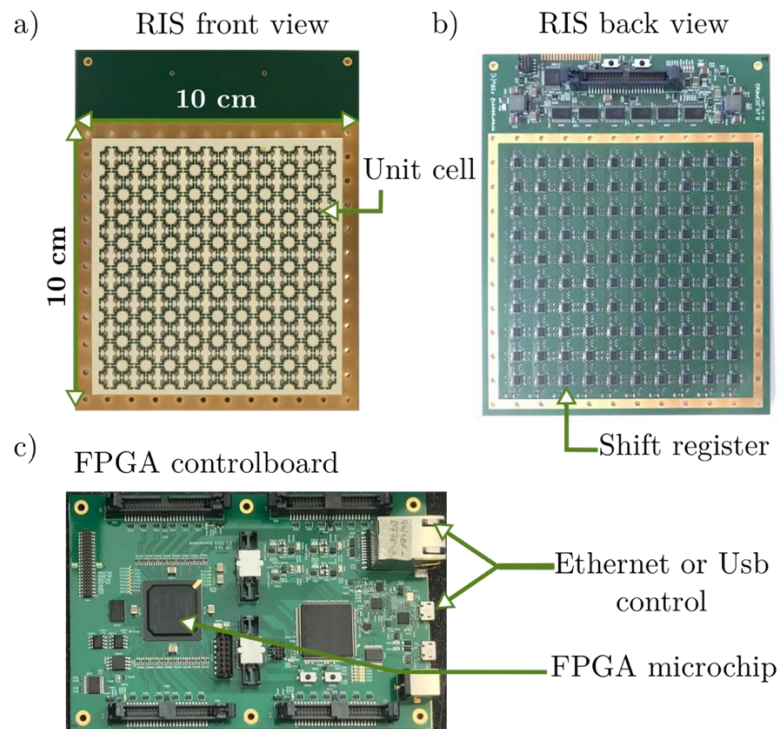
Figure 4-1 a) Front and b) back side of 10 × 10 cm2 GW2 mmWave RIS. c) RIS control board with different interfaces
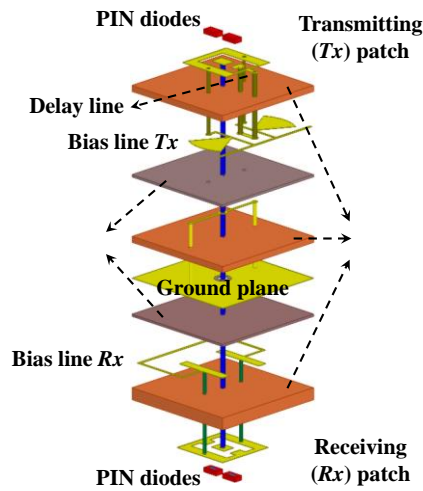
Figure 4-2: Proposed 2-bit linearly-polarized unit-cell: Schematic view of CEA6.
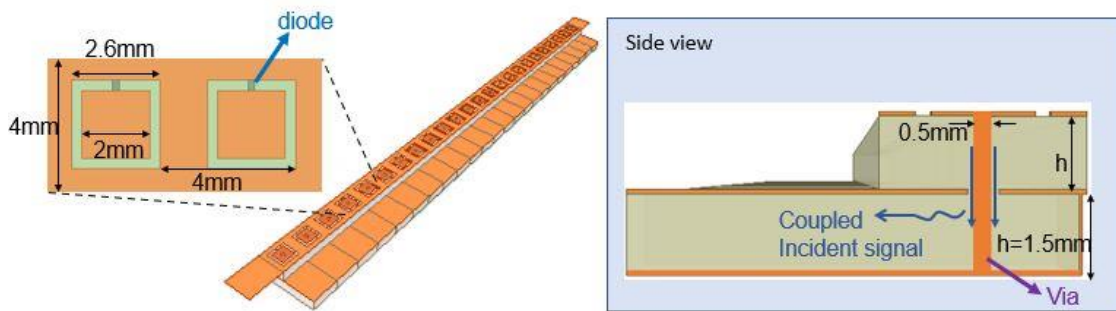
Figure 4-3 Hybrid RIS hardware design with integrated sensing capability.

5 Conclusions and perspective

In this document we presented different modelling approaches of RIS, based on full-electormagnetic models, equivalent impedance, and hybrid ones. Most of them have been validated on prototypes already available with the consortium or being developed during the project.

The inclusion of RIS in radio channel model has been proposed with different approaches including random coupling model for narrow bands and more general deterministic raytracing model, which could also benefit of RIS scatterrer models. Preliminary sounding activities including RIS have been also presented. Here below the perspectives for model validation and inclusion in system performance are discussed.

5.1 RIS/ channel modeling inclusion in system level simulation

The impedance model developed in Section 2.4.2 is being integrated in system-level simulators adopted to optimize the data load in Mobile Edge Computing (MEC) solutions. Current work is looking for the extension of advanced offloading strategies, which have been widely developed in WP4. In particular, the incorporation of the impedance-based channel model in MEC computing requires the consequent optimization of:

1. Time variability of the channel and data arrivals.

2. Unknown statistics of channel realization (i.e. scatterer/obstacles dynamics) and data arrivals.

3. Queueing delay, comprising communication and computation in edge computing scenarios.

The goal of this activity is to show the benefits of RIS-based communications by adopting an EM compliant RIS-assisted wireless propagation channel. Queueing theory and stochastic optimization are employed to jointly control radio (Tx power, bandwidth, etc.), computing (CPU scheduling for task processing) and wireless propagation (in the impedance-based model, Z_{RIS} is optimized to improve $|H_{E2E}|^2$) resources. Furthermore, the resources are optimized dynamically, based on instantaneous channel/arrivals realizations and queue states, with the objective of minimizing the average power consumption under delay constraints. In the channel model assumed for this study, obstacles are obtained by "packing" multiple dipole-like scatterers at nearest neighbour distance <0.5 λ. Preliminary results are shown in here below for a single user scenario: the performance gain obtained with a single RIS (with variable number of unit elements N), in terms of power-delay trade-off is clearly optimized by the presence of the RIS.
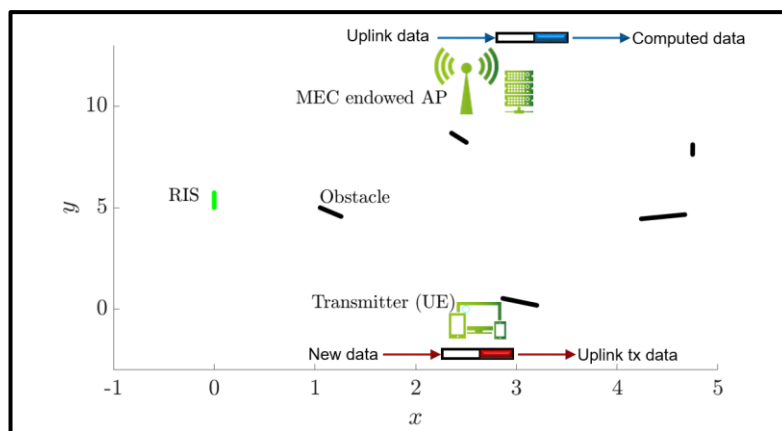

Figure 5.1. RIS-assisted SISO wireless link with linear clusters of dipoles representing obstacles.
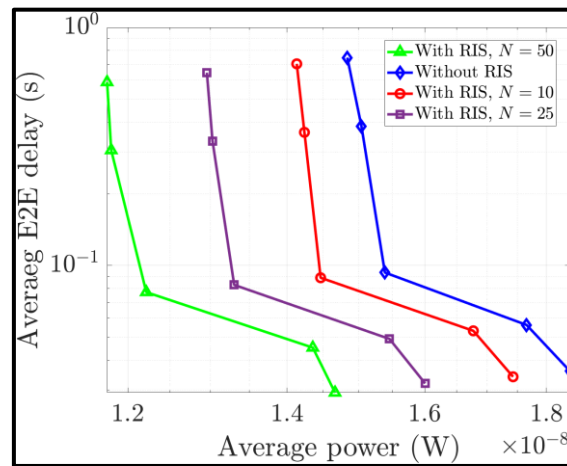
Figure 5.2. Average delay vs average power with and without RIS: the performance improve as the number of RIS unit elements increases.

The next step of the investigation will look at the overall system power consumption (possibly including RIS) in presence of multiple RIS and multiple users. Furthermore, a holistic end-to-end optimization of the RIS-assisted wireless link will be conceived, which includes specific unit cell design (Section 4), RIS power consumption models, average delay of MEC offloading strategy, energy and EMF efficiencies. MEC user cases have been selected as scenarios to pursue within RISE-6G, as reported in D2.3 and D2.4.

5.2 Next steps for modeling extension and validation

Modelling development and validation involve a wealth of activities where each and any Participant is contributing actively. RIS network design and coverage planning ultimately require a versatile framework incorporating multiple models that can be selected or combined in order to tackle the specific scenarios (and predict specific KPIs) defined in D2.1 and D2.2. This motivates the effort that Participants are devoting to extend and assess both the continuous and discrete RIS model families. The basic models created within the first year of RISE-6G will be applied to RIS prototypes available from GNW, CEA, ORA, NEC, and CHALMERS.

Further work will be conducted to:

1. Finalize the FDTD algorithms for T-RIS and R-RIS structures, which requires the implementation of GSTC boundary conditions and Huygens boxes.

2. Develop a theory for the integration of Rayleigh multi-path fading within FDTD algorithms and pursue applications in laboratory environments for fading emulation, e.g., reverberation chambers.

3. Reconcile the impedance-based model with abstract system-level models of the received signal, at least for RIS-assisted SISO wireless links (with T4.2 and WP5).

4. Extend impedance-based beyond the minimal scattering approximations of RIS unit cells with the aid of field-based models.

5. Integrate idealized multi-path fading into impedance-based and system-level RIS models, considering Ricean fading and hybrid LOS-NLOS scenarios.

6. Pursue the extension of RIS path loss models and their inclusion in power balance methods for better link budget calculations (with T6.2 and T6.3).

7. Develop CAD to mesh conversion strategies that are compliant with phase-space ray tracing algorithms in 2D.

8. Develop analytical models for the scattering matrices of the RIS in form of spatial-angular (phase-space) ray densities, by calculation of the Wigner function of field-based RIS models.

9. Include scattering models developed from T-RIS and R-RIS models into the DEA method integrating phase-space scattering matrices developed in 8.

10. Extend geometric channel models and their integration with channel sounding/measurements

6 References

[AAS14]   L. R. Arnaut, M. I. Andries, J. Sol and P. Besnier, "Evaluation Method for the Probability Distribution of the Quality Factor of Mode-Stirred Reverberation Chambers," in IEEE Transactions on Antennas and Propagation, vol. 62, no. 8, pp. 4199-4208, Aug. 2014, doi: 10.1109/TAP.2014.2327642.

[AAS21]   I. Alamzadeh, G. C. Alexandropoulos, N. Shlezinger, and M. F. Imani, "A reconfigura-ble intelligent surface with integrated sensing capabilities," Springer Nature Scientific Re-ports, to appear, 2021.

[AAT16]   V. S. Asadchy, M. Albooyeh, S. N. Tcvetkova, A. D¡az-Rubio, Y. Ra'di, and S. A. Tretyakov, "Perfect control of re-flection and refraction using spatially dispersive metasurfaces," Phys. Rev. B 94, 075142 - 19 August 2016.

[ADD21]   A. Abrardo, D. Dardari, M. Di Renzo and X. Qian, "MIMO Interference Channels Assisted by Reconfigurable Intelligent Surfaces: Mutual Coupling Aware Sum-Rate Optimization Based on a Mutual Impedance Channel Model," in IEEE Wireless Communications Letters, vol. 10, no. 12, pp. 2624-2628, Dec. 2021.

[AG12]   L. R. Arnaut and G. Gradoni, "Probability Distribution of the Quality Factor of a Mode-Stirred Reverberation Chamber," in IEEE Transactions on Electromagnetic Compatibility, vol. 55, no. 1, pp. 35-44, Feb. 2013.

[AG15]   L. R. Arnaut and G. Gradoni, "Probability Distribution of the Coherence Bandwidth of a Reverberation Chamber," in IEEE Transactions on Antennas and Propagation, vol. 63, no. 5, pp. 2286-2290, May 2015.

[AKG15]   K. Achouri, B. A. Khan, S. Gupta, G. Lavigne, M. A. Salem, and C. Caloz, "Synthesis of electromagnetic metasurfaces: principles and illustrations", EPJ Applied Metamaterials, vol. 2, p. 12, 2015.

[ARA19]   B. Addissie, J. Rodgers, T. Antonsen, "Extraction of the coupling impedance in overmoded cavities," Wave motion, Apr 1;87:123-31, 2019.

[ASA21]   G. C. Alexandropoulos, N. Shlezinger, I. Alamzadeh, M. F. Imani, H. Zhang, and Y. C. Eldar, "Hybrid reconfigurable intelligent metasurfaces: Enabling simultaneous tunable reflections and sensing for 6G wireless communications," [Online] https://arxiv.org/pdf/2104.04690.pdf, 2021.

[ASC151]   K. Achouri, M. A. Salem, and C. Caloz, "General metasurface synthesis based on susceptibility tensors", IEEE Trans. Antennas Propag., vol. 63, no. 7, pp. 2977-2991, Jul. 2015.

[ASC152]   K. Achouri, M. A. Salem, and C. Caloz, "Electromagnetic metasurface performing up to four independent wave transformations", in 2015 IEEE Conference on Antenna Measurements Applications (CAMA), Nov 2015, pp. 1-3.

[AV20]   G. C. Alexandropoulos and E. Vlachos, "A hardware architecture for reconfigurable intelligent surfaces with minimal active elements for explicit channel estimation," in Proc. IEEE International Conference on Acoustics, Speech, and Signal Processing, Barcelona, Spain, 4-8 May 2020, pp. 9175-9179.

[BG20]   J. Budhu and A. Grbic, "Perfectly Reflecting Metasurface Reflectarrays: Mutual Coupling Modeling Between Unique Elements Through Homogenization," in IEEE Transactions on Antennas and Propagation, vol. 69, no. 1, pp. 122-134, Jan. 2021, doi: 10.1109/TAP.2020.3001450.

[BGM15]   L. Bastianelli, L. Giacometti, V. Mariani Primiani, and F. Moglie, "Effect of absorber number and positioning on the power delay profile of a reverberation chamber," in 2015 IEEE International Symposium on Electromagnetic Compatibility (EMC), Dresden, Germany, Aug. 2015, pp. 422-427.

[BKS19J]   C. Bucheli et al., "Reconfigurable intelligent surfaces: Bridging the gap between scattering/reflection", arXiv:1912.05344, 2019.

[BLY92]   J. H. Beggs, R. J. Luebbers, K. S. Yee, and K. S. Kunz, "Finite-difference time-domain implementation of surface impedance boundary conditions", IEEE Trans. Antennas Propag., vol. 40, no. 1, pp. 49-56, Jan. 1992.

[BMB17]   M. Barazzetta, D. Micheli, L. Bastianelli, R. Diamanti, M. Totta, P. Obino, R. Lattanzi, F. Moglie, V. Mariani Primiani, A comparison between different reception diversity schemes of a 4G-LTE base station in reverberation chamber: a deployment in a live cellular network, IEEE Trans. Electromagn. Compat. 59 (6) (2017) 2029-2037. doi:10.1109/TEMC.2017.2657122.

[BMM20]   M. Bodehou, E. Martini, S. Maci, I. Huynen, and C. Craeye, "Multibeam and beam scanning with modulated metasur-faces," IEEE Trans. Antennas Propag., vol. 68, no. 3, pp. 1273-1281, Mar. 2020.

[CCR21]   D. Chappell, J.J. Crofts, M. Richter, and G. Tanner. "A direction preserving discretization for computing phase-space densities." SIAM Journal on Scientific Computing 43, no. 4, B884-B906, 2021.

[DCD20]   L. Di Palma, A. Clemente, L. Dussopt, R. Sauleau, P. Potier, and P. Pouliguen, "Circularly-polarized reconfigurable transmitarray in Ka-band with beam scanning and polarization switching capabilities," IEEE Trans. Antennas Propag., vol. 65, pp. 529-540, Feb. 2017.

[DCS20]   F. Diaby, A. Clemente, R. Sauleau, K. Pham, and L. Dussopt, "2-bit reconfigurable unit-cell and electronically steera-ble transmitarray at Ka-band," IEEE Trans. Antennas Propag., accepted for publication, 2020.

[DDT21]   M. Di Renzo, F. H. Danufane, S. Tretyakov, "Communication Models for Reconfigurable Intelligent Surfaces: From Surface Electromagnetics to Wireless Networks Optimization," arXiv: 2110.00833, 2021.

[DFV+07]   V. Degli-Esposti, F. Fuschini, E. M. Vitucci, G. Falciasecca, "Measure- ment and modelling of scattering from buildings," IEEE Trans. Antennas Propag., vol. 55 no 1, pp. 143–153, Jan. 2007

[DGL20]   C. Della Giovampaola, F. Camminita, G. Labate, E. Martini, and S. Maci, "Reconfigurable metasurface antenna for 5G base stations," in Proc. EuCAP, Copenhagen, Denmark, 2020, pp. 1-6.

[DT21]   A. Diaz-Rubio and S. A. Tretyakov, "Macroscopic modeling of anoma- lously reflecting metasurfaces: Angular response and far-field scattering," IEEE Trans. Antennas Propag., vol. 69, no. 10, pp. 6560–6571, Oct. 2021

[DZD20]   M. Di Renzo et al., "Smart Radio Environments Empowered by Reconfigurable Intelligent Surfaces: How It Works, State of Research, and The Road Ahead," in IEEE Journal on Selected Areas in Communications, vol. 38, no. 11, pp. 2450-2525, Nov. 2020, doi: 10.1109/JSAC.2020.3007211.

[FBP21]   A. Farasatul, V. Blakaj, S. Phang, T. M. Antonsen, S. C. Creagh, G. Gradoni, and G. Tanner. "Wireless power distributions in multi-cavity systems at high frequencies," Proceedings of the Royal Society A 477, no. 2245, 20200228, 2021.

[FLL04]   F. Falcone, T. Lopetegi, M.A.G. Laso, J.D. Baena, J. Bonache, M. Beruete, R. Marqu ?es, F. Mart?n, and M. Sorolla, "Babinet principle applied to the design of metasurfac-es and metamaterials", Phys. Rev. Lett., 93(19):197401, Nov 2004.

[GAA15]   G. Gradoni, T. M. Antonsen, S. M. Anlage and E. Ott, "A Statistical Model for the Excitation of Cavities Through Apertures," in IEEE Transactions on Electromagnetic Compatibility, vol. 57, no. 5, pp. 1049-1061, Oct. 2015, doi: 10.1109/TEMC.2015.2421346.

[GD21]   G. Gradoni and M. Di Renzo, "End-to-End Mutual Coupling Aware Communication Model for Reconfigurable Intelligent Surfaces: An Electromagnetic-Compliant Approach Based on Mutual Impedances," in IEEE Wireless Communications Letters, vol. 10, no. 5, pp. 938-942, May 2021, doi: 10.1109/LWC.2021.3050826.

[GDA16]   J. Gil Gil, Z. B. Drikas, T. D. Andreadis and S. M. Anlage, "Prediction of Induced Voltages on Ports in Complex, Three-Dimensional Enclosures With Apertures, Using the Random Coupling Model," in IEEE Transactions on Electromagnetic Compatibility, vol. 58, no. 5, pp. 1535-1540, Oct. 2016.

[GFE09]   Guidelines for evaluation of radio interface technologies for IMT Advanced, International Telecommunication Union - ITU Report M.2135-1, Dec. 2009.

[GTB16]   S. B. Glybovski, S. A. Tretyakov, P. A. Belov et al., "Metasurfaces: From microwaves to visible," Phys. Rep., vol. 634, pp. 1 - 72, 2016.

[GYX14]   G. Gradoni, J.H. Yeh, B. Xiao, T.M. Antonsen, S.M. Anlage, E. Ott, "Predicting the statistics of wave transport through chaotic cavities by the random coupling model: A review and recent progress.," Wave Motion, 51(4), 606-621, 2014.

[HC09]   T. H. Hand and S. A. Cummer, "A dynamic frequency selective surface using addressable metamaterials," 2009 IEEE Ant. and Prop. Soc. Inter. Symp., 2009.

[HC09]   T. H. Hand and S. A. Cummer, "A dynamic frequency selective surface using addressable metamaterials," 2009 IEEE Ant. and Prop. Soc. Inter. Symp., 2009.

[HGG16]   T. Hartmann, G. Tanner, G. Xie, D. Chappell, J. Bajars. "Modelling of high-frequency structure-borne sound transmission on FEM grids using the Discrete Flow Mapping technique," in Journal of Physics: Conference Series, vol. 744, no. 1, p. 012237. IOP Publishing, 2016.

[HGS08]   T.H. Hand, J. Gollub, S. Sajuyigbe, S.A. Cummer, and D.R. Smith, "Characterization of Complementary Electric Field Coupled (CELC) Resonator Surfaces", App. Phys. Lett. 93, 212504, 2008.

[HGS08]   T.H. Hand, J. Gollub, S. Sajuyigbe, S.A. Cummer, and D.R. Smith, "Characterization of Complementary Electric Field Coupled (CELC) Resonator Surfaces", App. Phys. Lett. 93, 212504, 2008.

[HSP12]   C. L. Holloway, H. A. Shah, R. J. Pirkl, K. A. Remley, D. A. Hill, and J. Ladbury, "Early time behavior in reverberation chambers and its effect on the relationships between coherence bandwidth, chamber decay time, RMS delay spread, and the chamber buildup time," IEEE Trans. Electromagn. Compat., vol. 54, no. 4, pp. 714-725, Aug. 2012.

[HVS17]   S. Hubert, A. Vallecchi, A. Schuchinsky and C. Craeye, "Modeling of impedance-loaded sub-wavelength metasurfaces," 2017 International Conference on Electromagnetics in Advanced Applications (ICEAA), 2017, pp. 1041-1044, doi: 10.1109/ICEAA.2017.8065438.

[JRZ21]   Z.-M. Jiang, M. Rihan, P. Zhang, L. Huang, Q. Deng, J. Zhang, and E. M. Mohamed, "Intelligent reflecting surface aided dual-function radar and communication system," IEEE Sensors Letters, 2021.

[LPP19]   C. Liaskos, G. Pirialakos, A. Pitilakis, S. Abadal, A. Tsioliaridou, A. Tasolamprou, O. Tsilipakos, N. Kantartzis, S. Ioannidis, E. Alarcon, A. Cabellos, M. Kafesaki, A. Pitsillides, K. Kossifos, J. Georgiou, and I. F. Akyildiz, "ABSense: Sensing Electromagnetic Waves on Metasurfaces via Ambient Compilation of Full Absorption," arXiv:1907.04811, July 2019.

[LSR14]   C. L"tb"ck Patan,, A. Sk†rbratt, R. Rehammar, C. Orlenius, Basic and advanced MIMO OTA testing of wireless devices using reverberation chamber, in: Proc. 8th Eur. Conf. Antennas Propag., The Hague, Netherlands, 2014, pp. 3488-3492. doi:10.1109/EuCAP.2014.6902581

[LU19]   J. S. Lu et al., "A discrete environment-driven GPU-based ray launching algorithm", IEEE Trans. Antennas Propag., vol. 67 no. 2, pp. 1558–2221,

[MBB20]   V. M. Primiani et al., "Reverberation chambers for testing wireless devices and systems," in IEEE Electromagnetic Compatibility Magazine, vol. 9, no. 2, pp. 45-55, 2nd Quarter 2020, doi: 10.1109/MEMC.2020.9133241.

[MBB21]   D. Micheli et al., "MIMO 4x4 vs. MIMO 2x2 Performance Assessment of a Real Life LTE Base Station in a Reverberation Chamber", in AEU - International Journal of Electronics and Communications, vol. 129, 2021, https://doi.org/10.1016/j.aeue.2020.153500

[MBC17]   D. Micheli, M. Barazzetta, C. Carlini, R. Diamanti, V. Mariani Primiani, F. Moglie, Testing of the carrier aggregation mode for a live LTE base station in reverberation chamber, IEEE Trans. Veh. Technol. 66 (4) (2017) 3024-3033. doi: 10.1109/TVT.2016.2587662.

[MBI17]   L. Pulido-Mancera, P. Bowen, M. Imani, N. Kundtz and D. Smith, "Polarizability extraction of complementary metamaterial elements in waveguides for aperture modeling", Phys. Rev. B, vol. 96, no. 23, Nov. 2017.

[MBI17]   L. Pulido-Mancera, P. Bowen, M. Imani, N. Kundtz and D. Smith, "Polarizability extraction of complementary metamaterial elements in waveguides for aperture modeling", Phys. Rev. B, vol. 96, no. 23, Nov. 2017.

[MBJ19]   Q. Ma, G. D. Bai, H. B. Jing, C. Yang, L. Li, and T. J. Cui, "Smart metasurface with self-adaptively reprogrammable functions," Light Sci Appl, vol. 8, p. 98, Oct. 2019.

[MBM15]   D. Micheli, M. Barazzetta, F. Moglie, V. Mariani Primiani, Power boosting and compensation during OTA testing of a real 4G LTE base station in reverberation

chamber, IEEE Trans. Electromagn. Compat. 57 (4) (2015) 623-634. doi: 10.1109/TEMC.2015.2434277.

[MBM16] F. Moglie, L. Bastianelli, V. Mariani Primiani, "Reliable Finite-Difference Time-Domain Simulations of Reverberation Chambers by Using Equivalent Volumetric Losses", IEEE Trans. on EMC, vol. 58, no.3, pp. 653-660 June 2016.

[MH73] J. Mautz and R. Harrington, "Modal analysis of loaded N-port scatterers," in IEEE Transactions on Antennas and Propagation, vol. 21, no. 2, pp. 188-199, March 1973, doi: 10.1109/TAP.1973.1140431.

[MPD20] S. Ma, S. Phang, Z. Drikas, B. Addissie, R. Hong, V. Blakaj, G. Gradoni, G. Tanner, T.M. Antonsen, E. Ott, S.M. Anlage, "Efficient statistical model for predicting electromagnetic wave distribution in coupled enclosures," Physical Review Applied, 8;14(1):014022, Jul 2020.

[NJS21] M. Najafi, V. Jamali, R. Schober and H. V. Poor, "Physics-Based Modeling and Scalable Optimization of Large Intelligent Reflecting Surfaces," in IEEE Transactions on Communications, vol. 69, no. 4, pp. 2673-2691, April 2021, doi: 10.1109/TCOMM.2020.3047098.

[PDP12] Propagation data and prediction methods for the planning of indoor radiocommunication systems and radio local area networks in the frequency range 900 MHz to 100 GHz, International Telecommunication Union - ITU Recommendation P.1238-7, Feb. 2012.

[PDS1] Multipath and Doppler Characterization of an Electromagnetic Environment by Massive MDT Measurements From 3G and 4G Mobile Terminals, https://ieeexplore.ieee.org/document/8620498

[PRL21] Z. Peng, C. Ross, Q. Jian Lim, G. Gradoni, Engineering Reflective Metasurfaces with Ising Hamiltonian and Quantum Annealing, under review, IEEE Transactions on Antennas and Propagation, (https://www.techrxiv.org/articles/preprint/Engineering_Reflective_Metasurfaces_with_Ising_Hamiltonian_and_Quantum_Annealing/14615031/1), 2021.

[PTG18] S. Phang, M. T. Ivrlac, G. Gradoni, S. C. Creagh, G. Tanner and J. A. Nossek, "Near-Field MIMO Communication Links," in IEEE Transactions on Circuits and Systems I: Regular Papers, vol. 65, no. 9, pp. 3027-3036, Sept. 2018, doi: 10.1109/TCSI.2018.2796305.

[PTH20] U. R. Patel, P. Triverio and S. V. Hum, "A Fast Macromodeling Approach to Efficiently Simulate Inhomogeneous Electromagnetic Surfaces," in IEEE Transactions on Antennas and Propagation, vol. 68, no. 11, pp. 7480-7493, Nov. 2020, doi: 10.1109/TAP.2020.3000857.

[QD21] X. Qian and M. D. Renzo, "Mutual Coupling and Unit Cell Aware Optimization for Reconfigurable Intelligent Surfaces," in IEEE Wireless Communications Letters, vol. 10, no. 6, pp. 1183-1187, June 2021, doi: 10.1109/LWC.2021.3061449.

[RVC19] J. R. Reis, M. Vala, R. F. S. Caldeirinha, "Review paper on transmitarray antennas," IEEE Access, vol. 7, pp. 94171-94188, Jun. 2019.

[SGF15] A. Sorrentino, A. Gifuni, G. Ferrara, and M. Migliaccio, "Mode-stirred reverberating chamber autocorrelation function: model, multifrequency measurements and applications," IET Science, Measurement Technology, vol. 9, no. 5, pp. 547-554, 2015.

[SMS06] D. Schurig, J. J. Mock, and D. R. Smith, "Electric-field-coupled resonators for nega-tive permittivity metamaterials", Appl. Phys. Lett. 88, 041109, 2006.

[SMS06] D. Schurig, J. J. Mock, and D. R. Smith, "Electric-field-coupled resonators for negative permittivity metamaterials", Appl. Phys. Lett. 88, 041109, 2006.

[SN17]	I. V. Shadrivov and D. N. Neshev, Tunable Metamaterials, World Scientific, 2017, chapter 9, pp. 387-418.
[SPV00]	D.R. Smith, W.J. Padilla, D. Vier, S. Nemat-Nasser, and S. Schultz, "Composite medium with simultaneously negative permeability and permittivity", Phys. Rev. Lett., 84(18):4184-4187, May 2000.
[SPV00]	D.R. Smith, W.J. Padilla, D. Vier, S. Nemat-Nasser, and S. Schultz, "Composite medium with simultaneously negative permeability and permittivity", Phys. Rev. Lett., 84(18):4184-4187, May 2000.
[SYM17]	D. R. Smith, O. Yurduseven, L. P. Mancera, P. Bowen, and N. B. Kundtz, "Analysis of a waveguide fed metasurface antenna," Phys. Rev. App., Nov. 2017.
[SYM17]	D. R. Smith, O. Yurduseven, L. P. Mancera, P. Bowen, and N. B. Kundtz, "Analysis of a waveguide fed metasurface antenna," Phys. Rev. App., Nov. 2017.
[TAA21]	A. Taha, M. Alrabeiah and A. Alkhateeb, "Enabling Large Intelligent Surfaces With Compressive Sensing and Deep Learning," in IEEE Access, vol. 9, pp. 44304-44321, March 2021.
[TAF95]	A. Taflove, "Computational Electrodynamics: The Finite-Difference Time-Domain Method", Norwood, MA: Artech House, 1995.
[TBM14]	J. P. Turpin, J. A. Bossard, K. L. Morgan et al., "Reconfigurable and tunable metamaterials: A review of the theory and applications," HINDAWI Int. J. Antennas. Propag., vol. 2014, 429837, 18 pages, 2014.
[V07]	O. Roy and M. Vetterli, "The effective rank: A measure of effective dimensionality," 2007 15th European Signal Processing Conference, 2007, pp. 606-610.
[VAC16]	Y. Vahabzadeh, K. Achouri and C. Caloz, "Simulation of Metasurfaces in Finite Difference Techniques", in IEEE Transactions on Antennas and Propagation, vol. 64, no. 11, pp. 4753-4759, Nov. 2016, doi: 10.1109/TAP.2016.2601347.
[VCA18]	Y. Vahabzadeh, N. Chamanara, K. Achouri and C. Caloz, "Computational Analysis of Metasurfaces", in IEEE Journal on Multiscale and Multiphysics Computational Techniques, vol. 3, pp. 37-49, 2018, doi: 10.1109/JMMCT.2018.2829871.
[VCC18]	Y. Vahabzadeh, N. Chamanara, and C. Caloz, "Generalized sheet transition condition FDTD simulation of metasurface", IEEE Trans. Antennas Propag., vol. 66, no. 1, pp. 271-280, Jan. 2018.
[VVD+22]	V. Degli-Esposti, E. M. Vitucci, M. Di Renzo and S. Tretyakov, "Reradiation and Scattering from a Reconfigurable Intelligent Surface: A General Macroscopic Model," in IEEE Transactions on Antennas and Propagation, doi: 10.1109/TAP.2022.3149660.
[XD21]	X. Qian and M. D. Renzo, "Mutual Coupling and Unit Cell Aware Optimization for Reconfigurable Intelligent Surfaces," in IEEE Wireless Communications Letters, vol. 10, no. 6, pp. 1183-1187, June 2021.
[YCY16]	H. Yang, X. Caon F. Yang, J. Gao, S. Xu, M. Li, X. Chen, Y. Zhao, Y. Zheng, and S. Li, "A programmable metasur-faces with dynamic polarization, scattering and focusing control," Scientific Reports, 6, 35692, Oct. 2016.
[YFY19]	Yang, Fan, and Yahya Rahmat-Samii. Surface Electromagnetics: With Applications in Antenna, Microwave, and Optical Engineering. 2019.
[ZSA21]	H. Zhang, N. Shlezinger, I. Alamzadeh, G. C. Alexandropoulos, M. F. Imani, and Y. C. Eldar, "Channel estimation with simultaneous reflecting and sensing reconfigurable intelligent metasurfaces," IEEE International Workshop on Signal Processing Advances in Wireless Communications, Lucca, Italy, 27-30 Sept. 2021.